UNIVERSITY OF GENOVA

PHD PROGRAM IN BIOENGINEERING AND ROBOTICS

Applicability of Advanced Diffusion Magnetic Resonance Imaging in clinical routine of Neonatal Data

by

Rosella Denise Trò

Thesis submitted for the degree of *Doctor of Philosophy* (34° cycle)

July 2022

<table>
<tr><td>Marco Massimo Fato</td><td>Supervisor</td></tr>
<tr><td>Giorgio Cannata</td><td>Head of the PhD program</td></tr>
</table>

Thesis Jury:

<table>
<tr><td>Filippo Molinari, <i>Politecnico di Torino</i></td><td>External examiner</td></tr>
<tr><td>Claudia Casellato, <i>University of Pavia</i></td><td>External examiner</td></tr>
<tr><td>Andrea Canessa, <i>University of Genoa</i></td><td>Internal examiner</td></tr>
</table>

Dibris

Department of Informatics, Bioengineering, Robotics and Systems Engineering

I would like to dedicate this thesis to my mother. Even if you are not here with us anymore, you are my everyday source of life. The strongest and most beautiful. . .

Declaration

I hereby declare that except where specific reference is made to the work of others, the contents of this dissertation are original and have not been submitted in whole or in part for consideration for any other degree or qualification in this, or any other university. This dissertation is my own work and contains nothing which is the outcome of work done in collaboration with others, except as specified in the text and Acknowledgements. This dissertation contains fewer than 65,000 words including appendices, bibliography, footnotes, tables and equations and has fewer than 150 figures.

<div align="right">

Rosella Trò
June 2022

</div>

Acknowledgements

First I would like to acknowledge my supervisor, professor Marco Massimo Fato, who supported and trusted me during this path, allowing me the right amount of freedom of action so as to develop my own research ideas and preferences across the vast field of neuroimaging.

I would also like to thank professor Gabriele Arnulfo for constantly lending me a hand in my work, always providing precious suggestions and insights. I could not have completed this dissertation without his support.

Then, I would like to acknowledge all my work collaborators: Antonio Napolitano, Julien Cohen-Adad and Shreyas Fadnavis. It was a great opportunity to discuss and share ideas with different backgrounds.

My gratitude also extends to all my lab mates for a cherished time spent together in the lab as well as in social settings.

I would like to thank all my family, my uncles, my grandmother and my sisters, who are my cornerstone and my pride. Finally, I am deeply grateful to my life partner Alberto for all the tremendous understanding and encouragement in the past few years and forsharing with me the worst and the best moments making them unique. The new adventure we started together has given me even more boost to accomplish this intense path as well as possible.

Abstract

Diffusion Magnetic Resonance Imaging (dMRI), a variant of conventional MRI based on the tissue water diffusion rate, has recently gathered an extraordinary interest among the scientific community due to the relationships found between several neurological and neurosurgical pathologies and alterations in diffusivity of both white and gray matter. It can thus be considered the imaging method of choice to study the brain, and several steps forward have been made from Diffusion Tensor Imaging (DTI) - the method which first showed the capabilities of dMRI - to advanced diffusion analysis methods.

Applying these cutting-edge imaging techniques to investigate pediatric subjects is gaining increasing popularity precisely for the unparalleled sensitivity to tissue microstructure compared to conventional MRI. Indeed, advanced dMRI models turn out to be ideal for investigating fast tissue growth and differentiation characterizing early infancy and not detectable with the same degree of sensitivity with structural MRI.

If, with regard to infant brain, most recent dMRI techniques have already been successfully applied in research studies and are entering clinical routine, their use in imaging of neonatal spinal cord is still unexplored. Nonetheless, we are dealing with an innovative, up-to-date domain which holds great promise for diagnosis and understanding of pathological conditions due to injury of both grey and white matter tracts. However, there are considerable challenges to this kind of imaging and research at present is focusing its effort on sorting them out. Further issues concern the application of this imaging in a pediatric clinical setting, which presents specific requirements in terms of acquisition sequences in contrastto current advanced diffusion methods.

The main goal of my PhD project, in collaboration with the LIFT (Laboratorio di Imaging Funzionale a 3Tesla) of Gaslini Children's Hospital in Genoa, has been to allow translation of advanced dMRI methods into clinical routine for the analysis of neonatal data, both in brain and spinal cord, considering the close interconnection between these two districts. Specifically, during my PhD work, I have paid particular attention to: (i) the design of ad-hoc acquisition sequences and preprocessing pipelines tailored for neonates - a crucial step at this delicate age-range; (ii) the application of Diffusion Kurtosis Imaging (DKI) model, a

promising extension of DTI quantifying non-gaussian diffusion in biological tissues; and (iii) the investigation of preterm birth in order to find new potential biomarkers, given its still high incidence and adverse impact worldwide.

Table of contents

List of figures

List of tables

Nomenclature

Acronyms / Abbreviations

5TT   Five-Tissue-Type

ACR   Anterior Corona Radiata

ACT   Anatomically-constrained tractography

AD   Axial Diffusivity

AK   Axial Kurtosis

ALIC   Anterior Limb of Internal Capsule

AMICO Accelerated Microstructure Imaging via Convex Optimization

BET   Brain Extraction Tool

CAU   Caudate

CCA   Canonical Correlation Analysis

CC   Corpus Callosum

CC   Cross Correlation

CNN   Convolutional Neuronal Network

CNS   Central Nervous System

cSC   cervical Spinal Cord

CSD   Constrained Spherical Deconvolution

CSF   Cerebro Spinal Fluid

CSTs Cortico Spinal Tracts

CVI   Cavum Veli Interpositi

d_par parallel diffusivity

d_perp perpendicular diffusivity

DKI   Diffusion Kurtosis Imaging

dMRI Diffusion Magnetic Resonance Imaging

DTI   Diffusion Tensor Imaging

DWI   Diffusion Weighted Imaging

EPI   Echo Planar Imaging

FA   Fractional Anisotropy

fa   fractional anisotropy

fODF fibre Orientation Distribution Function

FORECAST Fiber ORientation Estimated using Continuous Axially Symmetric Tensors

FOV   Field-of-View

GA   Gestational Age

GM   Gray Matter

GMH   Germinal Matrix Hemorrhage

HARDI High Angular Resolution Diffusion Imaging

HCP   Human Connectome Project

ICVF Intra Cellular Volume Fraction

ISOVF Isotropic Volume Fraction

IVH   Intra Ventricular Hemorrhage

KFA   Kurtosis Fractional Anisotropy

MASS Multi Atlas Skull Stripping

MB   Multi Band

MD   Mean Diffusivity

md   mean diffusivity

MK   Mean Kurtosis

MKT   Mean Kurtosis Tensor

ML   Machine Learning

MRI   Magnetic Resonance Imaging

MSK   Mean Signal Kurtosis

MSMT CSD Multi-Shell Multi-Tissue Constrained Spherical Deconvolution

NDI   Neurite Density Index

NLSAM Non Local Spatial and Angular Matching

NODDI Neurite Orientation Dispertion and Density Imaging

OLS   Ordinary Least Square

PAL   Pallidum

PLIC   Posterior Limb of Internal Capsule

PUT   Putamen

PVE   Partial Volume Effect

PVL   Periventricular Leukomalacia

PVE   Periventricular White Matter Injury

QC   Quality Control

RD   Radial Diffusivity

RF   Radio Frequency

RGB   Red-Green-Blue

RK   Radial Kurtosis

ROBEX Robust Brain Extraction

ROC   Receiver Operating Characteristic

ROI   Region of Interest

SAR   Specific Absorption Rate

SCI   Spinal Cord Imaging

SCP   Superior Cerebellar Peduncle

SC   Spinal Cord

SCT   Spinal Cord Toolbox

SD   Spherical Deconvolution

SNR   Signal-to-Noise Ratio

SVM   Support Vector Machine

TBSS Tract-Based Spatial Statistics

TEA   Term Equivalent Age

TFE   Turbo Field Echo

TH   Thalamus

TSE   Turbo Spin Echo

T   Tesla

VBM   Voxel Based Morphometry

WA   Weighted Average

WD   Wasserstein Distance

WMTI White Matter Tract Integrity

WM   White Matter

Part I

Introduction

Chapter 1

Motivation and rationale

*Children are the living messages we
send to a time we will not see*

John F. Kennedy
35th President of the United States

This sentence by President Kennedy, in my opinion, perfectly grasps the importance society should address to children's care. Indeed, newborns will be the adults of tomorrow: any effort dedicated ensuring them decent living standards is a mirror of society's self-respect and of the leagacy it leaves. This effort obviously translates in investments in infants' educational path but cannot disregard attention to their well-being.

Among various research fields in pediatrics, investigation of children's Central Nervous System (CNS) is by far the most fascinating and challenging. In effect, if science currently knows very little about healthy adult brain, study of infant CNS opens even more questions and issues. Understanding how the human brain develops from the very early stages is the only way to shed light on what allows children to acquire amazing and unique abilities, as well as on the impact of early disruptions (e.g., prematurity, neonatal insults) potentially leading to a wide range of neurodevelopmental disorders in adulthood.

Developing brain is subject to rapid, subtle structural, metabolic, and functional changes starting before birth and continuing into early childhood. This adaptive neuronal plasticity inherent to newborn's brain characterizes also Spinal Cord (SC), as underlined by the close interconnection existing between these two districts. Although neurodevelopment occurring at these early stages may have a substantial impact on later cognition, language, and social behavior, much remains to be discovered and understood about the processes that interact across early development to result in normative brain and spine. Added to this is the wide

variety of congenital or early acquired defects, malformations and abnormalities affecting CNS in the perinatal period.

A crucial though overlooked and neglected problem is represented by preterm births. Medical complications due to prematurity are the second leading cause of death and disability among children under five years of age, and preterm births occur 5–18% globally, leading to more than 1 million deaths per year (Liu et al., 2016). Its adverse impact on neurological development has been demonstrated in a number of cognitive, behavioral, and neuroimaging studies (Atkinson and Braddick, 2007; Spittle et al., 2011; Van Braeckel and Taylor, 2013; Volpe, 2009) .

In the last decade, incorporating imaging has contributed to invaluable insights about neurodevelopment at the start of life, with the disruptive emergence of neuroimaging studies in infant populations. As it can be performed well before knowing the child's behavioral and clinical outcome, MRI is an irreplaceable exploration method to evaluate the efficiency of early neuroprotective or neuroregenerative interventions aiming to avoid long-term disabilities in children. In this regard, a great contribution is being provided by diffusion MRI (dMRI) (Baliyan et al., 2016), a variant of conventional MRI based on water diffusion rate in body tissues offering undisputed advantages in terms of increased sensitivity to the underlying tissue architecture and thus providing unique information regarding the organization of brain fibres. dMRI has turned out to be particularly suitable for neonatal age range thanks to its ability to detect and characterize brain damage significantly earlier than structural MRI, and thus allowing successful early intervention.

From its first and standard model – Diffusion Tensor Imaging (DTI) (Soares et al., 2013) – to the most advanced techniques (Farquharson et al., 2013), dMRI has seeked increasing consensus within neuroimaging community asserting itself as the method of choice for in-vivo White Matter (WM) and Gray Matter (GM) assessment in adults. Despite its promising ability in unraveling underlying neurobiological mechanisms that drive both normal and atypical neurodevelopment, application of this imaging technique, in particular in its most recent developments, in newborns and children poses several technological and methodological challenges inherent to the delicate age range under analysis, especially as regards SC.

Indeed, if, limited to infant brain, a fast-increasing number of clinical applications and software packages are being developed, advanced dMRI is still largely underutilized in neonatal SC imaging because of its inherently demanding technological requirements. Nevertheless, results arising from recent application of dMRI to adult and child SC are

promising enough to suggest how informative this technique would be in investigating newborns, too.

In view of above considerations, I found the chance to closely collaborate with Giannina Gaslini Children's Hospital of Genova a precious and unmissable opportunity. Following the entire clinical procedure from MRI acquisition in this excellence reality, I persuaded more and more about the importance of addressing funds and resources in every attempt to improve life outcome of such defenseless human beings and about the necessity to translate state-of-the-art techniques into clinical use.

Consequently, I focused my PhD path on the application of advanced dMRI models in the neonatal age range (0-1 month) both for the brain and SC. I thus addressed my effort to translate these latest techniques to clinical routine, with all the issues that this entails. Adapting existing processing tools in use for adults to deal with age-specific requirements is essential to derive robust and reliable neuroimaging markers of multiple neurodevelopmental mechanisms, that can also be related to clinical, behavioral, and electrophysiological indexes from a diagnostic and prognostic perspective.

Chapter 2

Background

2.1 Diffusion Magnetic Resonance Imaging

Introduced in the mid-1980s, dMRI, also known as Diffusion-Weighted Imaging (DWI), is a particular type of MRI based upon measuring the random Brownian motion of water molecules within a voxel of tissue. Indeed, diffusion properties of water molecules largely differ depending on the underlying microarchitecture: homogeneous mediums, like a glass of water, exhibit a free, uniformly distributed diffusion of water molecules, whereas in highly ordered organs such as the brain, diffusion is driven by the tissue topological arrangement itself.

Specifically, while in the Cerebro-Spinal Fluid (CSF) and GM, water motion does not significantly prevail in any direction (*isotropic diffusion*); in WM, water molecules move preferentially along the direction of axons and fibre tracts (*anisotropic diffusion*). This difference in diffusivity is the cornerstone of the tissue contrast mechanisms obtained with dMRI, alternative to well-known contrasts T_1 and T_2.

As a result, dMRI is able to extract information about the water molecules exchange between intra- and extra-cellular space, managing to detect changes in the cerebral tissue due to neurological diseases or other pathologies.
Since its introduction, this modality has become one of the pillars of neuroimaging, precisely thanks to its ability in probing tissue structure in living organs non-invasively and at a microscopic scale. Investigation of neurological disorders such as acute brain ischemia, management of cancer patients, tracing and reconstruction of WM fibre tracts are just few examples among the multiple and rapidly-evolving applications of dMRI.

The sensitization of the image to diffusion is obtained by linearly varying the homogeneity of the magnetic field with gradient pulses applied across several directions.

A first pulsed field gradient is applied along a direction (*dephasing gradient*), causing the protons to precess at different rates along the selected direction, depending on their position along the gradient. This in turn implies dephasing of proton spins, to the extent that a signal loss is registered. After a given amount of time, an inverse gradient pulse is applied to the field along same direction (*rephasing gradient*).

Two possible cases can occur at rephasing gradient: the protons that have not moved between gradients applications (*no diffusion*) acquire a perfect rephasing and there is not a signal loss; coversely, those protons which have moved during this interval (*diffusion of water molecules*) experience an imperfect rephasing and a signal loss is measured by the receiver coil of the MRI scanner.

This represents the basic sequence for dMRI acquisitions designed by pioneers of the study (Stejskal and Tanner, 1965), who also modelled the signal reduction as an exponential decay:

$$S = S_0 \cdot e^{-\gamma^2 G^2 \delta^2 (\Delta - \frac{\delta}{3})D} \tag{2.1}$$

where S is the signal after application of the diffusion-sensitizing gradients, S_0 is the signal in absence of diffusion weighting, γ is the gyromagnetic ratio, G and δ the strength and duration of the gradient pulse, Δ the interval between the dephasing and rephasing pulses, and D the diffusion coefficient. (Le Bihan and Breton, 1985) simplified this expression by parametrizing the decay by the so called b value, a factor characteristic of the duration, strength and time between the two gradients. The signal attenuation thus becomes:

$$S = S_0 \cdot e^{-bD} \tag{2.2}$$

In an anisotropic medium, the diffusion coefficient is not constant but forms a diffusion tensor $\underline{\boldsymbol{D}}$, required to fully describe molecular movement along all directions in space. The first dMRI method to be developed for characterization of this tensor was DTI.

2.2   Diffusion Tensor Imaging

DTI was first introduced by (Basser et al., 1994) to fully characterize the diffusion of water molecules in body tissues. In anisotropic tissues, as in the case of the brain or, more importantly, SC, a tensor takes over for a single scalar coefficient to comprehensively describe

the different amounts of movement along all directions.

Such 2nd order diffusion tensor assumes the following form:

$$\underline{D} = \begin{bmatrix} D_{xx} & D_{xy} & D_{xz} \\ D_{yx} & D_{yy} & D_{yz} \\ D_{zx} & D_{zy} & D_{zz} \end{bmatrix} \qquad (2.3)$$

and is symmetric and positive definite ($D_{ij} = D_{ji}$, with $i, j = x, y, z$ reference frame of the MRI scanner)

Equation 2.2 thus becomes:

$$S = S_0 \cdot e^{- \sum\limits_{i=x,y,z} \sum\limits_{j=x,y,z} \underline{b}_{ij} \underline{D}_{ij}} \qquad (2.4)$$

where $\underline{b}$ is a matrix containing diffusion weights (b values) along each diffusion encoding direction, index i and j corresponds to a unique encoding direction.
For standard DTI protocol, a single b value for all directions is sufficient (Le Bihan et al., 2001). It is usual to report this expression in the logarithmic domain and to describe it through a set of linear equations, then solved through fitting procedures.
In theory, thanks to diffusion tensor's symmetry, the minimal set of images needed for its estimation is composed of six volumes acquired along six different gradient directions, plus at least an image with no diffusion weighting ($b = 0$) used as a reference for preprocessing. In practice, data should be collected along as many directions in space as possible, usually distributed uniformly on a sphere. Indeed, this uniform space sampling strategy allows to avoid sampling direction biases, is particularly interesting for fibre tracking applications, and provides a gain in SNR (Jones et al., 1999; Papadakis et al., 1999).
Along with uniform sampling of the diffusion space, advanced diffusion analysis and fibre tracking methods require a specific number of gradient directions and a minimum b value (Tournier et al., 2009), introducing constraints on their application in specific environments.

Since the display, meaningful measurement, and interpretation of 3D image data with a 3×3 diffusion matrix at each voxel is a challenging task, it is desirable to distill the image information into simpler scalar maps correlated to biophysical properties of tissues (Le Bihan et al., 2001). These parametric maps are computed voxel-wise starting from DT eigenvalues λ_1, λ_2, λ_3, corresponding to the diagonal term of the Diffusion Tensor D_{xx}, D_{yy}, D_{zz}, respectively.

Mean Diffusivity (MD) is a measure of the overall average molecular motion in a voxel independent of any tissue directionality. It is computed as follows:

$$MD = \frac{\lambda_1 + \lambda_2 + \lambda_3}{3} \tag{2.5}$$

Typically, MD is higher in damaged tissues as a result of increased free diffusion. For example, MD maps can highlight variations of water diffusivity in ischaemic regions very early after the ischaemic event, well before the appearance of abnormalities in conventional MRI, allowing to intervene when brain tissue is still salvageable (Le Bihan et al., 2001; Warach et al., 1992).

Axial Diffusivity (AD), measures the average diffusion along the main diffusion direction of the axons. It often stands for axonal architecture.

$$AD = \lambda_1 \tag{2.6}$$

Conversely, Radial Diffusivity (RD) quantifies the average diffusion along the direction perpendicular to the main diffusion direction of axons. It is commonly considered a marker of myelin integrity.

$$RD = \frac{\lambda_2 + \lambda_3}{2} \tag{2.7}$$

Another important index is Fractional Anisotropy (FA), which describes the degree to which the distribution of diffusion in a voxel is directional. Mathematically, FA is defined as the normalized variance of the eigenvalues of the tensor. Generally, in case of pathology, FA decreases due to the loss of coherence in the main preferred diffusion direction. This parameter has also shown to be proportional to the myelination of WM fibres in a voxel: for this reason, FA maps are often used to measure myelin integrity for microstructural WM analysis or brain maturation mapping in neonates and infants (Le Bihan et al., 2001).

$$FA = \sqrt{\frac{3}{2}} \sqrt{\frac{(\lambda_1 - MD)^2 + (\lambda_2 - MD)^2 + (\lambda_3 - MD)^2}{\lambda_1^2 + \lambda_2^2 + \lambda_3^2}} \tag{2.8}$$

From the eigenvectors of $\underline{D}$ we can also infer information about the directionality of the diffusion in a voxel, by assuming that the direction of the fibres is collinear with the first eigenvector v_1 associated with the largest eigenvalue λ_1. By selecting for each voxel, the first eigenvector of the voxels' DT, we obtain a vector field which can be used as input for

tractography algorithms to produce a reconstruction of the major WM fibre pathways in the brain, often represented using a Red-Green-Blue (RGB) color map and of considerable interest both clinically and functionally.

2.2.1 Limitations of DTI

DTI is by now the standard method for dMRI for its ease of application and robustness, routinely applied in clinical settings thanks to its feasibility in terms of acquisition protocol and timing.

However, it presents several drawbacks. The most significant is the so called "crossing fibre" problem: DTI assumes single main direction in each voxel so it cannot resolve two or more fibres crossing in a single voxel. This limitation poses the issue of correctly reconstructing voxels containing more complex configuration of fibres, such as crossing or "kissing" tracts - two fibre populations meeting and then separating again in the same voxel- and other multiple-fibre configuration. This is particularly important since it has been shown that about 90% of WM voxels in the brain contain multiple fibre tracts (Jeurissen et al., 2013). This in turn confounds interpretation of DTI measurements for diagnostic and therapeutic applications.

In the last decade, several methodologies of advanced diffusion analysis have been developed to solve this problem (Daducci et al., 2013; Tournier et al., 2011), for which computational efficiency and applicability in clinical environment have to be assessed. Some of the reasons for this missed adoption are scan times unfeasible for the clinical application, software and hardware availability and acquisition constraints (Farquharson et al., 2013).

Among the many higher-order models overcoming the limitations of DTI, Diffusion Kurtosis Imaging (DKI) (Jensen et al., 2005) has emerged for its improved sensitivity and specificity in detecting developmental and pathological changes in neural tissues combined with robustness to crossing-fibres effects and relatively easy implementation (Arab et al., 2018; Steven et al., 2014).

2.3 Diffusion Kurtosis Imaging

In an attempt to overcome limitations of DTI model, several microstructural models have been recently conceived providing a direct link between diffusion properties and specific microstructural features (Assaf and Basser, 2005; Jespersen et al., 2007; Nilsson et al., 2012; Zhang et al., 2012). However, the validity of these models may be compromised by improper

assumptions in their complex mathematical formulation (Henriques et al., 2019; Lampinen et al., 2017).

An alternative to avoid misleading interpretations is represented by phenomenological models, offering a complete characterization of water diffusion in biological tissues through a simpler mathematical expression containing parameters that do not directly relate with the biological tissue microstructure (Novikov et al., 2018).

Among them, one of the most popular is DKI, an extension of DTI that directly estimates the degree to which water diffusion deviates from a single Gaussian component (Jensen et al., 2005). Indeed, although DTI model hypothesizes an ideal Gaussian profile for diffusion of water molecules within every voxel, the presence of physiological boundaries (e.g., cell membranes or myelin sheaths) and obstacles (e.g., organelles, macromolecules) makes this diffusion far from Gaussian.

DKI precisely quantifies this excess-kurtosis and is thus able to probe tissue microstructure in a more faithful and sensitive way (Fieremans et al., 2011; Jensen and Helpern, 2010; Jensen et al., 2005). This in turn implies that the scalar measures provided by DKI closely relate to microstructural alterations in both healthy and pathological tissues providing more sensitive and specific markers for tissue injury than DTI data alone (Fieremans et al., 2013; Grossman et al., 2012; Huber et al., 2019; Hui et al., 2012; Lin et al., 2018; Marrale et al., 2016; Rudrapatna et al., 2014; Steven et al., 2014; Zhu et al., 2021). Furthermore, DKI provides more accurate information than DTI for tractography applications by resolving more complex fibre configurations of interest (Glenn et al., 2015a, 2016; Henriques et al., 2015; Jensen et al., 2014; Lazar et al., 2008).

The DKI model is obtain through a 2nd order expansion in the diffusion-weighted signal expression of Equation 2.4:

$$S = S_0 \cdot e^{ -\sum\limits_{i=x,y,z}\sum\limits_{j=x,y,z} \boldsymbol{b}_{ij}\boldsymbol{D}_{ij} + \sum\limits_{i=x,y,z}\sum\limits_{j=x,y,z}\sum\limits_{k=x,y,z}\sum\limits_{l=x,y,z} \frac{1}{6} \boldsymbol{b}_{ij}^2 \boldsymbol{D}_{ij}^2 \boldsymbol{K}_{ijkl} } \tag{2.9}$$

Where $\underline{\boldsymbol{D}}$ is the diffusion tensor and $\underline{\boldsymbol{K}}$ is the diffusional kurtosis tensor. In analogy to DTI, the DKI model can in turn be described through a set of linear equations and solved for the six independent parameters of $\underline{\boldsymbol{D}}$ and fifteen independent parameters of $\underline{\boldsymbol{K}}$, since it is axially symmetric (Lu et al., 2006; Tabesh et al., 2011). In addition, at least three b values are required (one $b = 0$ along with two non-zero b values).

Indeed, contrary to DTI, higher-order diffusion models, including DKI, require multi-shell High Angular Resolution Diffusion Imaging (HARDI) sequences (Descoteaux, 1999), typ-

ically involving several high *b* values distributed on a high number of gradient directions, grouped in shells.

Obviously, this implies longer acquisition times, straining the feasibility of advanced dMRI methods of such kind in certain clinical environment due to time constraints (typical scan times are in the order of 20 min).

Nevertheless, research efforts are focused on making this technique feasible within routine protocol since it has turned out to be extremely beneficial to study microstructural changes in a number of preclinical and clinical research populations.

As the acquisition protocol used to obtain a DKI dataset includes all the information necessary to derive a standard DTI dataset, it can be used to calculate both types of indices. DKI measures include the Kurtosis Fractional Anisotropy (KFA) (Glenn et al., 2015b), Mean, Axial and Radial kurtosis (MK, AK, RK, respectively) (Jensen and Helpern, 2010). These measures quantify the degree of non-Gaussianity and can be regarded as indices of tissue compartmentalization or complexity.

In analogy to the definition of MD, MK is defined as the average of directional kurtosis coefficients across all spatial directions, traditionally considered an index of overall microstructural complexity and compartimentalization.

For voxels containing well-aligned structures, RK is defined as the average of the directional kurtosis across all directions perpendicular to the main direction of fibres. It stands for microstructural complexity along perpendicular diffusion direction of fibres.

Conversely, AK is defined as the directional kurtosis along the main direction of well-aligned structures: it reflects microstructural complexity along main diffusion direction.

Finally, analogs to the FA of the diffusion tensor, KFA quantifies lower to higher kurtosis tensor anisotropy in a range between 0 and 1.

Chapter 3

Challenges and peculiarities of Neonatal Imaging

Several methodological challenges specific to imaging the neonatal population have been capturing reasearch's interest in the very last decades. These issues need to be addressed by putting in place specialized protocols and methodologies for data acquisition and processing (Arthurs et al., 2012; Dubois et al., 2021).

3.1   Motion and Sedation

The most relevant artifact introduced by neonatal imaging is motion. Indeed, it is about uncooperative patients, for which sedation is not often an option: in most centers, indication to infant sedation is subject to clinical guidelines and avoided for sole research purposes. It is unanimously agreed that oral sedation for MRI in the hands of experienced staff is safe and effective (Beebe et al., 2000; Dalal et al., 2006). However, especially in case of neonates, one may incur either in undersedation, leading to movement artefact and thus to repeat examination under anaesthesia, or in oversedation, manifesting as oxygen desaturation or transient apnoea, especially in preterm infants (Edwards and Arthurs, 2011; Malviya et al., 2000).

Moreover, rapid or irregular respiratory rate, and small-scale anatomy imply that even minimal movements can create motion artefacts that render images suboptimal for diagnosis. Different solutions can be adopted to address motion artifacts, ranging from: (i) using short acquisition sequences that can be run during a routine protocol not exceeding 30-45 minutes, (ii) to opting for motion-tolerant acquisition and reconstruction approaches explicitly

designed for this hard-to-image population, and (iii) to making the MR environment as patient-friendly as possible through the use of special settings and careful patient preparation.

3.2   Acoustic Noise

One of the most significant disadvantages of MRI is acoustic noise. The primary source of noise is the gradient magnetic field that occurs during the rapid current changes within the coils. The latter bend and vibrate against their mountings, causing a low frequency vibration (McJury PhD and Shellock PhD, 2000).

Consequently, exposure to a typical MR examination without ear protection can induce transient or permanent hearing loss because of the short but intensive noise exposure (Medicines and Agency, 2015), especially for infants. Noise levels largely vary according to the MR sequence but are directly proportional to the static field strength.

A recent and most effective alternative solution to noise protection devices consists in directly mitigating the source of the noise rather than relying on hearing protection in a noisy environment. This can be achieved through development of the so called "quite scanners" (Ljungberg et al., 2021), MR scanners which, by padding or suspending gradient coils within their mountings, do not generate the same levels of acoustic noise.

Adapting imaging sequence technique also has an impact on MR acoustic noise. Indeed, the use of fast parallel-imaging techniques can reduce acoustic noise, by using fewer Radio Frequency (RF) pulses and allowing gradients to vary more slowly. Nonetheless, these imaging techniques are not necessarily always available on standard imaging systems.

3.3   Thermoregulation

Another natural problem for neonates is thermoregulation, particularly if preterm (Waldron and MacKinnon, 2007). This consists in heat loss through evaporation, caused by functionally immature skin and minimized through humidity-controlled incubators.

Because of this, young infants may not be able to sufficiently maintain their temperature during MRI. Improved temperature monitoring of an MR room or wrapping the infant in a prewarmed sheet can help thermoregulation as well as provide additional comfort for the infant.

3.4 Radio-Frequency Heating

The main biological concern during MRI is that of heating, generated by RF pulse-related energy deposition in patient's tissues.

The average rate at which the RF field deposits energy in a given mass of tissue is named Specific Absorption Rate (SAR) and is regulated by international guidelines. The amount of RF energy deposited depends on many factors, including patient size, RF coil design, the body part imaged, the static field strength and the exact pulse sequence, therefore being difficult to predict precisely (Wang et al., 2007).

In adults, risk of SAR effects is low since heat is dissipated through normal thermoregulatory mechanisms such as peripheral vasodilatation, without noticeable local or systemic impact. Conversely, in infants with immature thermoregulatory systems, additionally affected by anesthesia, risk to reach SAR limit is more real.

SAR reduction is therefore a very important factor in all aspects of pediatric imaging, in particular at higher magnetic field strengths (Dagia and Ditchfield, 2008). Since SAR increases with the square of the field strength, some ways to limit its level would be resorting to lower field strengths, reducing the number of slices, having a delay between sequences, using parallel-imaging techniques, or special RF coil designs restricted to the body part of interest.

As request for MRI of neonates and infants increases, simulated modelling SAR for different clinical settings will play a vital role in developing new and more sophisticated dedicated coils.

3.5 MRI Safety and Compatibility

The greatest safety risk for children within an MR environment consists in the accidental interference of the MRI scanner with ferromagnetic metals. Indeed, pathological neonates may have additional requirements, such as ventilation or intravenous access, which must necessarily be both MR-safe (not containing ferromagnetic material and thus posing no additional risk to the patient) and MR-compatible (keeping functionality when exposed to a strong magnetic field) (Stokowski, 2005).

However, using MR-compatible devices may affect device accuracy. An example is represented by MR-compatible infusion pumps, which may not be precise enough for the neonatal population, since a 5% accuracy of pump infusion is recommended in the neonatal environment (Gnanalingham et al., 2005).

Infusion pumps that are specifically calibrated for neonatal use (but not MR-compatible) can be used outside the scanner room with lengthy extension sets attached, although this may introduce a risk of infection, as well as disrupt continuous infusions.

3.6 Small-Scale Anatomy

Another issue is represented by the small size of cerebral structures, which requires an increased spatial resolution to avoid significant Partial Volume Effects (PVE) (Lévy et al., 2015). Besides, incomplete maturation of the infant's CNS tissues implies different tissue characteristics than those of the adult, resulting in different values of MRI contrasts (e.g., T_1, T_2, diffusivity relaxation times).

To this end, MR sequences must be adapted to newborns to obtain relevant good soft-tissue contrast. Moreover, resorting to dedicated coils, designed in relation to the size of the area to be imaged, allows to maximize the image SNR (Hughes et al., 2017b; Lopez Rios et al., 2018).

Precisely because MR signal and contrast differ from the adult, resorting to age-specific, dedicated image postprocessing tools is also crucial (Barkovich et al., 2019).

3.7 Radio-Frequency Coils

RF coils, used to detect the very weak signals from the scanned subject, are a key factor in determining image quality, signal homogeneity and spatial resolution in MR imaging.

Beside the body coil, a large-diameter coil built into every scanner bore and ensuring a relatively uniform excitation field at the expense of signal reception, most MR scanners are equipped with smaller receive-only coils to increase the signal from a precise area of interest. These have the advantage of reducing the required RF power for a given flip angle, due to their smaller size, at the expense of a less uniform excitation field.

Some centers still use adult head or knee coils for paediatric head or body imaging (Helle et al., 2011). Nevertheless, larger adult RF coils tend to increase overall SAR, due to increased energy deposition over a larger body area, and give suboptimal SNR. As a result, the recent development of dedicated pediatric coil technology is increasingly taking hold.

3.8   MR Sequence Optimization

Another primary aspect to consider in neonatal brain and body imaging is the design of dedicated imaging sequence protocols, aimed to balance good image quality with minimal disturbance to the infant, taking into account also current SAR limits.

Neonates require specific conventional sequence parameters compared to adults, as the neonatal brain contains relatively more water than the adult brain. This implies the need for heavier T_1 and T_2 weighting, which in turn means longer TR and TE.

Moreover, high-resolution imaging is critical with limited SNR from the small structures in the neonatal brain as well as SC. For this reason, regarding structural imaging, 3D isotropic volumetric sequences are preferred, giving better contrast-to-noise and WM/GM differentiation (Conklin et al., 2008), and offering reduced overall examination time compared with acquiring in all three planes separately.

3.9   Diffusion MRI

Some other methodological issues are strictly linked to dMRI itself which, as for structural approaches, requires optimization of acquisition parameters, and is particularly sensitive to subject motion.

Because of the high water content and the low myelination degree, diffusion properties of the immature CNS show developmental specificity (e.g., higher diffusivity values and lower anisotropy values) compared with children and adults (Dubois et al., 2014).

For dMRI, EPI sequences or related variants are preferred for data acquisition because of their speed, and acquisition time can be further reduced thanks to the recent advent of Multi Band (MB) acceleration technique (Nunes et al., 2006).

Typical pediatric dMRI data require a proper acquisition protocol made up of low angular resolution, low b values (around 700 s/mm^2) and few gradient directions so as to minimize acquisition time.

Nevertheless, this forced time minimization clashes with specific requirements of advanced diffusion methods in terms of acquisition sequences. Indeed, HARDI sequences, made up of several high b values distributed on a high number of gradient directions, provide an accurate estimation of the diffusion model at the expense of acquisition time, thus straining the feasibility of advanced dMRI methods in pediatrics.

Dedicated time-efficient acquisition framework representing a trade-off between minimization of scan time and accuracy are at the heart of current research in the field.

Resorting to optimized acquisition sequences (Andre and Bammer, 2010), often combined with state-of-the-art techniques such as parallel-imaging (Fruehwald-Pallamar et al., 2012) and MB, can significantly increase acquisition speed and reduce artifacts. However, these advanced technologies are not always available in a real clinical scenario due to high costs and technical limitations.

Given the delicate relationship between advanced dMRI models and clinical needs, preprocessing plays a vital role in neonatal dMRI studies. Indeed, a robust, comprehensive and accurate correction of image artifacts is crucial to ensure reproducibility and accuracy of subsequent quantitative analysis. Specifically, correcting for motion artifacts is a prerequisite, whether regarding intraslice or intravolume artifacts resulting from a sudden movement, or spatial drifts observed between volumes corresponding to different gradient directions.

Finally, if for adults, universal templates can be suitable for a wide variety of applications and populations, definition of normative age- and population- specific diffusion atlases is essential to account for the dramatic morphological developmental changes and perform group comparisons or detect anomalies as reliably as possible.

3.9.1   Noise in Diffusion MRI

The fidelity of inferred biological microstructures through dMRI is limited by the substantial noise present in its acquisitions, due to numerous factors including thermal fluctuations, so that the noise confounds both qualitative (visual) and quantitative (microstructure and tractography) analysis.

In addition, higher b value required by HARDI schemes contribute to lower SNR in dMRI images, given the inverse relationship between diffusion weighting and SNR (Xie et al., 2015). This makes higher-order diffusion models, such as DKI, even more sensitive to low SNR.

Moreover, latest parallel-imaging techniques, conceived to reduce acquisition time, and thus extensively employed in pediatrics imply a moderate signal-to-noise penalty. These include accelerated acquisitions (e.g., partial k-space (Storey et al., 2007), MB imaging, and compressed sensing (Paquette et al., 2015)),

Furthermore, with new acquisition schemes or diffusion-encoding strategies, the sources and distribution of the noise can vary, making it difficult to model and remove.

Indeed, these cutting-edge acquisition methods make the signal distribution deviate from theoretical cases so that making a-priori assumption about noise profile (Koay et al., 2009; Tabelow et al., 2015; Veraart et al., 2016) leads to misestimation of the true signal distribution

with a detrimental effect on subsequent processing steps such as bias correction, denoising or diffusion model estimation.

Nevertheless, especially in routine clinical settings, appropriate modelling of signal and noise distributions often requires information about the acquisition and reconstruction processes not directly available from the scanner. It is hence of utmost importance to identify a suitable denoising approach, able to faithfully characterize the noise distribution directly through information from the magnitude data itself only. This issue is further complicated in case of neonatal imaging, with a comparatively lower SNR due to the relatively higher overall free water content (Pietsch et al., 2019).

Denoising is therefore a vital processing step for neonatal dMRI data prior to anatomical inference and crucial in clinical routine: in medical imaging, better denoising allows for higher quality images with fewer or shorter acquisitions, potentially making advanced acquisition schemes clinically viable, allowing for new bio-markers, and visualizing fine structures such as the SC.

3.10   Spinal Cord

Aforementioned issues and specificities are generally referred to neonatal MRI or dMRI imaging on the brain areas. Imaging of neonatal SC district presents additional ad-hoc criticalities and relative challenges, so that making the MR experience more neonate-friendly is further more demanding (Vargas et al., 2021, 2018).

Although this topic will be extensively addressed in the dedicated Chapter 7, we briefly anticipate the most relevant factors contributing to technical limitations to diffusion analysis of the SC.

The small cord volume leads to a low SNR; CSF pulsation and blood flow can produce prominent ghosting artifacts and degrade image quality; respiratory and cardiac movements cause image blurring and increased or decreased signal intensity; susceptibility artifacts occur at different tissue interfaces (bone, soft tissue, or fluid); anatomical arrangement of WM and GM is reversed from that of the brain; swallowing or related motion artifacts are mostly seen when imaging the cervical SC (cSC).

These challenges multiply in pediatric imaging: anatomic structures are even smaller in children and create a further difficulty in terms of available signal as well as limit of resolution, especially in the presence of anomalies.

Thus, fast, reliable, high-resolution artifact-free and reproducible imaging within minimal scan time is imperative to scan pediatric subjects.

An important factor to be considered for optimizing the image quality against the effects of field inhomogeneity is a suitable choice of pulse sequence. Echo planar sequence, where the whole of k-space is acquired after a single excitation pulse, including all its variants, is the preferential sequence for SC, commonly used in clinical practice. While this sequence offers short acquisition times, which reduces motion-related artifacts, it is are highly sensitive to susceptibility artifacts and eddy-current distortions.

Recent work using reduced Field-of-View (FOV) imaging sequences showed great reduction in geometric distortions when imaging the SC (Finsterbusch, 2009; Wilm et al., 2007). This approach takes advantage of the small-diameter SC morphology and applies a relatively small rectangular FOV to the area of interest.

3.11   Take-Home Message

To sum up, providing general, universally valid recommendations for the neonatal setting is difficult since closely dependent on the question being asked, the clinical or research context, and the available acquisition time for protocol.

Quality control procedures are essential to ensure the biological reliability of MRI observations, especially in case of cohorts with a large number of subjects and different ages, or groups of newborns with different early pathologies.

Moreover, several solutions conceived to address inherent challenges are not readily available in a real clinical scenario, due to technical or financial reasons. As a result, balancing patient care with optimal image quality is as critical as crucial.

Chapter 4

The role of diffusion MRI in Neonatal Imaging

During the pre- and peri-natal period, various insults - such as hypoxia-ischemia, infection, and exposure to toxic substances - as well as genetic abnormalities affect neurodevelopment. Preterm birth and low birth weight are additional risk factors for brain impairment. However, if in severely damaged babies abnormal symptoms appear immediately after birth, a symptom-based diagnosis is extremely difficult in case of neonates with mild to moderate brain damage. In such a case, timely detection and characterization of brain disruption is crucial to prevent long-term disabilities.

In this respect, the advent of dMRI has litterally revolutionized the ability to investigate longitudinal brain development and growth (Oishi et al., 2012; Pietsch, 2018).

In the last decade, investigators have extensively resorted to dMRI to study the rapid changes in microstructural properties of WM and GM non-invasively with added precocity, conspicuity, specificity, and prognostic value to the conventional MRI data (Yoshida et al., 2013).

The unique sensitivity to cellular organization, cortical development, neuronal migration and myelination occurring during the third trimester and the neonatal period has made dMRI the tool of choice for studying WM development and the early detection of injury. Indeed, when interpreted concurrently with conventional MR imaging and other advanced MR imaging techniques, dMRI can facilitate an accurate diagnosis, provide important information about pathophysiology and prognosis of the diseases, and guide adequate therapeutic modalities. Only as an example, thanks to its sensitivity to axonal geometry, dMRI provides superior anatomical information about pre-myelinated brains and the monitoring of axonal injuries,

outperforming T_2 maps, which often cannot even differentiate WM and GM due to the incomplete myelination in neonates (Rodrigues and Grant, 2011).

4.1 DTI in Neonatal Imaging

As already mentioned, DTI is a technique that provides an unprecedented noninvasive imaging approach to assess WM tractography and integrity in the brain.
DTI has by now become a gold standard not only in research but also in clinical practice mainly thanks to methodological advances, such as accelerated data acquisition (Barth et al., 2016) and motion correction algorithms, which have substantially shortened the acquisition times of DTI to under 5 minutes.

Consequently, the use of DTI in newborns and children has substantially increased in the last years (Hu and McAllister, 2019). In pediatric populations, DTI has been employed to study WM injury in patients with hypoxic ischemic encephalopathy (Li et al., 2017b), autism (Walker et al., 2012), as well as congenital heart diseases (Karmacharya et al., 2018). Other investigators have exploited DTI to study WM development in the corpus callosum and language regions of the brain in preterm neonates (Malavolti et al., 2017). Moreover, the impact of nutrition modality on brain WM development has been assessed (Schneider et al., 2018). Finally, population-based studies have used DTI to establish normative atlases and templates for WM development (Feng et al., 2019).

4.2 HARDI in Neonal Imaging

If DTI is still the most widely used dMRI analysis approach in the developing brain, routinely obtained within most radiology departments in their standard-of-care brain protocols, more recent approaches have moved beyond the tensor model to study tissue microstructure more specifically.

Whereas whole-brain DTI can be performed in a reasonable time, these techniques pose additional challenges in neonatal imaging. Indeed, they require high b value (typically > 2000 s/mm^2) and longer acquisition times, which may lead to motion-corrupted data, reduced SNR, and increased distortions. However, recent advances in data acquisition and hardware, such as the use of protocols designed specifically for neonates using neonatal head coils and MB coupled with modern gradient coil systems (Hutter et al., 2018), now enable - if available in the hosting center - HARDI data to be acquired in a clinically feasible time.

Applying these cutting-edge imaging methods to investigate pediatric subjects is gaining increasing popularity within the scientific community precisely for undisputed advantages with respect to DTI. Indeed, advanced dMRI models turn out to be ideal to improve our understanding of the neural substrate associated with impaired brain development in this population, and not detectable with the same degree of sensitivity by structural MRI or DTI (Pecheva et al., 2018).

To prove this, large-scale studies (such as the developing Human Connectome Project, http://www.developingconnectome.org) are now underway and are obtaining high *b* value HARDI data in the neonatal brain with the aim of improving our understanding of human brain development and the impact of environmental and genetic factors on brain development.

Among elaborate models recently proposed to analyze multishell HARDI data, DKI, Neurite Orientation Dispersion and Density Imaging (NODDI), and Constrained Spherical Deconvolution (CSD) (Tournier et al., 2007) have emerged the most (see Appendix A for details).

4.2.1 White Matter Connectivity

As early as the preterm period, the organization of main fibre bundles is clearly delineated on DTI directionality maps showing the main direction of the diffusion tensor.

However, the ones based on simple diffusion models (e.g., DTI that only considers a single fibre population per voxel) present major limitations, leading to biases such as false negatives (premature termination of a tract) or false positives (switch of a tract to a neighboring one). It is only by resorting to the most sophisticated tools, requiring HARDI data and fibre Orientation Distribution Function (fODF) estimation, that one can hope to explore structural connectivity with the best anatomical reliability.

Compared to diffusion tensor imaging, fODF-based analysis using the CSD technique allows delineating more complex WM bundles in neonates, such as in the corona radiata, the arcuate fasciculus and cerebellar–cortical pathways (Dubois et al., 2016), supported by the emergence of a wide variety of ad-hoc tractography tools.

4.2.2 White Matter Maturation

As the connections develop, the WM fibres gradually become mature and functional through the process of myelination, whose successive steps can be measured with dMRI (Dubois et al., 2014; Ouyang et al., 2019a).

The perinatal period is characterised by a pattern of decreasing DTI diffusivities (MD, AD,

RD) and increasing anisotropy (FA) in the cerebral WM in preterm infants (de Bruïne et al., 2011; Kersbergen et al., 2014; van Pul et al., 2012) and term infants (Oishi et al., 2011).

These DTI parameters continue to show intense changes during the first postnatal months in bundles identified by tractography. They are probably sensitive to different mechanisms, such as the proliferation of glial cells, the extension of oligodendrocyte processes, and their wrapping around axonal fibres.

WM maturation follows a heterogeneous spatiotemporal pattern, with different fasciculi maturing at different times and different rates (Braga et al., 2015; Dubois et al., 2008) in a posterior-to-anterior and a central-to-peripheral direction of maturation. Maturation models and observations in fetuses, preterm newborns, and infants (Nossin-Manor et al., 2015; Zanin et al., 2010) support the hypothesis of sequential changes in DTI parameters and suggest two successive steps: (i) early changes in microstructure related to the fibres premyelination would mainly lead to a decrease in AD and RD; and (ii) subsequent wrapping of myelin sheaths around axons would not modify AD but would decrease RD, implying an additional increase in anisotropy.

Beyond DTI, more complex diffusion models have been used to assess WM maturation, such as NODDI, which showed differences between regions in terms of changes in neurite density and orientation dispersion indices in newborns and infants (Dean et al., 2017; Jelescu et al., 2015; Kunz et al., 2014), and DKI, which appeared to be informative in normal development when the estimated intra- and extra- cellular axial diffusivities do not change (Jelescu et al., 2015).

4.2.3   Microstructural Measures in Grey Matter

In addition to assessing WM, dMRI allows very precise in vivo exploration of the GM microstructure.

As regards DTI, cortical maturation up to Term Equivalent Age (TEA) is characterised by decreasing FA and MD, reflecting increased dendritic arborisation and synapse formation and suggesting impaired cortical development in the preterm population (Ball et al., 2013). DTI also allows the microstructural exploration of central GM nuclei in the developing brain (Nossin-Manor et al., 2013; Ouyang et al., 2019a), but there are still few analyses provided with more comprehensive models such as NODDI or DKI.

The NODDI model might be used to better understand the progression of these mechanisms during development (Batalle et al., 2019; Eaton-Rosen et al., 2015), as the neurite density index informs about the cellular and organelle density, and the orientation dispersion

index on geometrical microstructure.

DKI might also provide valuable insights on the cortical microstructure, with continuous decrease in MK over the preterm period (Ouyang et al., 2019b).

Nevertheless, more studies are needed to systematically compare the markers provided by the different diffusion models in the developing brain according to the age of newborns and the cortical regions. Indeed, as with the microstructural evaluation of the WM, systematic model-to-model comparisons are still lacking to assess which are the best markers to reliably quantify microstructural tissue maturation in newborns.

4.3   Neonatal Spinal Cord Imaging

Intrinsic methodological challenges only hinted in Chapter 3 have lead to a significant delay in technological advances and relative research applications for dMRI of SC compared to the brain region.

This is clearly obvious also from the significant lower number of neuroimaging tools specifically conceived for SC in the face of a multitude of brain image processing frameworks. As a result, application of dMRI to this area, especially in its latest techniques, is still far from becoming a common clinical practice in pediatrics.

The efficacy and potential applications of DTI in adult spinal cord are the subject of numerous studies covering a wide range of diseases (e.g. traumatic injury, spinal tumors, cervical myelopathies, amyotrophic lateral sclerosis and multiple sclerosis (MS)) since both DTI metrics and Diffusion Tensor Tractography (DTT) provide additional tissue characteristics not found in conventional MRI (Li et al., 2017a; Wang et al., 2016).

For instance, changes in DTI indices are visualized in regions of the cord which appear normal on conventional MRI and are remote from the site of cord lesion/compression (Vedantam et al., 2014).

Lately, interest in SC DTI has also extended to the pediatric field with promising results, thanks to a protocol that acquires diffusion-weighted images along a limited number of directions (up to 20) with a maximum b value of 700-1000 s/mm^2, keeping the total acquisition time within 8 minutes.

Feasibility of obtaining repeatable DTI parameters has been investigated by (Singhi et al., 2012) as regards pediatric cervical SC and by (Saksena et al., 2016) for the entire spine. The latter demonstrated that DTI can be used as an imaging biomarker to evaluate SC above and below the congenital lesion in syringohydromyelia subjects.

(Saksena et al., 2018), (Mohamed et al., 2011), (Alizadeh et al., 2018) and (Mulcahey et al.,

2013) assessed the utility and effectiveness of DTI and DTT of the pediatric cervical and thoracic spinal cord on subjects with SCI and all proved DTI and DTT good reproducibility and high correlation with clinical scores.

One of the major challenges in dysraphism is to know the morphologic organization of the spinal cord: in a preliminary work by (Antherieu et al., 2019), spinal lipoma was chosen for analyzing the microarchitecture parameters and fibre morphology of the spinal cord by DTI with tractography. Tractography of the conus medullaris in a very young pediatric population (0–8 years old) with a spinal lipoma has turned out to be possible, reproductive, and allows visualization of the spinal cord within the dysraphism.

All these works, however, deal with large pediatric populations and developmental studies and none of them is specifically focused on the neonatal age range.

Even more recently, some studies have begun to emerge aiming to extend advanced dMRI methods, such as DKI or NODDI to SC, too.

In this respect, HARDI techniques can be computed on adults using a moderately expanded diffusion sampling scheme and their metrics can be obtained simultaneously with conventional diffusion tensor-derived parameters.

(Panara et al., 2017) assessed feasibility in terms of repeatability and reproducibility of DKI for microstructural assessment of the normal cervical spinal cord. DKI can provide additional and complementary information to DTI on spinal cord pathology: it has been successfully applied by (Raz et al., 2013) and (Bester et al., 2010) on adult cervical SC (cSC) of patients with MS to characterize lesional and normal-appearing GM and WM damage.

As regards NODDI, (By et al., 2017) investigated the feasibility and utility of NODDI in the cSC of MS patients and found out it provides unique contrast that is not available with DKI or DTI, enabling improved characterization of the spinal cord in MS. In support of the same hypothesis, (Grussu et al., 2017) showed for the first time that neurite orientation dispersion is a new biomarker that uncovers previously undetected layers of complexity of MS SC pathology, scanning at high field four post mortem SC specimens.

Conversely, as it is easy to imagine, pediatric application of advanced dMRI methods is still at its embryonic stage: most of the strategies adopted for obtaining sufficient-quality adult imaging are not easily applicable for infants, much less to the neonatal setting.

To the best of our knowledge, the only published work on pediatric DKI is by (Conklin et al., 2016): they provided mathematical and experimental evidence that DKI can offer additional information about the micromolecular environment of the pediatric spinal cord. A novel DKI imaging sequence based on a tilted 2D spatially selective radio frequency pulse providing reduced FOV imaging was developed, implemented, and optimized on a 3T MRI scanner,

and tested on healthy and SCI pediatric subjects. On the contrary, NODDI does not appear to have been published in a pediatric setting yet.

4.4   Take-Home Message

As far as it concerns neonatal brain, a varied number of ad-hoc tools are emerging, specifically conceived to explore neonatal age range. Indeed, latest technological progresses have contributed to make advanced dMRI models applicable also in early pediatrics.
However, these technologies are not always available in a clinical setting, straining feasibility of beyond-DTI models in everyday clinical practice.

This scenario further complicates in case of SC imaging, given its intrinsic more stringent requirements compared to brain. This is witnessed by the complete lack of studies regarding applicability of HARDI models to infant SC.
Nevertheless, considering promising results coming from the adoption of such cutting-edge methods for infant brain, translation of HARDI to neonatal SC may provide interesting insights about tissue microstructure of this as small as challenging district.

Chapter 5

Organization of the work

Given the plethora of both genetic and accidental injuries affecting the CNS in the early stages of development, the evident difficulties in their diagnosis and the importance of an early intervention, I opted for focusing my PhD path on the attempt to translate advanced dMRI models not only to the neonatal setting but also to a real clinical scenario, aiming to demonstrate feasibility and potential clinical utility of these techniques.

Among various models I chose to primarily dwell on DKI for several reasons.
First of all, I preferred a phenomenological model such as DKI thanks to the lack of constraints on underlying biophysical properties of imaged tissues.
Conversely, compartimental models of biological tissues have been developed for adult brain and thus, at least in theory, not immediately applicable to the neonatal case and in SC district. Moreover, being conceived as an expansion of DTI, DKI turns out to be clinically applicable with less effort than other other higher-order models, allowing to include also standard DTI indices. In addition, compared to DTI, it has shown to represent appropriately the tissue microstructure in the presence of crossing fibres and to outperform DTI-derived measures in terms of tissue specificity. Finally, in a restricted environment, such as SC, diffusion is no longer Gaussian and the tensor model deviates from the signal, being optimally captured by the DKI model.

I thus organized my work as follows. First of all, I stressed the importance of a proper and robust preprocessing as a key factor for successful analysis. Specifically, I focused on denoising, given its crucial role in improving the often sub-optimal quality of diagnostic images. I thus decided to start from well-established adult brain data from HCP release (WU-Minn, 2017) to validate two state-of-the-art denoising methods, both based on adaptive estimation of noise distributions (part I, Chapter 6). I compared their performance applied to fitting the DKI model and inspected the effect of denoising on DKI-related measures

with varying field strengths, with a view to extend Ultra High Field (UHF) MRI to neonatal imaging.

I then made use of the conclusions drawn from this study to implement the most suitable denoising method in the two following works, starting from data acquired at Neuroradiology Unit of Gaslini Children's Hospital, which formed the core of my PhD path.

Specifically, I focused on filling the gap about investigations on infant SC, by implementing the first semi-automated pipeline for handling with DKI data of neonatal spinal cord (Part II, Chapter 7), from setting of a dedicated acquisition sequence to extraction of diffusion measures, through accurate adjustment and adaptation of processing algorithms customized for adult SC. The design of this pipeline has reckoned with all the technological and methodological issues posed by infant imaging, which strains the feasibility of advanced diffusion imaging methods due to the strict clinical requirements. Applicability and clinical validity of proposed method has been evaluated analyzing a preliminary clinical case-study concerning Periventricular WM Injury (PWMI), a condition common to preterm birth.

Finally, I worked on neonatal brain (Part II, Chapter 8), by creating a customized neonatal image processing pipeline from a combination and adaptation of existing tools. I then used it to characterize differential neurodevelopment between pre-term and term-born subjects through extraction of representative features from multiple advanced diffusion MRI microstructural models and using both standard group-level and Machine Learning (ML) approaches.

Part III, Chapter 9 contains a discussion of the main results of this work of thesis, and a brief explanation of the future research activity which is the natural continuation of this work.

At the end of this thesis, Appendix A describes in more depth the advanced dMRI methods I have used in this work besides DTI and DKI; Appendix B contains supplementary material for the work described in Chapters 6,7,8; finally, Appendix C resumes all relevant publications to this work.

Part II

Denoising as a crucial step in Diffusion MRI

Chapter 6

Influence of adaptive denoising on Diffusion Kurtosis Imaging at 3T and 7T

6.1 Background

The aim of this first part of the work was to investigate the impact of denoising on DKI-related markers with varying field strength, from 3T to 7T. Indeed, while most MRI studies in neonates and infants currently resort to 1.5 or 3T MRI scanners, UHF MRI (e.g., 7T) would also be a promising perspective for mapping, at higher spatial resolution, fine structures in development, or microlesions not detectable with 3T MRI. This is a hot topic that some collaborative research and clinical groups have begun to address, but which triggers additional constraints and challenges.

Higher-order diffusion models would definitely benefit from introduction of UHF in clinical routine. For instance, DKI's sensitivity in microstructural abnormalities associated with disease can be further increased by acquiring DKI at higher magnetic field strengths than routine 1.5T, as the higher field strength increases the SNR (Heidemann et al., 2010), improving MRI spatial resolution and reducing partial volume artifacts.

However, UHF strength suffers from increased sources of artifacts than standard magnetic field strength. Indeed, it is also characterized by shorter T_2^* (and consequently shorter T_2) and increased field inhomogeneity, which may offset the advantageous increase in SNR (Van Essen and Ugurbil, 2012). Field inhomogeneity implies increased image distortion and shorter T_2^* consequent blurring and signal loss with long echo trains in EPI, frequently used as a readout sequence. Additional ghosting artifacts can be introduced because fat suppression may be compromised due to field inhomogeneity, as well as motion and physiologic noise artifacts which may become more prevalent with 7T.

Since exploiting combined advantages of DKI imaging technique and scanning at UHF may have potentially relevant clinical implications, the first crucial aspect we wondered about was variability of DKI-derived biomarkers from standard 3T to 7T.

In principle, the diffusion properties of water in biological tissues should not be affected by the scanner field strength. However, field intensity influences the relative SNR in the image data, possibly leading to sources of bias and instability in the estimates of diffusion measures (Alexander et al., 2006). In addition, the effect of both macroscopic and microscopic susceptibility-induced gradients on diffusion metrics must be considered (Clark et al., 1999). Local microscopic susceptibility-induced gradients may be originated through spatial variations in magnetic susceptibility along fibre surfaces in a perfectly aligned fibre bundle. Diffusion of water molecules through microscopically inhomogeneous fields leads to a dephasing of nuclear spins which results in an irreversible loss of signal and in a decrease in T_2. This kind of gradients are also known to exist at interfaces between bone and tissue, in tissues, such as liver, spleen and the basal ganglia, that contain intracellular deposits of iron stored in ferritin and hemosiderin (Schenck, 1996) or in pathological iron deposits in the brain linked to severe neurodegenerative disorders like Parkinson's disease (Fujiwara et al., 2014) as well as along myelinated nerve fibres with Ranvier nodes (Palombo et al., 2015). It has been proved that these gradients can have an impact on altering the diffusion tensor measurements (Clark et al., 1999) and the kurtosis ones (Palombo et al., 2015). Indeed, these gradients' magnitude linearly increases with the applied field: as a result, any systematic effects are then field-dependent.

Similar to what was done previously for DTI (Choi et al., 2011; Clark et al., 1999; Fushimi et al., 2007; Hunsche et al., 2001; Moser et al., 2009; Polders et al., 2011), recent studies have attempted to assess field strength dependence also for DKI between 1.5 and 3T. One study has suggested that kurtosis metrics estimation is significantly affected by tissue microstructure, topological rearrangement, and, less remarkably, by magnetic susceptibility (Palombo et al., 2015). Reversely, another research has revealed no significant variation across field strengths (Shaw et al., 2017).

All these findings are quite conflicting, mainly due to different acquisition protocols, hardware configurations, vendors and denoising methods.

In our work, we aim at comparing DKI measures acquired at 3T and 7T, clarifying the discrepancy and ambiguity of existing results starting from a more accurate noise modelling. Given the key role played by the choice of denoising method on subsequent analysis and the issues inherent to UHF, we focused our investigation on adult data from HCP release (WU-Minn, 2017). Indeed, healthy adult data is here used as "baseline" data to test and apply

any processing or analysis method in brain imaging, with a view to extend drawn conclusion from this "ground truth" case to the neonatal setting. To this end, HCP young adult dataset benefits from whole brain dMRI acquired for research purposes, and thus of optimal quality and high resolution.

The ultimate goal of the present paper is exactly to assess the joint impact of two possible sources of bias in estimation of diffusion metrics: magnetic field strength and denoising approach.

Indeed, we believe that, in order to assess the influence of magnetic field strength on variability of DKI maps, noise represents a key factor to take into account. DKI measures are in fact inherently sensitive to low SNR acquisition (Glenn et al., 2015c) and thus proper noise suppression at high field strengths ensures improvement in reproducibility and robustness of DKI biomarkers, of utmost importance in diagnostics.

Noise has usually been statistically modelled in literature attending to the scanner coil architecture as a Rician distribution with constant variance for the whole image, also known as stationary Rician distribution (Veraart et al., 2016). If this model can be adopted for a single-coil acquisition, the reconstruction process carried out by parallel-imaging methods like SENSE (Pruessmann et al., 1999) or GRAPPA (Griswold et al., 2002) yields to a variance of noise value which is dependent on the position within the final image (Aja-Fernández et al., 2014). Hence, the traditional noise estimation methods -e.g., Marchenko-Pastur Principal Component Analysis (MP-PCA)-based (Veraart et al., 2016), founded on a single noise level for the whole image - fail.

This is the case of HCP data, whose image reconstruction uses SENSE1 multi-channel for both scanners, combined with MB technique in order to improve imaging speed and reduce scan time, thus questioning stationarity of noise in the reconstructed data and stressing the need for a proper noise estimator beyond textbook Rician distribution.

Among the multiplicity of existing denoising methods used in dMRI, we opted for choosing as use-case the comparison between two advanced denoising frameworks, representing the state-of-the-art in case of increasingly complex dMRI systems (e.g., multiple channels and complex reconstruction algorithms): Non-Local Spatial and Angular Matching (NLSAM) (St-Jean et al., 2016) and Patch2Self (Fadnavis et al., 2020). These two approaches share two main features: they do not need formulation of an a-priori model for noise, thus ensuring more realistic representations of image features, and they can both be applied at any step in the pre-processing pipeline.

NLSAM is a spatially and angular adaptive denoising allowing to estimate noise distributions as they explicitly depend on the number of coils, making it possible to estimate all unknown

parameters using only the magnitude data: no a priori knowledge is needed from the acquisition or the reconstruction process itself, which is usually not stored or hard to obtain in a clinical setting (St-Jean et al., 2020). Without assuming an a-priori Rician distribution, this framework avoids misestimation of the noise distribution in parallel and MB imaging, being essential also for avoiding errors in subsequent processing steps such as bias correction, denoising and diffusion model estimation.

Conversely, Patch2Self is a recently proposed self-supervised learning denoising method whose unique advantage is the lack of requirement for selecting or calibrating an explicit model either for noise or diffusion signal. The only assumption it relies on is randomness and uncorrelation of noise across different gradient directions. Its framework consists in holding out one volume and using patches from all other volumes to predict the centre of the patches of the held-out volume using a regressor. This denoiser has already showed a significant improvement in repeatability and conspicuity of pathology in diffusion volumes and quantitative DTI metrics for adult brain and SC (Schilling et al., 2021).

6.2 Methods

6.2.1 Data Acquisition

We retrospectively extracted a 30-subjects subset from HCP data release including high-resolution 3T and 7T MR scans from 11 male and 19 female young healthy adult twins (ages 22-35) (WU-Minn, 2017). All participants were scanned using an acquisition protocol as suitable and performing as possible for the magnetic field in question. Nevertheless, differences in the two acquisition procedures are limited and provide also comparable scan times.

We made use of Open Access Data by registering an account at ConnectomeDB and consequently agreed to the Open Access Data Use Terms. Within HCP privacy policy, each patient has first been asked for verbal informed consent and given an extensive telephone interview and later for written informed consent.

Details on scanner hardware, acquisition protocol, artifacts handling, data quality control and pre-processing steps are available at (WU-Minn, 2017) and (Sotiropoulos et al., 2013) and also summarized in Table 6.1, as far as it concerns diffusion imaging.

Table 6.1 HCP Acquisition protocol details for diffusion imaging

	3T	7T
Scanner (Siemens, Erlangen, Germany)	Connectome Skyra	MAGNETOM
Sequence	Spin-Echo EPI	Spin-Echo EPI
TR (s)	5520	7000
TE (ms)	89.5	71.2
FOV (RO×PE)	210×180	210×210
Matrix (RO×PE)	168×144	200×200
Slice Thickness (mm)	1.25	1.05
# Slices	111	132
MultiBand Factor	3	2
Acceleration Factor (iPAT)	–	3
BW (Hz/px)	1488	1388
b-values	1000, 2000, 3000	1000, 2000

6.2.2 Image Processing

Pre-processing steps included minimization of spatial distortions and data alignment across modalities and across subjects using appropriate volume-based and surface-based registration methods. They all were performed in advance by HCP pipeline. Specifically, 3T and 7T diffusion MRI images were pre-processed with a new v3.19.0 version of the diffusion pipeline that supports the use of a new version of FSL's EDDY that adds image slice outlier detection and replacement to remove noise caused by subject movement.

In order to perform analysis based on denoising approach, we consequently applied the two types of aforementioned denoising methods to already pre-processed DWI data at both field strengths. In both cases, we focused subsequent analysis on masked brain scans using a binary mask provided within HCP release. Indeed, masking makes denoising far faster and reconstruction more robust by skipping unnecessary voxels. Moreover, we set the threshold for $b = 0$ shell at 100, given the variability of non-diffusion-weighted b values at both field strengths.

As regards NLSAM, we resorted to 5 angular neighbours, as suggested in (Chen et al., 2019; St-Jean et al., 2020) and automatically estimated both parameters of the noise distribution: the number of degrees of freedom N, related to the number of receiver coils and to the reconstruction technique used - in case of parallel-imaging and MB - and the Gaussian noise standard deviation σ_g relating to the original noise distribution from background in the data. This is possibly by specifying `auto` option as command line input. We used DWI images as a starting point (an alternative is to start from noise maps if available) and we chose to apply

the moments method for estimating parameters, as set by default.

In parallel, Patch2Self denoising implementation in DIPY v.1.4.1 (Garyfallidis et al., 2014) was applied to already preprocessed data with Ordinary Least Square (OLS) as regression method.

We then extracted DKI-derived measures using DIPY v.1.4.1 for noisy and denoised data with both methods. From tensors estimations, the software outcome were parametric diffusion maps for DKI, including MK, AK, RK, and KFA. Since kurtosis measures are susceptible to high amplitude outliers, we opted for removing their impact by limiting metrics' extraction within the typical range $(0, 3)$.

6.2.3   Comparison of denoising approaches

In order to assess the impact of the choice of denoising approach on subsequent diffusion measures within magnetic field strength, we evaluated the denoising performance both qualitatively and quantitatively. To this end, we firstly measured computational efficiency by comparing runtimes required by each of the two methods to denoise a single example subject at each field strength.

We then made a preliminary qualitative comparison, which is important as visual inspection is a crucial part of clinical diagnosis. Indeed, we visually investigated the denoising outcome of NLSAM and Patch2Self against plain pre-processed (noisy) dMRI data along with their corresponding residuals (squared differences between the noisy data and the denoised output). This visual assessment was also extended to DKI parametric maps across subjects, looking for apparent differences between the two methods at fixed field intensity.

We then inspected impact of denoising on microstructure model fitting, a critical step often leading to degenerate parameter estimates due to the low SNR of dMRI acquisitions. We thus assessed the goodness of fit in the three cases (noisy, NLSAM-denoised, Patch2Self-denoised) resulting from fitting the DKI model to a middle axial slice of our data. In order to compare the goodness of each fit, we performed a k-fold Cross-Validation (CV, https://dipy.org/documentation/1.4.1./examples_built/reconstruction/kfold_xval/) (Rokem et al., 2015) for a middle axial slice of masked data. The data has been divided into $k = 3$ different subsets for the selected voxels, and data from two folds have been used to fit the model, which predicts the data on the held-out fold. As standard measure for quantifying the goodness of fit in linear regression models, we computed the coefficient of determination with expression:

$$R^2 score = 1 - \frac{\sum_i (y_i - f_i)^2}{\sum_i (y_i - \bar{y})^2} \tag{6.1}$$

with $y_1, \ldots, y_n \triangleq$ observed values; $\bar{y} \triangleq$ mean of observed values; $f_1, \ldots, f_n \triangleq$ fitted values

Statistical comparison was done by simply subtracting the goodness-of-fit R^2 scores of fitting noisy data from Patch2Self and NLSAM denoised data for DKI model through 2-sided t-test with Bonferroni correction.

Finally, we evaluated ability of denoising method in terms of alleviating degeneracies in DKI maps in specific ROIs. Indeed, models such as DKI are susceptible to noise and signal fluctuations, which can often lead to estimation degeneracies. For group-level comparisons, we used JHU-ICBM atlas (Mori et al., 2008), already defined in MNI space and warped its labels into each subject's diffusion space taking advantage of warping fields provided in advance by HCP data release. We focused on WM since it is more susceptible to these implausible negative estimates near tissue and water boundaries: Corpus Callosum (CC); Anterior Limb of Internal Capsule (ALIC); Posterior Limb of Internal Capsule (PLIC); Anterior Corona Radiata (ACR); Superior Cerebellar Peduncle (SCP). These areas were chosen since containing a high amount of crossing and inter-digitating fibres (Figure 6.1a,b). Potential discrepancies among denoising methods with fixed magnetic field were statistically evaluated through one-way ANOVA using Bonferroni post-hoc procedure for multiple comparisons.

We thus moved on to assessment of the variability of DKI measures at varying both field strength and denoising method. For this purpose, we included in our ROI analysis also GM areas, besides to the WM ones. Indeed, we extracted subcortical automatic segmentation from Desikan-Killiany Atlas (Desikan et al., 2006) available on FreeSurfer (Fischl, 2012) for a total of 4 ROIs: Caudate Nucleus (CN), Putamen (PUT), Globus Pallidus (GP) and Thalamus (TH). These are the most used ROIs for metrics comparison at different field levels (Chung et al., 2016; Shaw et al., 2017) (Figure 6.1c).

In order to evaluate the trend of DKI measures across denoising approach and magnetic field intensity, we displayed violin plots for each DKI map within specific ROI, at both 3T and 7T for noisy as well as for denoised data. A two-way ANOVA was performed to analyse the effect of field strength and denoising method on average DKI measures across ROIs. Pairwise differences across field and denoising approach were investigated through Bonferroni post-hoc procedure for multiple comparisons.
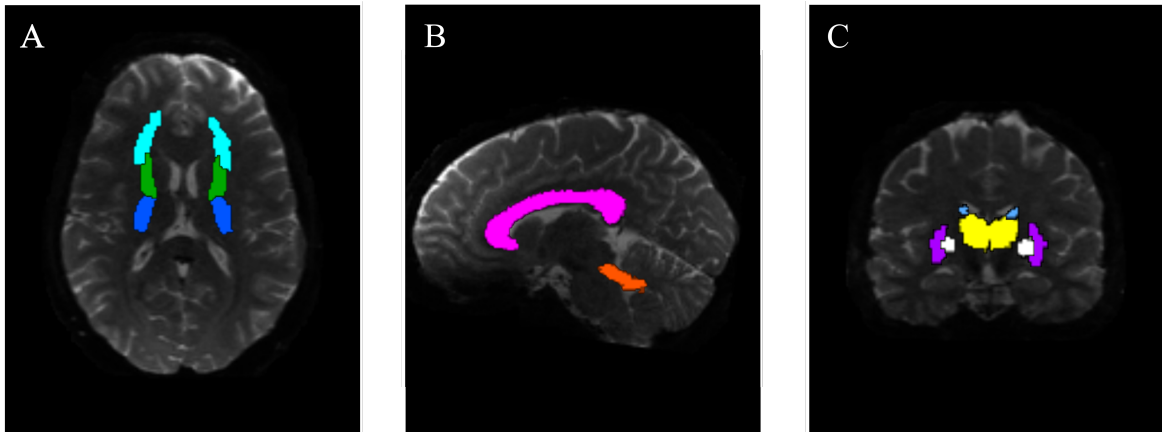
Figure 6.1 **ROIs overlaid on a 3T exemplary DKI image**: White Matter areas including **(A)** Anterior Limb of Internal Capsule (ALIC) represented in Green, Posterior Limb of Internal Capsule (PLIC) in blue and Anterior Corona Radiata (ACR) in cyan, **(B)** Corpus Callosum (CC) in pink along with Superior Cerebellar Peduncle (SCP) in orange; Grey Matter areas such as **(C)** Thalamus (TH) marked in yellow, Putamen (PUT) in Violet, Caudate Nucleus (CN) in light blue and Pallidum (PAL) in white.

6.3 Results

6.3.1 Computational Efficiency

Runtime of the two denoising algorithms in minutes is reported in Table 6.2. Experiments were conducted on a high-performance server with 2.3 GHz 4x24-cores AMD Epyc 7352 CPU, 251 GB DDR4-3200 RAM and 24 GB PNY Quadro RTX6000 GPU.

We can easily notice that the computational time required by NLSAM is twice longer than Patch2Self for 3T scanner, and eight times longer in case of 7T. This is likely due to fairly unoptimized Python implementation inherent to this method and acknowledged by the authors themselves (St-Jean et al., 2016).

Table 6.2 Required runtime in minutes for the compared denoising algorithms on one exemplary subject for both magnetic field strengths.

	3T		7T	
	Patch2Self	**Nlsam**	**Patch2Self**	**Nlsam**
Time (mins)	131	269	40	328

6.3.2 Visual assessment of DKI data and DKI-related measures

First-sight visual inspection of DKI volumes from one representative example subject yet provides us with useful information about denoising behavior with respect to magnetic field strength. For each of the magnetic fields, in Figure 6.2 we show the axial slice of a randomly chosen 3D volume and the corresponding residuals. Nevertheless, this behavior is consistent across all the cohort.

First of all, we can note that both denoising approaches do not show any anatomical features in the error-residual maps, so it is likely that neither are introducing structural artifacts.

At first glance, as regards 3T data, we can observe minor differences between starting noisy image and the ones obtained after application of both denoising methods. NLSAM contribution seems even less relevant than Patch2Self, given the extremely low amplitude of the residual map, which means denoising does not add artifacts nor significantly improves image appearance at standard 3T field intensity.

Conversely, denoising contribution in increasing image quality significantly arises at UHF. Specifically, denoised 7T scans after NLSAM show sharper anatomical details and less background noise. This is even more evident referring to Patch2Self denoising, which seems to present less smoothing and to produce more visually coherent outputs compared to NLSAM.
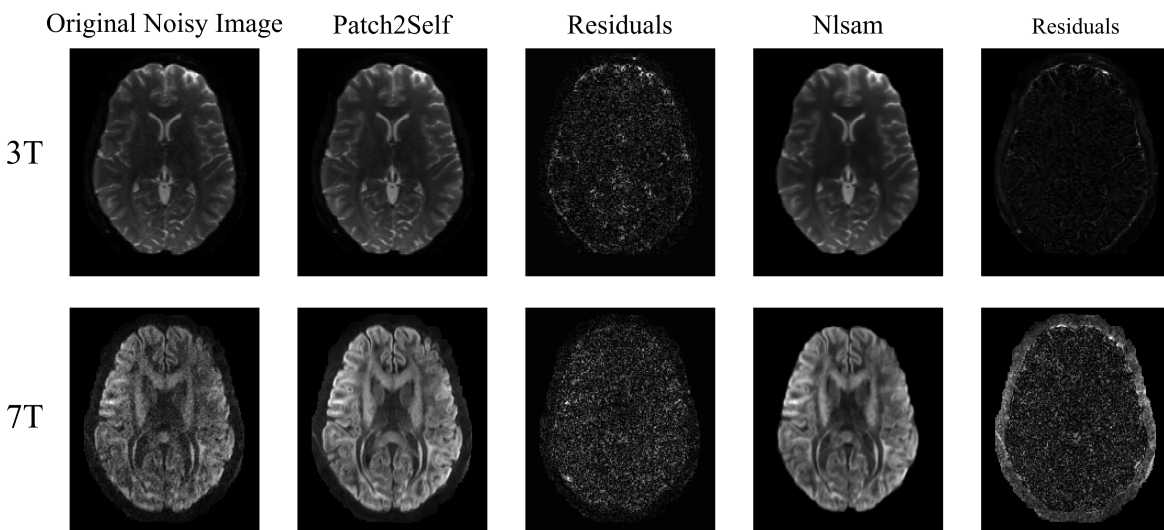
Figure 6.2 **The denoising of Patch2Self and NLSAM is compared against the original noisy image along with their corresponding residuals** on a middle axial representative slice for one example subject. Notice that both denoising approaches at 7T suppress more noise and do not show any anatomical structure in the corresponding residual plots.

As regards removal of degeneracies inherent to DKI fitting, we detected an increasing performance from noisy data to Patch2self and, finally, to NLSAM by inspecting all DKI measures. In Figure 6.3, we compare the effects of different denoising algorithms on DKI parameter estimation by displaying MK maps at both field intensities. Indeed, this is the most representative of this observed trend among all DKI-derived parameters.
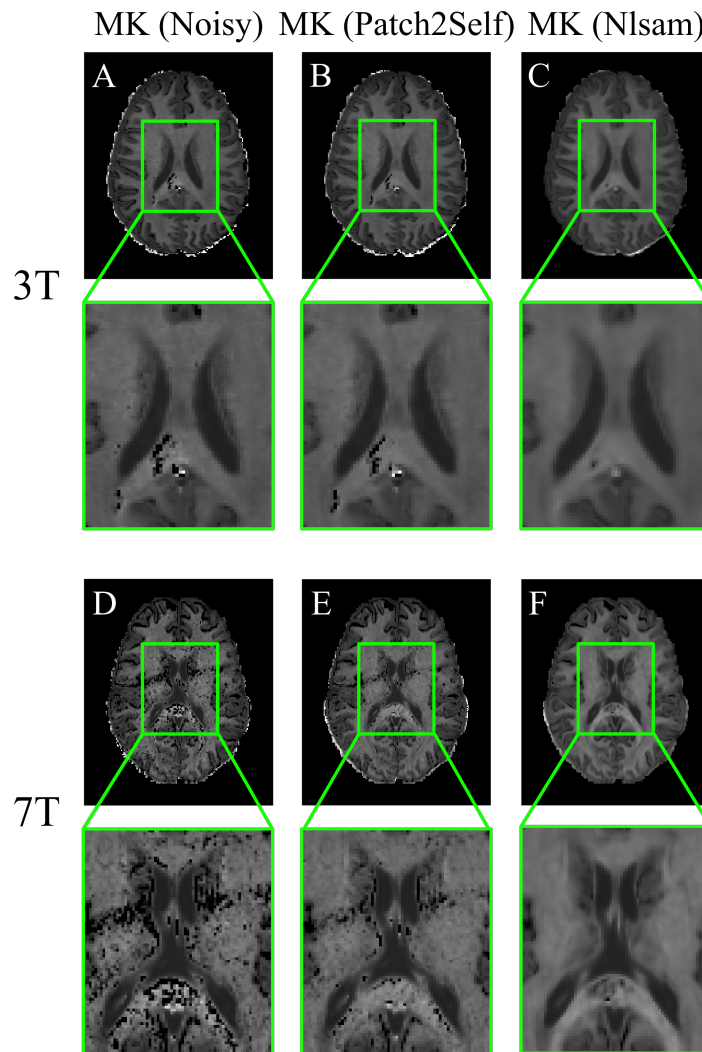
Figure 6.3 **Denoising performance in removal of degeneracies at 3T and 7T on DKI metrics for one exemplary axial slice on Mean Kurtosis (MK) map at 3T and 7T**. Notice that NLSAM **(C,F)** alleviates more degeneracies in model estimation (visible as black voxels in the highlighted region) as compared to noisy (original) **(A,D)** and Patch2Self **(B,E)** denoised data.

6.3.3 Quantitative comparison of the goodness-of-fit

In Figure 6.4a we depict the improvement of the R^2 metric obtained after fitting the downstream DKI model to a middle axial slice for noisy and denoised 3T data with NLSAM and Patch2Self, respectively. We can observe Patch2Self consistently improves model fitting across all voxels compared to NLSAM (two-sided t-test with Bonferroni correction, $p \leq 1.00 \cdot e^{-4}$). The same trend can be observed for the goodness-of-fit R^2 scores relative to 7T data (Figure 6.4b).
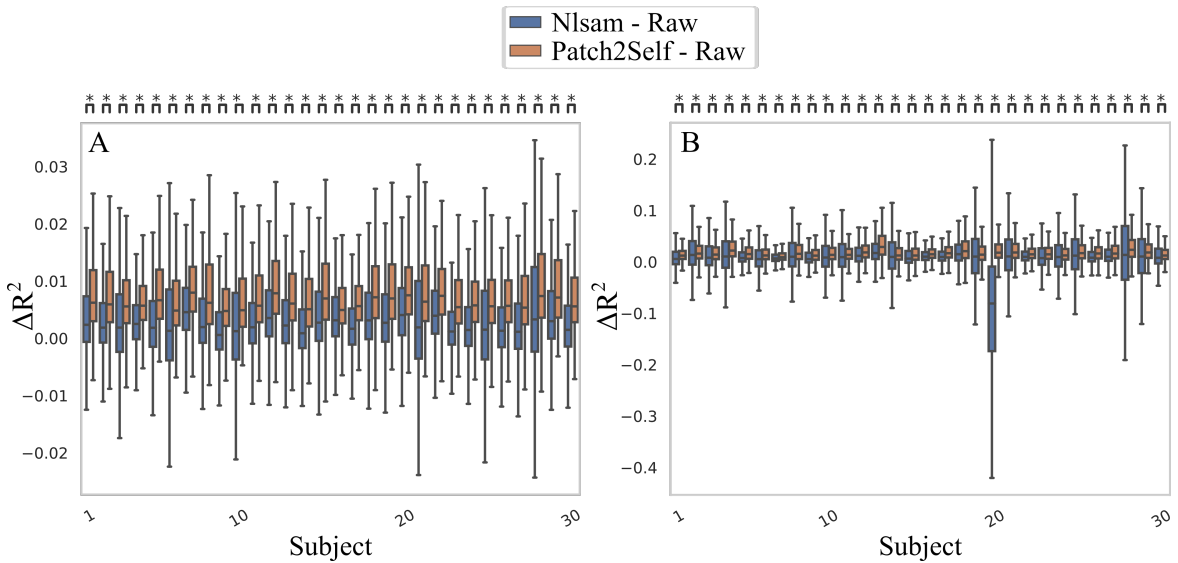
Figure 6.4 **Boxplots quantifying the increase in R^2 metric after fitting downstream DKI model** at **(A)** 3T and at **(B)** 7T. The R^2 improvements in each case are plotted by subtracting the scores of model fitting on noisy data from R^2 of fitting each denoised output. Note that the consistency of microstructure model fitting on Patch2Self denoised data is higher than that obtained from NLSAM. $*$ indicates $p \leq 1.00 \cdot e^{-4}$

Quantitative comparison of degeneracies alleviation

As regards ROI-based analysis, a one-way ANOVA with Bonferroni correction for multiple comparisons was conducted to compare effect of denoising method on the number of degeneracies in WM areas. Figure 6.5 summarizes measurement of the number of degeneracies across WM ROIs for all the DKI parametric maps.

Significant differences found among denoising approach have been observed in all measures, except for KFA, which does not appear to suffer from negative DKI estimates in any ROI. An overall common trend can be observed for most ROIs and metrics: (i) higher range of variability in degeneracies distribution at 7T with respect to 3T for any denoising method;

(ii) at 3T, higher discrepancies between noisy and Patch2Self-denoised data on one side and NLSAM-denoised scans on the other; (iii) in contrast, at 7T, a more relevant differentiation of noisy data from both denoising approaches; (iv) an increasing loss of degeneracies from noisy to Patch2self to NLSAM denoised volumes, respectively, whose most representative example is CC region.

6.3.4 Joint impact of denoising approach and magnetic field on variability of DKI measures

We opted for focusing our investigation about variation of DKI measures with magnetic field, accounting for the denoising approach adopted, exclusively on MK and KFA.

Indeed, MK is by far the most widely investigated DKI measure in preclinical and clinical studies, having the more throughout biophysical interpretation and standing for microstructural tissue complexity (Jensen et al., 2005). In addition, this metric proved to be highly sensitive to susceptibility-induced background gradients that would at least partially explain the field-dependent variability of diffusion measures (Palombo et al., 2015).

As regards AK and RK, according to reference studies about DKI method, they are strictly dependent on MK in their definition (Jensen and Helpern, 2010). We thus opted, given the observational and preliminary nature of this work, to set them apart for now. In contrast, for its own mathematical formulation, KFA is independent from MK (Hansen and Jespersen, 2016). Moreover, unlike other DKI measures, KFA was found to have the largest relative discrepancy between 1.5 and 3T in (Shaw et al., 2017).

Violin plots displaying underlying distribution of averaged MK and KFA across subjects, in both WM and GM ROIs at both field strengths and after application of the two denoising methods, are reported in Figure 6.6 and 6.7, respectively, with strip plots as a complement to show all observations. We inspected both simple main effects analysis and Bonferroni post-hoc testing to specifically assess pairwise differences between the two factors' levels in all examined ROIs.

For the sake of completeness, variation of remaining DKI-related measures relative to field intensity and denoising is displayed in Supplementary Figures B.1 and B.2 in Appendix B.

From this analysis, as regards MK, we can notice denoising does influence variability with magnetic field strength in CC, SCP, PUT, TH and PAL. Indeed, MK values in these ROIs do not significantly change in absence of denoising: significant variations arise when introducing both denoising methods for CC, PUT, TH and PAL; just Patch2Self for SCP.
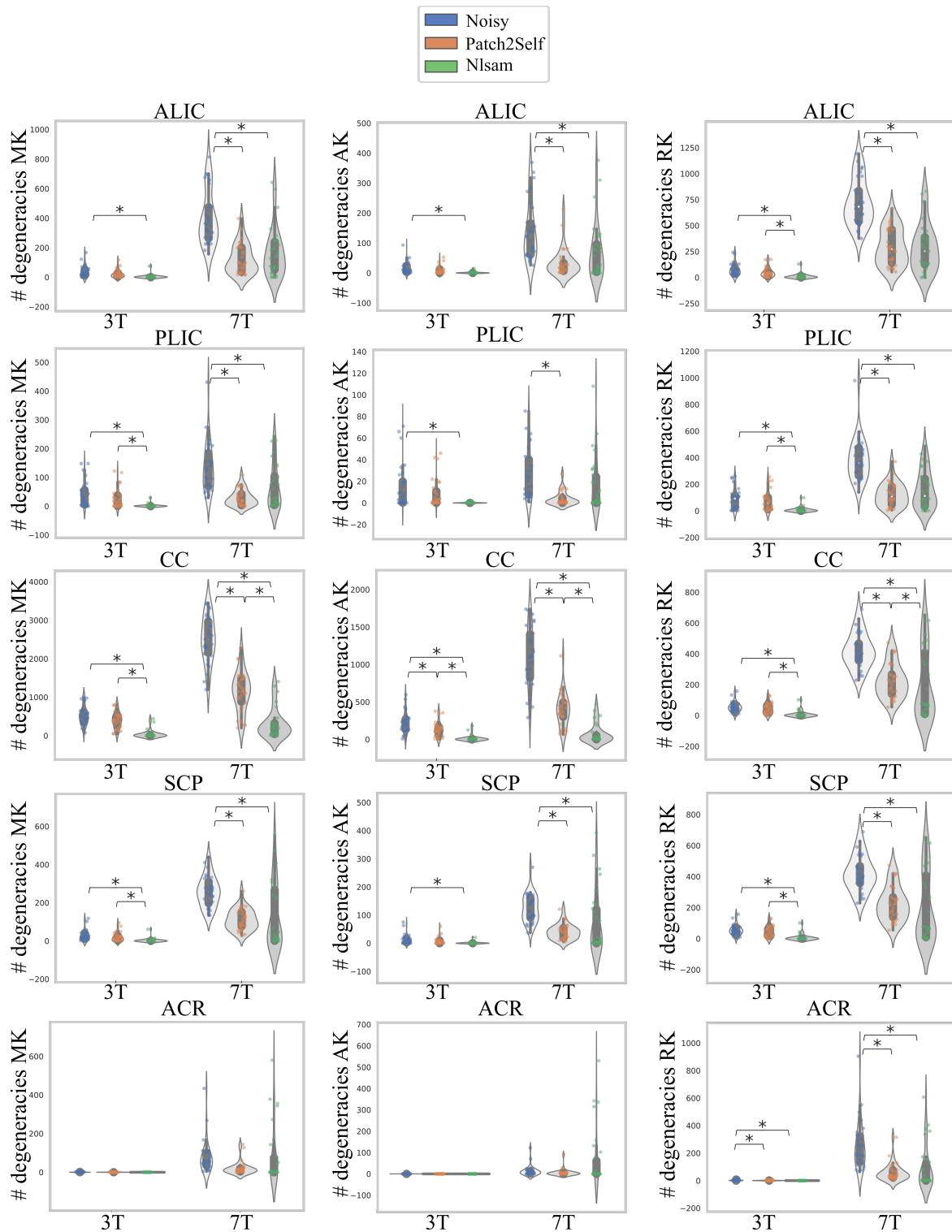
Figure 6.5 **Number of implausible voxels for Mean Kurtosis (MK), Axial Kurtosis (AK), Radial Kurtosis (RK) in WM areas**: Anterior Limb of Internal Capsule (ALIC), Posterior Limb of Internal Capsule (PLIC), Corpus Callosum (CC), Superior Cerebellar Peduncle (SCP) and Anterior Corona Radiata (ACR). $*$ indicates $p \leq 0.005$ ($\frac{\alpha}{n}$, with $n = 10$) in one-way ANOVA with Bonferroni correction.

Regarding variations of MK metric with respect to denoising approach, we can observe higher differences at UHF. Indeed, significant differences in denoising at 3T were detected just for PLIC and CC. As for KFA, this metric does not seem to depend on denoising in its variation from 3T to 7T. Indeed, significant differences in KFA values exhibit whether applying both denoising methods or not. Patch2Self method even seems to flatten any difference between the two fields in ALIC, TH and PAL. This time variations of KFA metric related to the denoising method adopted indifferently interest both 3T and 7T.
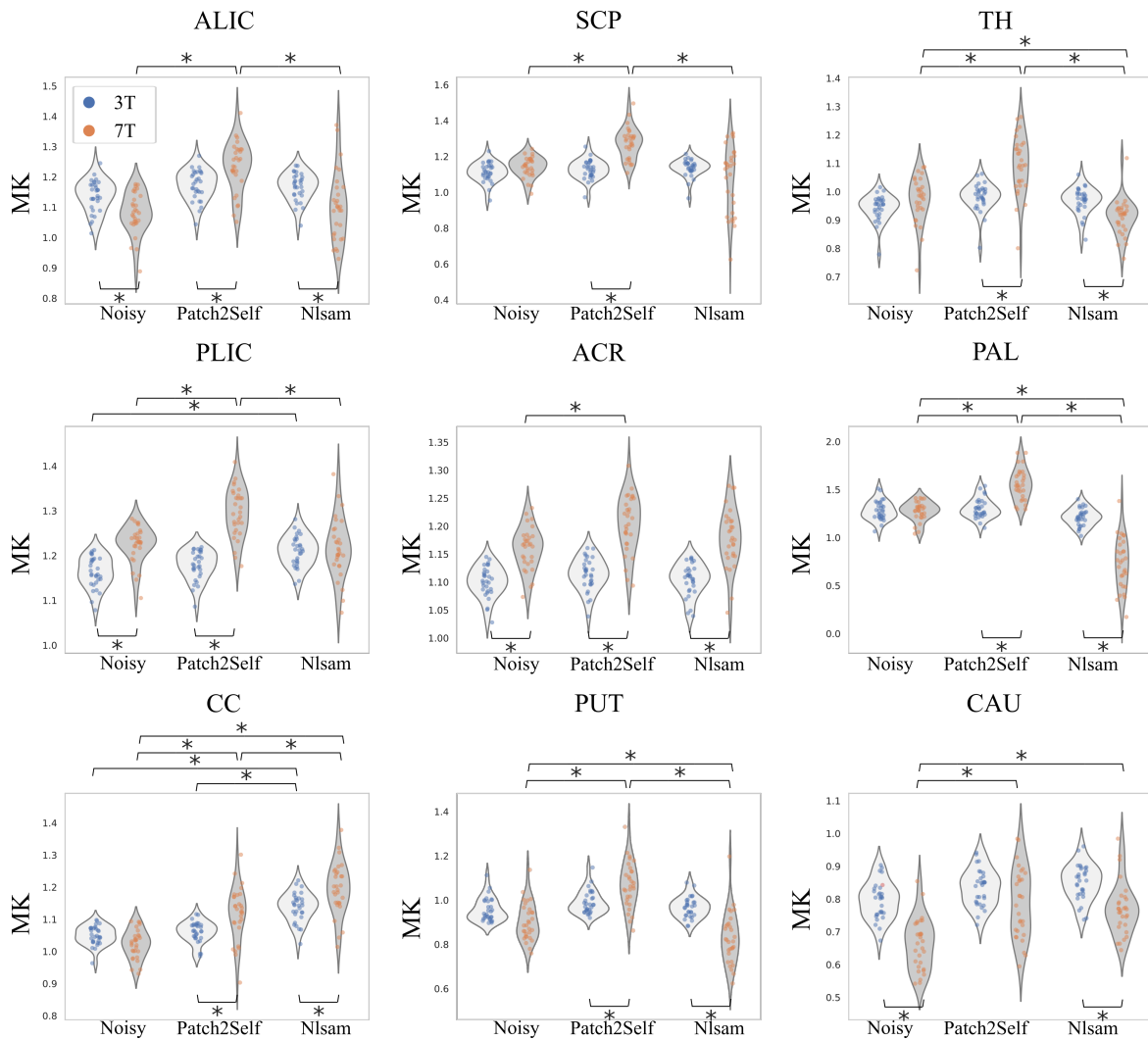
Figure 6.6 **Violin plots of average MK over WM and GM ROIs at each field strength and denoising approach** with overlaid strip plots as a complement to show all observations along with representation of the underlying distribution. In two-way ANOVA with Bonferroni correction, upper * indicates $p \leq 0.0056$, ($\frac{\alpha}{n}$, with $n = 9$) considering differences in the denoising approach at fixed magnetic field. Conversely, lower * indicates $p \leq 0.0056$, ($\frac{\alpha}{n}$, with $n = 9$) considering differences in the magnetic field within the same denoising method.
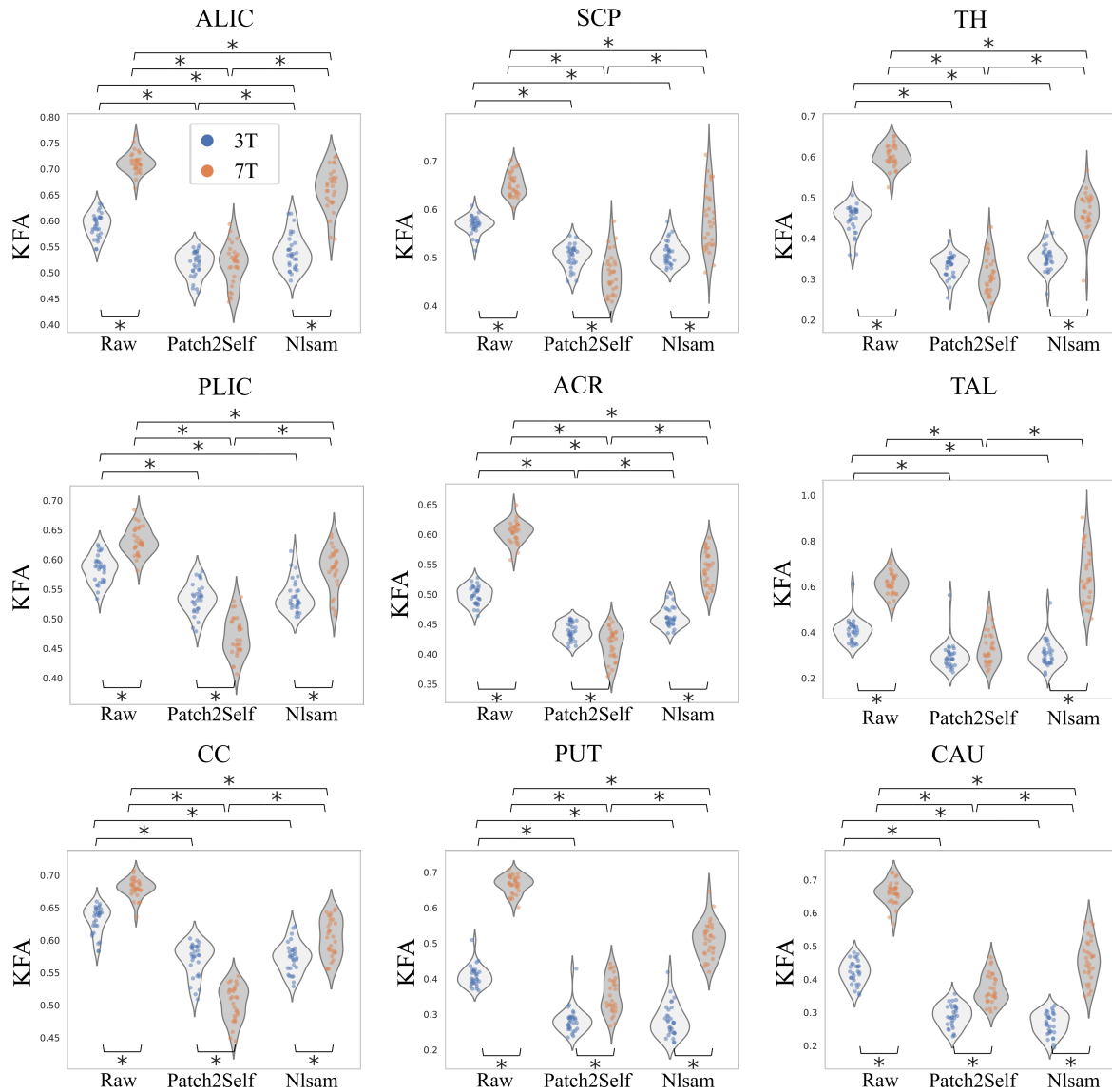
Figure 6.7 **Violin plots of average KFA over WM and GM ROIs at each field strength and denoising approach** with overlaid strip plots as a complement to show all observations along with representation of the underlying distribution. In two-way ANOVA with Bonferroni correction, upper $*$ indicates $p \leq 0.0056$, ($\frac{\alpha}{n}$, with $n = 9$) considering differences in the denoising approach at fixed magnetic field. Conversely, lower $*$ indicates $p \leq 0.0056$, ($\frac{\alpha}{n}$, with $n = 9$) considering differences in the magnetic field within the same denoising method.

Part III

Feasibility of advanced Diffusion Imaging in neonatal clinical data

Chapter 7

Diffusion Kurtosis Imaging of Neonatal Spinal Cord in clinical routine

7.1 Background

In light of the findings from Chapter 6, we opted for adopting Patch2Self as the denoising method of choice when translating to neonatal imaging. The first target of our investigations was SC region. Intrigued by results of application of HARDI methods to adults as well as children, we aimed at exploiting their advantages also in the neonatal setting, attempting to enable their inclusion within real clinical scenarios and focusing specifically on the DKI model.

Within existing non-standard techniques, DKI has indeed turned out to be especially suitable for imaging of SC, a structure where the assumption of Gaussian diffusion fails (Cohen et al., 2017). Indeed, GM in the central portion of SC contains cell membranes and organelles that limit diffusion to fewer directions. Taking into account pathological processes not following a Gaussian distribution, DKI provides a better understanding of the underlying micromolecular environment. In fact, it exhibits increased sensitivity in microstructural assessment of both WM and GM (Wu and Cheung, 2010). Hence this susceptibility translates into an increased amount of diagnostic information, beyond that obtained with routine diffusion metrics, as proven both for adult brain (Jensen et al., 2005; Wu and Cheung, 2010) and spine (Raz et al., 2013), (Hori et al., 2012).

Latest technological advances on reduced FOV techniques to mitigate susceptibility artifacts and cardiac/respiratory gating have allowed to overcome most of the methodological challenges inherent to adult SC imaging (Taber et al., 1998). Thanks to these strategies, DKI by now represents a promising tool for studying a plethora of spine disorders with minor

modifications to protocol parameters in use for brain imaging (Raz et al., 2013), (Bester et al., 2010; Li and Wang, 2017; Panara et al., 2017).

As anticipated in Chapter 3, the scenario becomes definitely more complicated when attempting to translate this imaging technique to the neonatal clinical setting for a multiplicity of factors related to the age range under analysis (Sorantin et al., 2008). On the one hand, artifact-reducing techniques (i.e. cardiac gating, respiratory compensation, and suppression sequences) (Wilm et al., 2007) are often unfeasible since time-consuming, and sedation is typically not desirable. On the other hand, optimized acquisition sequences (Andre and Bammer, 2010), often combined with state-of-the-art techniques such as parallel-imaging and MB, ideal for increasing acquisition speed and thus enabling HARDI, are not always available in a general hospital due to high costs and technical limitations.
All aforementioned issues result in artifact-laden, low-signal images, which are often sub-optimal for diagnostic evaluation.These complications have made HARDI techniques fairly unutilized for investigation neonatal SC domain.

If extension of DTI to the pediatric SC has shown promising results in a wide range of clinical conditions, as evidenced by the increasing number of works on the topic (see Chapter 4), what immediately stands out while reviewing literature on pediatric SC is the absence of studies concerning DKI and particularly applied to the neonatal period (0-1 month).

To the best of our knowledge, the only published work on pediatric DKI (Conklin et al., 2016) is limited to grown-up children (6-16 years), whose larger anatomical structures and reduced source of movements enable better image quality and longer scan times. Indeed, in newborns, SC dimensions themselves - 24 cm average length and 4.4 mm diameter, possibly further diminishing in case of distortions (Singh et al., 2021) - are sufficient to conceive amplification of previously mentioned technical issues and thus legitimize the lack of research towards this direction.

However, the ability of DKI to offer additional and complementary information to DTI may bring a significant contribution in investigating such decisive and delicate stage of development, especially if we consider the wide range of developmental anomalies of the spinal canal affecting infants at birth (Rufener et al., 2011).

It is on this premise that we conceived our work, whose aim is to show the feasibility of applying DKI to neonatal SC within clinical routine, opting for minimal modifications of current clinical setup. We thus introduce here the first complete pipeline specifically adapted to neonatal imaging acquired for diagnostic purposes. Applicability and clinical validity of proposed method has been evaluated analyzing a specific clinical case-study concerning a condition common to preterm birth, in collaboration with Neuroradiology Unit of Giannina

Gaslini Children's Hospital of Genova.

Specifically, we assessed effects of WM brain lesions typical of PWMI on below cervical SC tracts by comparing diffusion measures between pathological patients and healthy controls. Our findings, though preliminary, confirm the ability of DKI model in capturing subtle pathological alterations. Conversely, DKI-related measures appear to be less sensitive to WM/GM tissue differentiation at this stage.

Since there are currently neither available protocols nor standardized methodological pipelines for performing DKI in the infant SC, this methodological outline may at least serve as a proof-of-concept, stressing the need for infant-specific data acquisition and processing guidelines in order to translate DKI of neonatal SC into routine clinical practice.

7.2 Matherials and Methods

7.2.1 Subjects

Infants whose data have been used to disclose each step of the pipeline have been enrolled since August 2019 and scanned with 3.0 T MR scanner using a 32-channel head array coil (Ingenia Cx, Philips, Best, the Netherlands) at the Neuroradiology Unit of Giannina Gaslini Children's Hospital of Genova. Conventional MRI and DKI were performed in 17 pre-term infants (28.1 to 36.7 weeks Gestational Age (GA); scanned at TEA). Diagnosis has been exclusively made based on MRI findings reported by experienced neuroradiologists. Details about subjects' demographics are reported in Table 7.1.

This single-center study was carried out in accordance with the recommendations of "Comitato Etico Regione Liguria, Genova, Italy" with written informed parental consent obtained for each infant prior to examination in accordance with the Declaration of Helsinki. Subjects were spontaneously breathing during examination; free-flowing oxygen was administered for all the duration of MRI session if necessary. Throughout the course of the examination, newborns were subjected to constant monitoring of the oxygen saturation and heart rate, by pulse oximeter and three-electrode electrocardiographic monitoring, respectively. In consensus with a board-certified pediatric neuroradiologist, we performed Quality Control (QC) for each of the pipeline's steps.

7.2.2 Full Pipeline Description

Our pipeline integrates MRtrix3 v.3.0.1 (Tournier et al., 2019) for setting of dMRI acquisition sequence, Spinal Cord Toolbox (SCT, v. 5.3.0, https://github.com/neuropoly/

Table 7.1 Demographics features of infants-spinal cord

	Unhealthy (n=9)	Healthy (n=8)
Gender (M/F)	6/3	4/4
Mean GA (range; week)	30.3±2.6 (28.1-35.0)	31.8±3.1 (28.3-36.7)
Mean PNA (range; week)	9.2±3.9 (0.1-11.7)	8.6±3.6 (2.0-10.7)
Mean PMA (range; week)	39.4±1.6 (35.1-40.6)	40.4±1.3 (38.7-42.4)

*M/F = number of male and female infants; GA = gestational age;
PNA= postnatal age; PMA = postmenstrual age.

spinalcordtoolbox) (De Leener et al., 2017a) for all processing steps specific to the SC, and DIPY v.1.4.1 (Garyfallidis et al., 2014) for denoising as well as computation of diffusion metrics.

Output of key processes, such as motion correction, segmentation and registration with atlas, can be checked through an interactive SCT QC module, which automatically generates reports consisting in HTML files, containing a table of entries and allowing to show, for each entry, animated images (background with overlay on and off) for data quality validation. In our methodological pipeline we have opted for mainly relying on SCT, being currently the only existing fully-comprehensive, free and open-source software dedicated to the processing and analysis of multi-parametric MRI of the spinal cord successfully employed in a plethora of clinical applications concerning adult SC.

An overview of our image processing pipeline highlighting key features is shown in Figure 7.1. Since SCT algorithms are validated in adult imaging, we specifically customized each processing step to our neonatal scans. Our pipeline thus represents, to the best of our knowledge, the first semi-automated ad-hoc procedure for imaging of neonatal spine. A fully automatic workflow is not feasible here: acquisition time constraints, available scanner features, and subsequent image quality require inevitable although minimal and highly reproducible manual interventions.

7.2.3 Customized Acquisition Setting

In order to minimize macroscopic movement artifacts, all recommended guidelines for pediatric imaging have been adopted. So as to protect infants from acoustic disturbances caused by MR sequences, we resorted to baby earmuffs and silicone paste for hearing aids. Furthermore, we avoided most of the motion by swaddling infants and by placing airbags around the baby's head. In addition, protective pads have been placed between the magnet
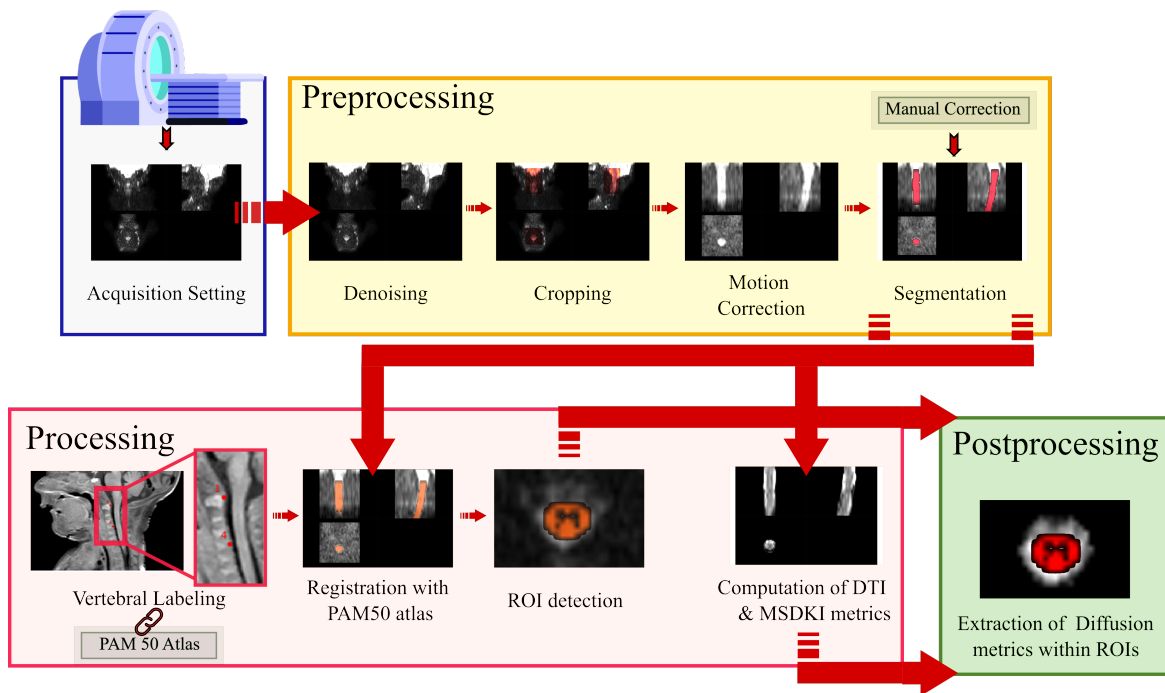
Figure 7.1 **Overall Processing Pipeline:** designed pipeline allows complete handling of DKI scan of neonatal Spinal Cord from acquisition setup to preprocessing, processing and postprocessing

and the patient. All these contribute to create a comfortable and warm rest environment, minimizing the chance of free movements.

MRI was performed when possible during spontaneous sleep by exploiting the administration of breast milk or formula about 30 minutes before the start of the exam. In case of spontaneous sleep failure, in order to minimize macroscopic movement artifacts, the instrumental examination was performed under mild sedation by orally administering Midazolam at 0.1-0.2 mg/kg diluted in glucose solution 33%, subject to signature of informed consent from parents and applied by expert trained nurses.

Given the lack of a specific acquisition protocol for DKI of neonatal SC, we designed the diffusion-weighting scheme in collaboration with the neuroradiologists at Giannina Gaslini Hospital. One constraint we had to deal with was the impossibility to perform optimized variants of SE-EPI sequence (i.e. reduced FOV or spatially selective techniques) on Philips Ingenia scanner. Therefore, minimization of scan duration was our main focus in order to suppress motion and fast CSF pulsation artifacts typical of newborns.

We thus tested different versions of diffusion-weighted gradient scheme, adopting optimal trade-off between fODFs profile (estimated with Mrtrix3 using Multi-Shell Multi-Tissue

CSD (MSMT CSD)), image quality and scan time. We generated each multi-shell diffusion gradient table through Mrtrix3 script `gen_scheme`, taking as inputs the number of phase-encoding directions to be included in the scheme (for most scanners, including ours, typically 1), the *b* value of the shell, and the number of directions to include in the shell. This procedure ensures uniform spherical sampling by maximizing uniformity within shells using a bipolar electrostatic repulsion model for optimal angular coverage.

Regarding the choice of acquisition parameters, we borrowed some crucial measures (*b* values, voxel size, as well as TR/TE) from the setting in use in the corresponding adult study we referred as a starting point (Panara et al., 2019). Indeed, this group presented a scenario closely similar to ours - Philips 3T scanner and SE-EPI sequence without advanced variants - and managed to perform DKI in adult subjects within clinically feasible time, e.g. 6 minutes.

For further reducing acquisition time without significantly affecting image quality, we applied the MB slice acceleration technique (https://www.usa.philips.com/healthcare/resources/landing/compressed-sensecombined) (Barth et al., 2016) . The final version of diffusion acquisition scheme is displayed in Figure 7.2 as well as reported in Table 7.2, and includes 6 $b = 0$; 13 $b = 700$ and 13 $b = 2100$ s/mm^2 for a duration of 4 minutes 30 seconds. This allowed acquisition of high in-plane resolution axial diffusion weighted images, where $b = 0$ scans could be well discriminated from non $b = 0$ volumes and anatomical SC features are sharp.

A valuable alternative to this reduced DKI scheme is represented by Fast Kurtosis Imaging (Hansen and Jespersen, 2017). This recently developed technique may give a relevant boost to widespread, routine clinical applicability of DKI in the infant SC by drastically reducing acquisition as well as post-processing time. A significant increase in speed is indeed made possible by a reduction in data demand achieved through rigorous analysis of the relation between the DKI signal and the kurtosis tensor-based metrics. It therefore computes a Mean of the Kurtosis Tensor (MKT) from at least 13 diffusion-weighted images - the so called "1-3-9 approach". Commonly, this basic scheme is extended to 19 diffusion-weighted images - the so called "1-9-9 approach"- for robust and reliable parameter estimation with the chance to reconstruct some parameters even in real time, which may be really valuable in the clinic. This technique has been successfully validated both in human brain (Næss-Schmidt et al., 2017; Tietze et al., 2015) and SC (Thaler et al., 2021) demonstrating to offer the same information as the conventional DKI both in normal and diseased tissue.

Moreover, under the assumption of axisymmetry inherent to regions with a well-defined axis of symmetry such as large peripheral nerves and SC (Hansen et al., 2016), this method can also be easily integrated with White Matter Tract Integrity (WMTI). This valuable
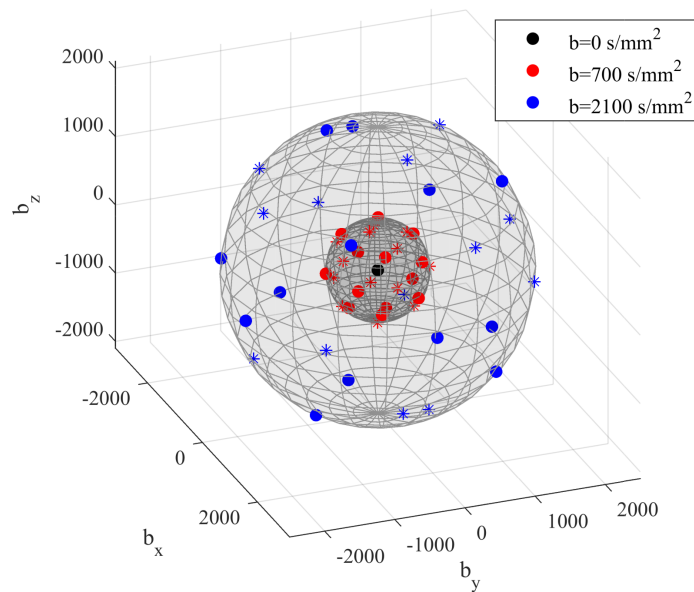
Figure 7.2 **3D view of final diffusion acquisition scheme:** directions of diffusion-sensitizing gradients relative to each *b* value are displayed in three different colors as reported in the legend. Units are in s/mm^2. Markers indicates polarity: dots are the polarities in the set, asterisks their opposite

modeling-based WM characterization (Fieremans et al., 2011) provides detailed information about microstructure of highly aligned fiber bundles and could thus be particularly suitable for investigating SC.

Both "1-3-9" and "1-9-9" methods are heavily sensitive to deviations from the encoding scheme required to ensure data reduction. These schemes consist in acquiring images at fixed *b* values (0,1000 and 2500) along a precise set of directions specified in (Hansen et al., 2013). This is thus about conventional diffusion sequences easily implemented on almost any clinical system by allowing inclusion of DKI, at little additional cost, as a component of any protocol for imaging of the brain or other organs. However, our starting acquisition scheme did not match the required diffusion sensitizing directions and exactly for this reason we were not able to apply this method retrospectively. Nonetheless, a strength of current methodological pipeline is its independence from the dMRI acquisition scheme used to acquire input raw data and it could thus be successfully used to perform fast DKI, too.

Along with dMRI, we also acquired a high-resolution structural image as anatomical reference. The definitive MRI protocol thus consisted in a Turbo Spin Echo (TSE) 3D T1-weighted image followed by a DKI series whose details are listed in Table 7.2.

Table 7.2 Data Acquisition Details for both structural 3D T1w and DKI image

	3dT1	**DKI**
TR/TE (s)	0.6/0.026337	3.378/0.128
Diffusion Scheme (s/mm²)	–	6 b=0, 13 b=700, 13 b=2100
Flip Angle (°)	90	90
Field of View (FOV) (mm)	195x195x126	128x93x96
in-plane Acquisition Resolution (mm)	1*1	1*1
Acquisition Matrix	195*195	128*93
Reconstruction Resolution (mm)	0.38*0.38	0.8*0.8
Reconstruction Matrix	512*512	160*160
Multi-Band Factor	–	2
# Averages	2	1
Slice Thickness (mm)	0.5 without gap	4, without gap
Slice Orientation	sagittal	axial
# Slices	251	24
Total Scan Time	4 minutes 5 s	4 minutes 30 s
Partial Fourier factor	–	0.6

7.2.4   Preprocessing

Denoising

SC imaging is characterized by low SNR, which can hamper accurate, repeatable, quantitative measurements. Moreover, models such as DKI are susceptible to noise and signal fluctuations often leading to degeneracies in estimation of derived parameters. SNR further lowers in case of neonates, due to relatively high overall free water content, and denoising approaches based on PCA are inapplicable due to a reduced number of diffusion gradient directions. Therefore, considering also the main findings from Chapter 6, we chose Patch2Self to perform the crucial denosing step within our pipeline. This denoiser has already showed a significant improvement in repeatability and conspicuity of pathology in diffusion volumes and quantitative DTI metrics for adult SC (Schilling et al., 2021). Here, we opted for applying Patch2Self as first preprocessing step on raw data since it showed to offer highest SNR. The method is implemented in Dipy v.1.4.0 and applied with OLS regressor, since recommended for SC imaging (Figure 7.3).

Cropping

SC scans usually include also cerebral areas such as medulla and cerebellum due to their proximity with cervical SC. In order to exclusively focus on the area of interest excluding
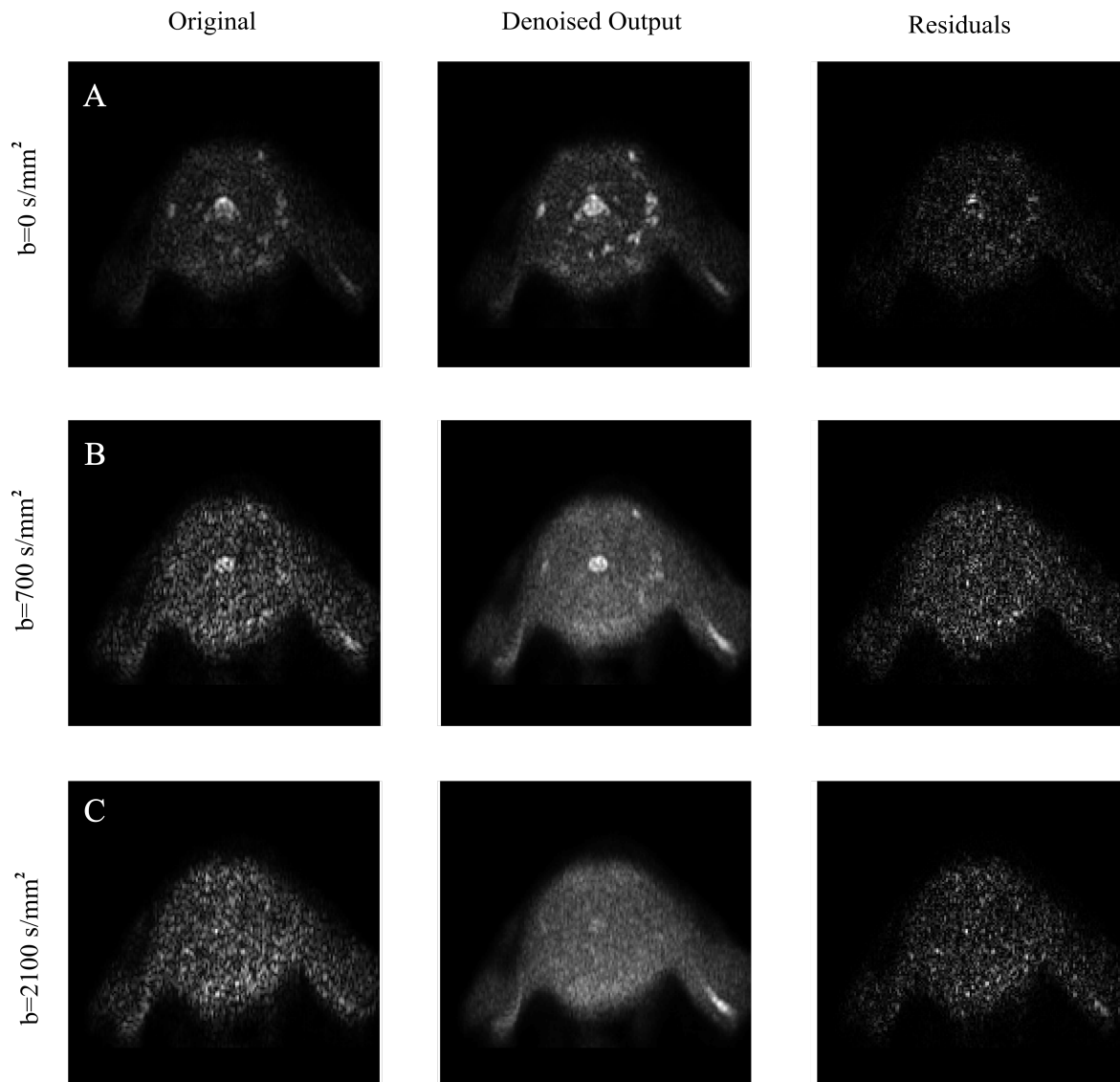
Figure 7.3 **Visual inspection of denoising:** The denoising of Patch2Self is compared against the original noisy image along with their corresponding residuals for each **(A)** b=0, **(B)** b=700 and **(C)** b=2100 s/mm^2 shells, respectively. Notice that Patch2Self does not show any anatomical structure in the corresponding residual plots likely neither introducing structural artifacts

undesired voxels, as a first preprocessing step, we thus recommend applying to DKI images
SCT function `sct_crop_image` allowing also to fasten subsequent processing. Lower and
higher bounds for cropping along the three spatial coordinates can be specified via command
line in order to select the same area of interest (i.e., cSC) for all the cohort, considering FOV
positioning is consistent across subjects. Specifically, in the case of our scans, FOV reduction
allowed to exclude upper non-spinal areas (i.e., cerebellum) as well as lower spinal levels
whose corresponding slices are not usable due to poor image quality (Figure 7.4a).
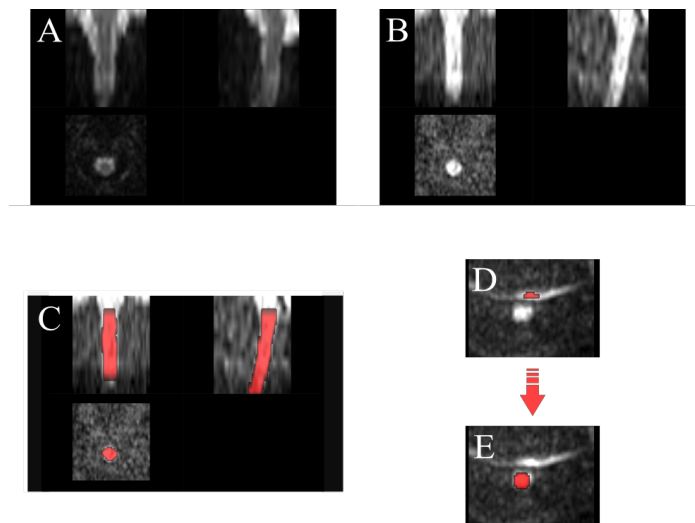
Figure 7.4 **Preprocessing:** DKI scan through preprocessing steps for one example subject:
(A) FOV reduction; **(B)** Motion Correction; **(C)** Segmentation: Deep Learning Segmentation
algorithm generally achieves satisfactory results in SC detection; **(D)** Example of artefactual
slice due to a poor fat saturation, causing the fat to alias on the spinal cord area and **(E)**
requiring manual correction of segmentation

Motion Correction

Subjects' immobilization and anesthesia successfully minimized motion in our acquisitions.
However, since dMRI data are analyzed at a voxel level, residual intrascan and/or interslice
motion can adversely affect accuracy of the modeled results. We thus resorted to SCT
complex motion correction framework `sct_dmri_moco`, based on a combination of tools.
First of all, *SliceReg* algorithm estimates slice-by-slice translations while ensuring regular-
ization constraints along z axis. The latter is achieved using a polynomial function (order
specified by the user, flag *-param*). This method was shown to offer better accuracy and
robustness than rigid-body transformations and non-regularized slice-by-slice registration,
respectively (De Leener et al., 2017a).

Moreover, motion correction in SCT includes another feature first proposed in (Xu et al., 2013) to improve the robustness of registration in high *b* value diffusion MRI data such as DKI datasets. It consists in grouping adjacent volumes and estimating the transformation relying on these successive subsets (typically from 3 to 5 volumes) averaged together (flag *-g*).

This robust slice- and group- wise motion correction works successfully also in case of neonatal scans, and it is hence applied here with default parameters: grouping of 3 successive dMRI volumes, regularization with 2nd order polynomial function, unitary smoothing kernel (1 mm), and final spline interpolation (flag *-x*), except for the metric used for registration (Figure 7.4b). Indeed, Cross Correlation (CC) has been selected as similarity metric given its better performance with respect to Mean Squares or Mutual Information (default option) at the expense of computational time. Since `sct_dmri_moco` works through iterative average over groups of successive slices in order to increase the SNR of the target image, its output includes a 3D volume corresponding to the mean from DKI slices. These motion corrected average DKI data will serve as input for subsequent segmentation thanks to its excellent cord contrast.

Thanks to the limited duration of our acquisition and to adopted procedures for minimizing movement throughout the exam, amount of motion is very limited in our images. As a result, outcome of motion correction step does not significantly differ from raw DKI image by visual assessment. However, this represents a crucial step in case of longer scans more prone to source of motion artefacts.

Segmentation

Proper segmentation of SC is decisive for subsequent steps of template registration and computation of metrics along the cord. Detection of SC has turned out to be a critical step, since standard SCT algorithm `sct_propseg`, based on multi-resolution propagation of tubular deformable models (De Leener et al., 2014), is trained for adult spine. Given the reduced size of neonatal SC and the low contrast between the spine and CSF, default segmentation method fails in several slices even after modulating the algorithm parameters - e.g., manual initialization of spinal cord centerline through interactive viewer (flag *-init-mask*), selection of SC radius size (flag *-radius*) or cord rescale (flag *-rescale*).

We thus resorted to a more recent and advanced method of SC extraction, based on deep learning `sct_deepseg_sc` (Gros et al., 2019). This fully automatic segmentation framework was conceived for detecting SC and intramedullary MS lesions from a variety of MRI contrasts and resolutions. It is composed of a cascade of two convolutional neural networks

(CNN), specifically designed to deal with spinal cord morphometry: the first detects the cord centerline and reduces the space around the SC (for better class balance), and the second segments the cord. Segmentation results outperformed `sct_propseg`, showing higher robustness to variability in both image parameters and clinical conditions.

Thanks to its versatility, the application of this method results suitable also for neonatal imaging, allowing robust and accurate segmentation of our scans without ever the need of additional parameters but just specifying the kind of image contrast as dwi (flag *-c*) (Figure 7.4c). In case of failure of SC detection, we necessarily opted for manual correction of problematic slices on FSL editor (FSLeyes) (Figure 7.4d,e).

This is the case of five subjects within our cohort: to validate the quality of segmentation, we checked the QC feature on our MRI images across subjects and noticed some local segmentation leakage - related to the onset of artifacts at acquisition phase and not to a flaw with the algorithm - in a few slices and hence corrected it manually.

7.2.5   Processing

Vertebral Labeling

After segmentation, labeling of vertebral levels or discs is the second mandatory step in order to match the template to the subject's MRI (template registration). Two vertebral levels are necessary for registering data to the template. Each of these two landmarks consists of a voxel placed in the middle of the SC, at the level of the corresponding mid-vertebral body, and assigned a relative number starting from 1 for C1 vertebra. However, SCT recently introduced the possibility to alternatively use inter-vertebral disc labels with the analogous procedure of reference numbered voxels.

We performed this step on 3D T1w images in order to achieve better accuracy given their higher overall quality and contrast compared to DKI ones, where vertebral discs are not clearly identifiable.

Labeling from 3D T1w anatomical image is possible as it turned out to match relatively well along the superior-inferior (z) axis, the target direction of disc labeling, with the DKI scan - not along the Anterior-Posterior (AP) or Right-Left (RL) direction, Figure 7.5. Vertebral labeling is typically done using an automatic method `sct_label_vertebrae`, which finds C2-C3 disc, and then locates neighbouring discs using similarity measure with the PAM50 template at each specific level (Ullmann et al., 2014). Default SCT procedure `sct_label_vertebrae` fails in automatically detecting C2-C3 vertebral disc once again because of the small size of spines at issue and low image contrast compared to adults.

Therefore, we manually created labels with the command `sct_label_utils` through inter-active viewer option provided by SCT (flag *-create-viewer*) with little to no waste of time. Specifically, vertebral labeling was created at the posterior tip of the top of C1 vertebra and at C3-C4 disc, centered in the cord. Manual intervention only took a few seconds per subject (Figure B.5).
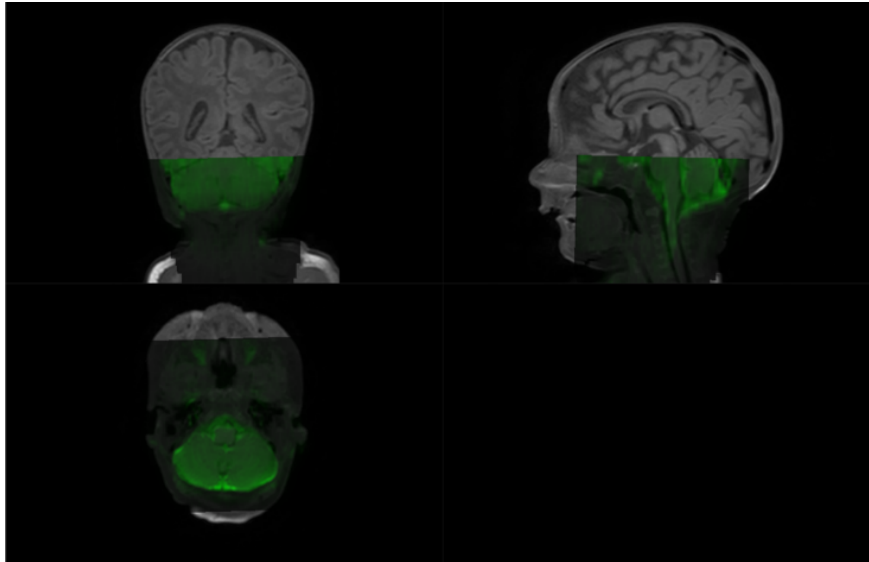
Figure 7.5 **DKI scan overlaid on structural 3dT1w image:** while both images are clearly not registered along the antero-posterior direction due to the very strong susceptibility artefact, the z-location is similar: see how the bottom tip of the cerebellum is consistent for the two scans

Registration to PAM50 Atlas

Registration between subject's diffusion and atlas space is a very demanding task in case of neonatal imaging given the lack of a specific pediatric atlas compatible with SCT (one is currently under creation, https://github.com/neuropoly/spinalcordtoolbox/issues/2530). We thus used PAM50 atlas (De Leener et al., 2018), an adult template for MRI of the full SC and brainstem in the same coordinate system as the ICBM152 (MNI) brain template, allowing to conduct simultaneous brain/spine studies. It consists of a T_1w, T_2w, T_2^*w, WM and GM probabilistic atlas and WM atlas of tracts as well as probabilistic labeling of spinal levels. The template has been constructed from straightened SC for facilitating registration and visualization of results.

`sct_register_to_template` is the main command for registering one subject to the template and vice versa, since it outputs the forward and backward warping fields. We chose

subject's native diffusion space as target of registration transforms as the straightening required by opposite strategy would cause through-plane interpolation errors which would bias following extraction of diffusion measures (De Leener et al., 2017b).

Moreover, we suggest employing T_1w atlas image for its better contrast similarity with DKI scan compared to T_2w.

Application of default command did not produce satisfactory results, stressing the need to tweak all the input parameters to deal with our particular contrast and resolution. Given the presence of artifacts and some inherent features (e.g., low CSF/cord contrast) that could compromise the registration, we used SC segmentation as input for the algorithm to ensure maximum robustness.

Registration was then built through multiple steps by increasing the complexity of the transformation performed in each step (starting with large deformation with low degree of freedom and finishing with local adjustment). Specifically, the first step consists in vertebral alignment, that is vertebral level matching between the subject and the template based on posterior edge of the intervertebral discs provided by previous manual vertebral labeling. Second step is slice-wise center of mass alignment between the two images, using *centermass* algorithm instead of default *centermassrot* (which also includes rotation alignment) because the cord is quasi-circular and cord angle estimation is not reliable here. The third step is R-L scaling along x axis followed by A-P alignment to match segmentation borders along y axis, with the ultimate aim of accommodating the very small SC size. Finally, iterative slice-wise non-linear registration is performed through non-linear symmetric normalization regularized with b-splines (Tustison et al., 2013) using information from comparison of Cross Correlation metric (CC) between the two images, which allows refinement of SC shape. Once the algorithm completed, one can assess the quality of registration through visual evaluation and inspection of QC module, and thus warp the template and all its objects to each subject's DKI image (Figure 7.6).

Current selection of parameters and steps successfully worked for our scans since atlas registration algorithm robustly achieved convergence, as verified through inspection of QC feature.

Computation of diffusion metrics

The end point of previous preprocessing and processing steps was computation of diffusion parametric maps, from which to extract quantitative summary measures requested by the particular study in question. We estimated diffusion parametric maps through DIPY software, as suggested in (Henriques et al., 2021a). To avoid unnecessary calculations on the back-
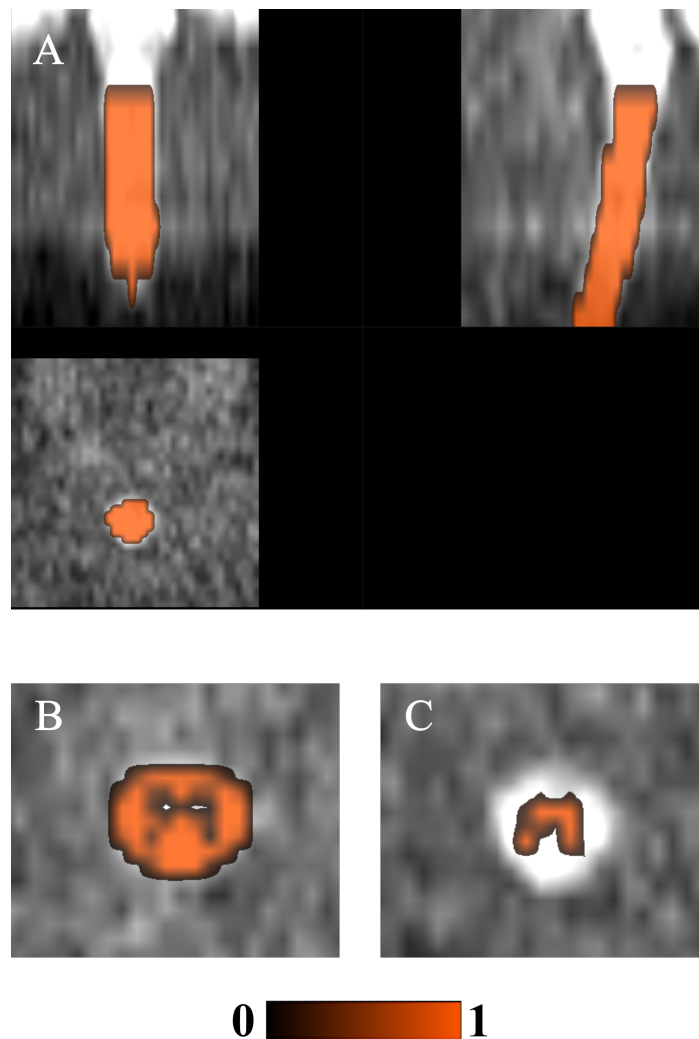
Figure 7.6 **Registration with PAM50 atlas and ROI detection through atlas-based approach**: **(A)** PAM50 atlas' cord segmentation binary mask, **(B)** WM and **(C)** GM probabilistic masks warped to subject's DKI motion-corrected mean image

ground of the image, we used a mask created by dilating spinal cord segmentation (through `sct_maths` command) because values outside the binary cord mask are important for proper account of PVE, having to be minimized in every possible way. Indeed, this phenomenon, because of the coarse resolution of MRI with respect to SC anatomy, may make the apparent value within a boundary voxel be a mixture between the WM and CSF compartment, thus yielding an inaccurate quantification of diffusion measures.

Since DKI model involves the estimation of a large number of parameters (Tax et al., 2015) and is more sensitive to artefacts (Henriques, 2012), we chose to further suppress the effects of noise and artefacts before diffusion kurtosis fitting using a 3D Gaussian smoothing (with a Gaussian kernel with fwhm=1.25) as suggested by pioneer DKI studies (Jensen et al., 2005). This also helps in addressing the issue of implausible negative values inherent to DKI fitting (Henriques et al., 2021b). The following parametric maps could thus be generated: MD, AD, RD, FA and MK, AK, RK, KFA, and MSK.

Given the low angular resolution data available, to ensure robustness and reproducibility of parameters' estimates, we opted for just computing DTI measures, whose reference tensor can be correctly estimated from at least six independent directions, and MSK. The latter is a robust scalar kurtosis index that can be estimated independently from acquisition scheme (Neto Henriques, 2018), (Henriques et al., 2015). Indeed, fitting MSDKI is well posed without relying on the full DK tensor, which would require a minimum of 15 non-collinear directions per b value. Moreover, this measure is generally more robust to low SNR situations as in case of neonatal imaging.

MSK can be seen as a proxy for the MK, showing to present nearly identical contrast while improving robustness and reproducibility of the kurtosis metrics, and results in parameter maps with enhanced quality and contrast. Specifically, this measure turns out to be less sensitive to thermal noise and imaging artifacts, and thus drastically reduces black voxels intrinsic to DKI and challenging the visual and statistical analysis of potentially clinically relevant biomarkers of tissue integrity. Moreover, as previously pointed (Henriques et al., 2015), standard kurtosis measures do not only depend on microstructural properties but also on mesoscopic properties such as fiber dispersion or the intersection angle of crossing fibers. In contrary, MSK has the advantage of being decoupled from confounding effects of tissue dispersion and crossing (Neto Henriques, 2018). Figure B.3 provides visualization of overall axial diffusion maps, including both DTI and MSDKI metrics, for an example subject.

Postprocessing

Thanks to this atlas-based analysis approach, it was possible to perform cord-specific quantification of diffusion metrics through `sct_extract_metric` command, also restricted to specific ROIs (labels used by default are taken from the PAM50 template, e.g. WM tracts, flag *-l*), vertebral levels (flag *-vert*) or slice (flag *-z*), according to the specific clinical needs concerned.

Along with WM and GM probabilistic masks as a whole, normally investigated in medical practice, one can carry out ROI detection also in specific tracts according to the clinical question (fifteen WM tracts and three GM regions available in total for each side). In our example, neither DKI nor structural images ensured sufficient WM-GM-CSF contrast to perform any manual detection of ROIs in contrast to high-contrast PSIR image of (Panara et al., 2019), whose acquisition time would be too long for neonates. Therefore, we exploited good registration outcome for automatic delineation of ROIs through atlas-based approach. We opted for using lateral Cortico-Spinal Tracts (CSTs) as ROIs for consistency with (Panara et al., 2019) - though grouping together left and right sides in order to gain robustness by increasing volume fraction as suggested in (De Leener et al., 2017a) - as well as WM and GM. We then computed the average of each diffusion measure (MD, AD, RD, FA and MSK) across C1-C4 vertebral levels, since outside of these levels the registration is inaccurate and/or MRI signal may be corrupted. We thus checked through QC module the correctly segmented slices corresponded to the same vertebral levels across subjects, starting from the first slice containing only SC (excluding cerebellum, Figure B.4c).

Moreover, estimation of DTI and MSDKI weighted average metrics was limited to those slices where SC segmentation is accurate: outside the segmentation mask, metrics would indeed be irrelevant. This was obtained by multiplying segmentation mask by specific WM, GM and CSTs atlas labels. We quantified diffusion metrics using Weighted Average (WA) estimation to minimize PVE avoiding bias into resulting metrics by the surrounding tissues (e.g., CSF). This is one of the recommended methods especially in case of noisy images and small tracts as in our case. We assessed associated voxel fraction to quantify the reliability of our diffusion measures: as demonstrated in (De Leener et al., 2017a), having at least 240 voxels results in an error smaller than 1%, while having 30 voxels results in an error inferior to 2%. In this example, the metrics were computed based on average 178.3, 50.5 and 31.5 voxels in WM, GM and CSTs respectively, thus assuring sufficient accuracy of estimates.

7.2.6 Case Study

PWMI is the most frequent type of brain lesion in preterm infants, and the spatial extent and location of WM injury correlate with distinct clinical outcomes, including cerebral palsy and motor impairment (Volpe et al., 2017). Given the strong association of WM injury with the motor function development of preterm neonates, we hypothesized that periventricular punctate WM lesions at TEA could be associated with regionally specific alterations in cSC microstructure.

A similar approach was already used by (Panara et al., 2019) to characterize cSC microstructural abnormalities in a cohort of adult patients with previous unilateral ischemic stroke in the vascular territory of the middle cerebral artery. DTI and DKI diffusion measures in cSC resulted to be a valuable imaging marker for predicting clinical outcome. In particular, significant reduction of FA and MK was observed in the affected lateral WM bundle of the cSC, correlating with the severity of motor dysfunction.

Accordingly, the ultimate goal of our study was to verify whether the presence of periventricular WM lesions affects the cSC tracts development. Specifically, we aimed to compare DTI and MSDKI measures of cSC in two groups of preterm neonates: (i) with punctate Periventricular White Matter lesions (PWMI), and (ii) with normal brain MRI (controls).

7.3 Results

7.3.1 Population size and classification

In order to investigate clinical differences among acquired subjects, we grouped infants as follows: (i) 9 subjects with punctate PWMI and (ii) 9 subjects with normal brain MRI, used as control group. At QC phase, in accordance with the expert neuroradiologist, we opted for excluding one control subject due to excessively poor image quality (e.g., signal leakage at C1-C3 level, Figure B.4a,b). Therefore, the final number of subjects under analysis amounted to 9 and 8 infants for the patient and the control groups, respectively.

7.3.2 The role of denoising

As mentioned above, neonatal imaging is inherently affected by low SNR and sensitive to imaging artifacts. Proper denoising of scans is therefore a crucial step in the processing pipeline. Above all, we thus focused on quantitatively assessing the contribution of Patch2Self denoiser on subsequent analysis. Firstly, we computed average SNR on $b = 0$, $b = 700$ and

$b = 2100$ s/mm^2 images for all subjects and across all slices belonging to C1-C4 area of our interest. For this task, we resorted to SCT function `sct_compute_snr`. The latter exploits methods described in (Dietrich et al., 2007).

Specifically, we have taken into account the spatially varying and parameter-dependent nature of noise distribution in case of parallel-imaging by choosing the so-called mult method. According to this definition, the noise of a single voxel is described by the stochastic variation of its signal intensity in repeated acquisitions. Since this approach has the weakest requirements on the statistical and spatial distribution of noise, it turns out to be valid also in case of increasingly complex MRI systems (e.g., multiple channels and complex reconstruction algorithms) and it is thus used as the standard of reference with which to compare the validity of other existing methods. In the absence of back-to-back scans with the same parameters (to use the default diff method), we looked at mult approach as the best option possible for our kind of input data.

We found an increase in mean SNR after applying Patch2Self at $b = 0$ s/mm^2 (5.88 ± 1.41 vs 14.64 ± 4.53), $b = 700$ s/mm^2 (3.12 ± 0.67 vs 16.47 ± 6.62), and $b = 2100$ s/mm^2 (1.95 ± 0.16 vs 12.31 ± 6.20). Hence, this evidence subsists not only for $b = 0$ images, agnostic from signal attenuation related to diffusion and thus exhibiting the highest SNR, but also for non $b = 0$ shells (Figure 7.7).
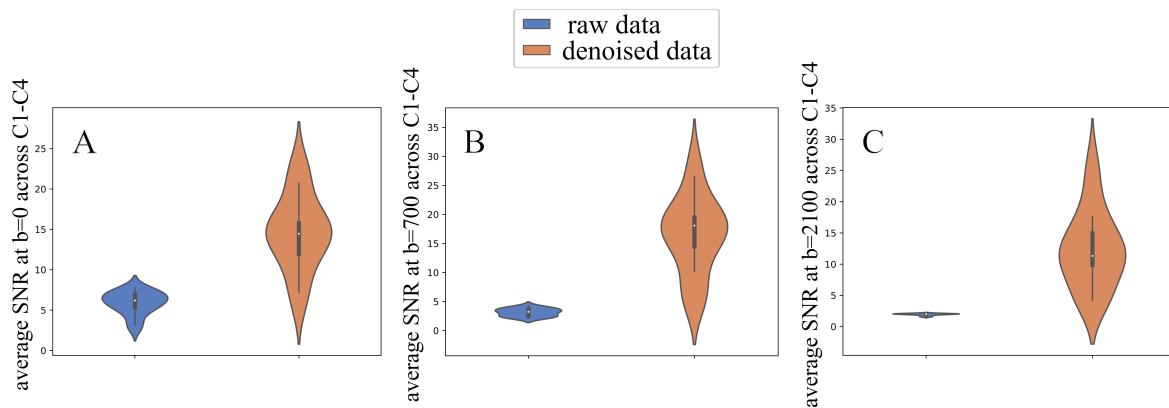
Figure 7.7 **Effects of Patch2Self denoising on noise at different diffusion weightings**. Average Signal-to-Noise Ratio (SNR) computed on **(A)** b=0 images , **(B)** b=700 and **(C)** b=2100 s/mm^2 increases in all the cohort, across C1-C4 vertebral levels under analysis, when including denoising with Patch2Self algorithm in the processing pipeline

We then inspected the impact of denoising on microstructure model fitting, a critical step often leading to degenerate parameter estimates due to the low SNR of dMRI acquisitions. Specifically, we applied DTI and MSDKI model on raw and denoised data, resorting both to traditional MP-PCA and to Patch2Self method. We opted for comparing our denoising

procedure with MP-PCA since it represents the current state-of-the-art unsupervised method for denoising DWI. MP-PCA exploits the redundancy in multidirectional dMRI data by identifying the noise-only principal components using the knowledge that the corresponding eigenvalues are described by the universal MP distribution, parameterized by the noise level. In order to compare the goodness of each fit, we performed a k-fold cross-validation (k=2) (see Chapter 6) across the whole volume of masked data for all the dataset at disposal. As standard measure for quantifying the goodness of fit in linear regression models, we computed the coefficient of determination R^2 as in Equation 6.1 of Chapter 6. In Figure 7.8, we depict the improvement of the R^2 metric by simply subtracting the R^2 scores of fitting undenoised data from Marchenko-Pastur and Patch2Self denoised data for both DTI and MSDKI models. We could observe a consistent trend across all subjects: R² shows a significant increase from MP-PCA to Patch2Self method for all the cohort in case of fitting MSDKI model, for all subjects except for one in case of DTI model (two-sided t-test with Bonferroni correction). Our observation suggests that Patch2Self proves to be particularly suitable for DKI model fitting.

7.3.3 MSK decreases in patients with PWMI lesions

To an initial evaluation based on the limited sample size available, we detected an increase in MD, AD, RD (Figure B.6), parallel to an overall decrease in FA and MSK (Figure 7.9) in preterm neonates with PWMI. This decrease was more pronounced in MSK than FA (Figure 7.9).

This visual trend of diffusion measures has been supported by a statistical survey, to be considered as preliminary given the very low sample size. We thus performed Scheirer Ray Hare Test, that is the non-parametric alternative of 2-way ANOVA, to assess the presence of statistically significant differences in DTI- and MSDKI- derived metrics between patient and control groups.

Specifically, we analyzed the effect of diagnosis (PWMI/control) and ROI (WM/GM/CSTs) on each diffusion measure (MSK, FA, MD, AD, RD). We showed that there is not a statistically significant interaction between the effects of diagnosis and ROI for any of the DTI and MSDKI measure (Table B.1). Similarly, simple main effects analysis showed that ROI does not significantly affect any diffusion parameter. Conversely, simple main effects analysis indicated a statistically significant effect of diagnosis exclusively on MSK, regardless of the ROI examined ($p = 0.0153$).

Then, we wanted to assess if MSK and FA means were significantly different between the

Figure 7.8 **Boxplots quantifying the increase in coefficient of determination metric after fitting downstream DTI and MSDKI models for the whole Spinal Cord volume across all subjects:** The R^2 improvements in each case are plotted by subtracting the scores of model fitting on undenoised data (noisy) from R^2 of fitting each denoised output. Note that the consistency of microstructure model fitting on Patch2Self (P2S) denoised data is higher than that obtained from Marchenko-Pastur (MPPCA), especially as regards MSDKI model. $ns : 5.00 \cdot e^{-2} < p \leq 1.00 \cdot e^0, * : 1.00 \cdot e^{-2} < p \leq 5.00 \cdot e^{-2}, ** : 1.00 \cdot e^{-3} < p \leq 1.00 \cdot e^{-2}, *** : 1.00 \cdot e^{-4} < p \leq 1.00 \cdot e^{-3}, **** : p \leq 1.00 \cdot e^{-4}$ in two-sided t-test with Bonferroni correction.

two groups in the different ROIs. We thus conducted a Mann-Whitney U test between each patient/control pair for each ROI (GM, WM, CSTs) separately for MSK and FA (Table B.2). Given the general low power of the statistical tests due to the limited number of subjects, we decided to quantify Common Language Effect Size (CLES) given its independence from sample size. Also in this case, we reported a non-significant ($p > 0.05$) difference of both MSK and FA values between the two groups in all ROIs. Nevertheless, we observed that MSK in CSTs exhibits the combined lowest p value ($p = 0.067$, uncorrected) and the highest effect size (0.77), corroborating the observed decrease of MSK in the patient group with respect to the controls (Figure 7.9).
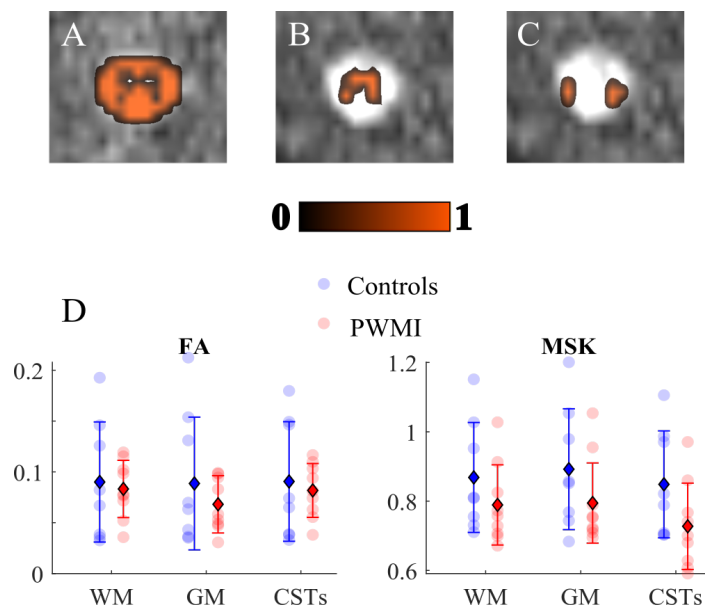
Figure 7.9 **MSK decreases in neonatal Periventricular White Matter Injuries**: **(A)** White Matter (WM), **(B)** Gray Matter (GM) and **(C)** Cortico-Spinal Tracts (CSTs) ROIs overlaid on DKI motion corrected image; **(D)** Scatter plots of FA and MSK in group subjects across aforementioned ROIs: colored spots indicate single subject's value for each metric; as reported in the legend, controls' measures are in blue, whereas Periventricular White Matter Injury (PWMI) group's in red. Units for MSK are in mm^2/s, while FA is dimensionless. Error bars displaying mean (diamond) and standard deviation (bars) are overlaid on scatter plots.

Chapter 8

Data-driven characterization of Preterm Birth through intramodal Diffusion MRI

8.1   Background

In Chapter 7 we investigated the applicability of HARDI to SC region in preterm neonates. Given that cerebral WM is the major target of anomalies associated with preterm birth, in this Chapter we shifted to explore WM brain maturation of preterm subjects acquired at TEA. Indeed, despite the development of monitoring and treatment technology in the neonatal intensive care unit, the incidence of preterm birth is still increasing worldwide (Beck et al., 2010; Blencowe et al., 2013), with surviving neonates often meeting high rates of neurodevelopmental impairments (Bhutta et al., 2002). These sequelae have been attributed to perinatal brain injury, particularly when this involves WM, with the severity of WM injury being predictive of neurodevelopmental outcome in later childhood (Dyet et al., 2006; Kimpton et al., 2021). Thus, increasing the understanding of WM microstructural development between birth and term equivalent age in preterm infants with normal or abnormal neurodevelopment may be informative to identify specific and early markers of WM maturation both in case of normative and of adverse neurodevelopmental outcomes.

As such cerebral alteration occurs beneath an anatomical scale, being therefore undetectable by conventional imagery, dMRI has established as the most valuable tool to inspect this altered WM development in preterm infants (Counsell et al., 2003; Volpe, 2003). For instance, previous neonatal brain DTI studies indicated that WM FA increases with age, even before myelin is evident on conventional MR imaging sequences, and diffusion parameters correlate with cognitive, language, and motor outcomes (Hüppi et al., 1998a; Partridge et al., 2004).

If examination of WM development in preterm neonates by using DTI, sensitive to microstructural organization, is by then recognized as a standard clinical tool to identify neonates at high risk of neurodevelopmental impairment, the recent advent of HARDI imaging represents a promising tool for enhancing our understanding of WM maturation compared with standard DTI metrics alone (Kunz et al., 2014). Most recent studies show how higher-order diffusion models (e.g., DKI (Ouyang et al., 2019b; Shi et al., 2016; Zhao et al., 2021), NODDI (Kelly et al., 2016) or CSD (Pannek et al., 2018)) may offer unique insight into the postnatal neurological development associated with differential degrees of preterm birth, thanks to their improved sensitivity to microstructural changes both in WM and GM.

Indeed, opposed to isolated WM injury, impaired neurodevelopment in preterm infants represents a complex interplay between GM and WM damage, leading to structural changes throughout the entire brain to which DTI may not be so sensitive (Tymofiyeva et al., 2012). Moreover, by relating the diffusion signal more directly and specifically to underlying cellular microstructural properties, HARDI methods allow to investigate WM microstructure with higher levels of detail, and to potentially give access to richer microstructural properties, thus increasing the diagnostic values of their derived measures. Cutting-edge methods of microstructural brain imaging are thus expected to provide unprecedented insights into early brain anomaly leading to subsequent adverse outcomes, often intrinsic to very preterm birth and whose accurate prediction is imperative for the implementation of early interventions in clinical practice.

However, as far as we are aware, existing works all focus on investigating alterations of pre-term brain resorting to one microstructural model at a time. Conversely, a combination of multiple models may be extremely useful to offer complementary information about tissue microstructure, given also the lack of systematic model-to-model comparisons to assess which are the best markers to reliably quantify microstructural tissue maturation in newborns. Specifically, in this study,we examined four models among the most used in pediatrics: DKI, NODDI, MSMT CSD and FORECAST – for further and specific details see Appendix A – selected for their suitability in grasping microstructural changes beyond DTI's capabilities (Pecheva et al., 2018).

Our work thus primarily aims at investigating the potential of an intramodal approach to dMRI, made up of several microstructural dMRI models, in extracting relevant markers of prematurity. Furthermore, with a view to deeply inspect each of the microstructural-derived measures, we also seek to assess their robustness to the method of investigation in use. To do so, we opted for comparing two state-of-the-art methods for large-scale longitudinal

neuroimaging studies, that is Tract-Based Spatial Statistics (TBSS) and Machine Learning (ML) classification.

TBSS is an automated, observer-independent approach for assessing FA in the major WM tracts on a voxel-wise basis across groups of subjects (Smith et al., 2006). It achieves this through carefully tuned alignment of FA maps to a standard-space template, followed by projection of individual data onto a skeletonised representation of major WM tracts common to the group to circumvent the PVE and gain statistical power from this dimensionality reduction. Since WM dysmaturation is increasingly recognized as the primary pathology in contemporary cohorts of preterm neonates, this method has been used extensively on scans acquired at TEA in preterm-born neonates to successfully detect alterations in WM microstructure in the absence of overt brain injury (Alexandrou et al., 2014; Anjari et al., 2007) and to predict cognitive and motor outcomes in young preterm-born children (Counsell et al., 2002; Duerden et al., 2015),which is highly relevant to clinicians making essential care decisions. The reasons behind popularity of TBSS reside in being an objective, sensitive and relatively easy to interpret method for multi-subject, whole-brain diffusion data analysis. This allows to overcome some of the limitations of common ROI-based approach to analyze neonatal data, which suffers from subjectivity, manual intensity, intra- and inter-subject variability, and a priori spatial localizaation, which makes it suboptimal for comparison of several brain regions or large subject groups (Ly et al., 2015). At the same time, the approach does not require data smoothing and could alleviate many concerns raised regarding other conventional fully automated whole-brain measurement techniques such as voxel-based morphometry (VBM) framework that was previously used in many DTI studies (Whitwell, 2009).

Although remaining the leading technique for voxel-wise DTI analysis, as any other voxel-based analysis method, application of TBSS does not come without pitfalls, including: influence of noise level, parameter settings, choice of the template, quality of image registration on the resulting anatomical specificity, the low sensitivity for detecting wide-spread subtle abnormalities, the impossibility to develop individually-based imaging indices. All these factors in turn question reproducibility and robustness of the final TBSS result, being essential for establishing biomarkers and diagnostic/prognostic indices at the individual level (Bach et al., 2014).

In this respect, the advent of ML in the early 2000s has totally revolutionized neuroimaging studies. Indeed, compared to population-based analysis, ML approaches can extract unbiased, individualized biomarkers of diseases or functional brain states of fundamental importance in diagnosis, prognosis, and patient stratification (Davatzikos, 2019). Earlier

studies focused on Support Vector Machines (SVM) (Golland et al., 2002; Lao et al., 2004), which has been a cornerstone in this field, largely because of its robustness and ease of use with a variety of kernels (Schölkopf et al., 2002). These and other methods have already been widely applied in neuroimaging studies regarding preterm birth (Chu et al., 2015; Galdi et al., 2020; Saha et al., 2020), with the vast majority of works resorting to TBSS or other VBM methods as a preprocessing step preparatory to application of ML algorithms. However, to the best of our knowledge, this is the first study using TBSS and a ML-based classification jointly on intramodal dMRI to explore the most discriminating WM regions as biomarkers to supplement the understanding of such a current phenomenon as preterm birth.

8.2 Matherials and Methods

8.2.1 Subjects

A total of forty-seven preterm and twenty-three term-born subjects have been enrolled between November 2017 and August 2021 at the Neuroradiology Unit of Gaslini Children's Hospital. Conventional MRI and DKI were performed using a 3.0T MRI scanner (Ingenia Cx, Philips, Best, the Netherlands) with a 32-channel head array coil.

This single-center study was carried out in accordance with the recommendations of "Comitato Etico Regione Liguria, Genoa, Italy" with written informed parental consent obtained for each infant prior to examination in accordance with the Declaration of Helsinki. All the precautions for patient's feeding, sedation, position and monitoring, adopted also in the work on spine from Chapter 7, were replicated for this study.

Exclusion criteria included obvious motion artifacts, oblique positioning, an incomplete imaging process or a low SNR.

GA was used as a classifying variable for preterm (GA < 37 weeks) and term birth (GA $\geq$ 37 weeks). Preterm subjects have been acquired at TEA, as dictated by clinical procedure. Our cohort was further stratified according to the presence of brain pathologies. Unhealthy subjects within pre-term group comprise infants diagnosed with a variety of clinical anomalies common to prematurity: the most numerous one are Periventricular Leukomalacia (PVL; 5 subjects), followed by Intra Ventricular Hemorrhage (IVH; 4 subjects) and Germinal Matrix Hemorrhage (GMH; 4 subjects).

Similarly, patients in the term group exhibit a wide range of brain anomalies, as expected when collecting subjects in a real clinical scenario. The most frequent pathology we registered was asphyxia (3 subjects).

Instead, patients with germinolytic cyst or Cavum Veli Interpositi (CVI) were included in the healthy group. Details about subjects' demographics are reported in Table 8.1.

Table 8.1 Demographic features of infants-brain

	Preterm infants (n=46)		Term born infants (n=23)	
	Unhealthy (n=21)	Healthy (n=25)	Unhealthy (n=11)	Healthy (n=12)
Gender (M/F)	9/12	5/20	8/3	7/5
Mean GA (range; week)	30.36±2.53 (25.28-36.71)	31.84±2.37 (28.86-36.28)	38.75±1.63 (37-41.57)	39.5± 1.34 (38-41.71)
Mean PNA (range; week)	7.89±3.81 (1.43-14.29)	8.20±2.80 (1.86-13.86)	3.13±3.19 (0.14-10.14)	1.81±1.15 (0.71-4)
Mean PMA (range; week)	38.25±2.71 (32.86-42.29)	40.05±1.94 (37.14-47.57)	42.68±2.76 (39.14-48.43)	40.57±1.96 (38.14-44.29)

*M/F = number of male and female infants; GA = gestational age; PNA= postnatal age; PMA = postmenstrual age.

8.2.2 MR Acquisition

Our acquisition protocol includes Turbo Field Echo (TFE) 3D T1w and a HARDI series. Details about acquisition are reported in Table 8.2.

Table 8.2 Acquisition protocols for structural T1 and HARDI series

	3dT1	HARDI
TR/TE (s)	0.6/0.026337	2.086/0.114
Diffusion Scheme (s/mm²)	–	5 b=0, 30 b=700, 60 b=2800
Flip Angle (°)	90	90
Reconstruction Resolution (mm)	0.38*0.38	1.5*1.5
Reconstruction Matrix	512*512	144*144
Multi-Band Factor	–	2
# Averages	2	1
Slice Thickness (mm)	0.5 without gap	2.2, without gap
Slice Orientation	sagittal	axial
# Slices	251	42
Total Scan Time	4 minutes 5 s	3 minutes 30 s
Partial Fourier factor	–	0.6

8.2.3 Preprocessing pipeline

Structural Images

The first critical step was skull-stripping. We opted for using 3D T1w images as anatomical reference since 3D T2w scans were available only for a subset of subjects. Having to do with neonatal scans, standard skull-stripping methods (Hosseini et al., 2015) such as Brain

Extraction Tool (BET) (Smith, 2000), Robust Brain Extraction (ROBEX) (Iglesias et al., 2011) or BrainSuite (Shattuck and Leahy, 2000) failed in correctly removing non-brain areas, thus requiring manual corrections and introducing both a user- and a subject-based bias. Therefore, we resorted to MASS (Multi Atlas Skull Stripping) (Doshi et al., 2013): a machine learning algorithm which performs brain extraction through a template selection strategy obtaining a higher accuracy than recent state-of-the-art tools and avoiding user's intervention. As a preliminary step, 3D T1w images were FOV-reduced, processed with BET, and then bias-field corrected with N4 algorithm to suppress low-frequency inhomogeneities (Tustison et al., 2010).

At this phase, under supervision of a board-certified neuroradiologist, we selected six subjects that best represented the anatomical variations within the dataset, and processed this cohort with the developing HCP (dHCP) pipeline (Hughes et al., 2017a). This workflow requires both 3D T1w and 3D T2w images, their associated binary masks as well as information about GA, and automatically outputs structural betted images and relative masks at the expense of a high computational cost.

The six 3D T1w betted images generated with dHCP pipeline were subsequently used as a reference template to train MASS algorithm. A final re-run of N4 algorithm ensured bias-field correction using the correct mask extracted with MASS framework instead of the rough one after preliminary brain extraction with BET. All preprocessing relative to structural scans is summarized in Figure 8.1a.

HARDI scans

As already mentioned, HARDI scans in pediatrics are really sensitive to low SNR, more prone to macro as well as micro sources of movements. For the same reasons as in the work on neonatal SC from Chapter 7, we confirmed Patch2Self (Fadnavis et al., 2020) as the very first preprocessing step as regards diffusion imaging. This denoiser turned out to be particularly suitable for higher order diffusion models, outperforming other existing methods at visual and modeling tasks. The method is implemented in DIPY v.1.4.0 (Garyfallidis et al., 2014) and applied with OLS regressor, with the threshold for $b = 0$ shell at 100, given the variability of non-diffusion-weighted b values. We opted for applying denoising at the very beginning of the preprocessing pipeline since, out of several attempts, this option produced the best outcome in term of quality of downstream parametric measures.

All subsequent preprocessing steps were done in Mrtrix3 v.3.0.1 (Tournier et al., 2019). Standard analysis pipeline performed well also on neonatal scans thanks to overall good image contrast. We thus carried out: (i) denoising again through `dwidenoise` command;

(ii) unringing with `mrdegibbs` command; (iii) EPI-distortion correction, eddy-current and movement distortion correction with `dwifslpreproc`; (iv) B1-field inhomogeneity correction with `dwibiascorrect` command through *ants* algorithm. Similarly, all preprocessing relative to diffusion images is displayed in Figure 8.1b.
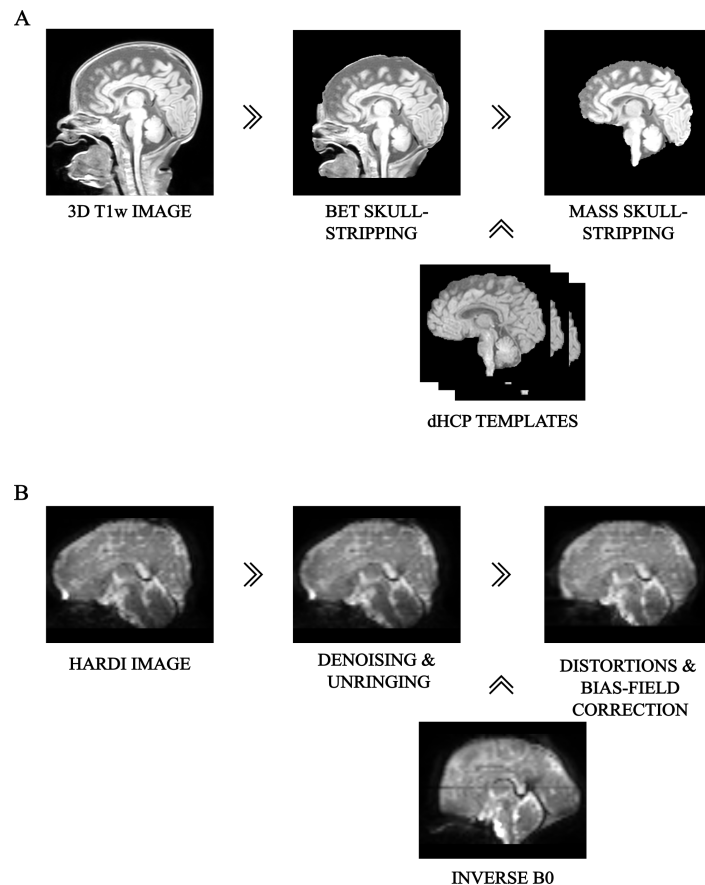
Figure 8.1 **Preprocessing pipeline:** overview of the main preliminary image processing steps performed on: **(A)** 3D T1-weighted, whose key step is skull-stripping and **(B)** HARDI scans, whose core is represented by denoising as well as distortion correction, for an example subject.

Microstructural models

This was the starting point for application of multiple advanced microstructural dMRI models, which were easily employed to this cohort thanks to overall high image quality (Figure 8.2). Outcome produced by each model has been subject to inspection by two experienced neuroradiologists and compared with existing studies on age-matched cohorts. A more detailed compendium about the microstructural models used in this work can be consulted at

Appendix A. Furthermore, to avoid spurious contributions from non representative image portions as well as to reduce computational time, all models have been applied to a masked version of the data derived from averaging and skull-stripping the non-diffusion weighted pre-processed volumes.

Diffusion Kurtosis Imaging   We performed estimation of diffusion maps through DIPY v.1.4.0, (https://dipy.org) (Garyfallidis et al., 2014). Standard DKI parametric maps (MK, AK, RK, KFA) were thus generated (https://dipy.org/documentation/1.0.0./examples_built/ reconst_dki/). In line with the work from previous Chapters, since kurtosis measures are susceptible to high amplitude outliers, we removed their impact by limiting metrics' extraction within the typical range (0,3).
Patch2Self once again proved to improve reliability and accuracy of downstream analyses. Specifically, it turned out to be suitable for DKI model since it reduces the number of degeneracies in parameters' estimation without adding any artifacts due to denoising.

Neurite Orientation Dispersion and Density imaging   We computed NODDI-related measures (ICVF, ISOVF, ODI) with linear framework for Accelerated Microstructure Imaging via Convex Optimization (AMICO) implemented in Python (https://github.com/daducci/ AMICO), which, through a convex optimization approach, drastically accelerates the fit of existing higher-order dMRI techniques while preserving accuracy and precision in the estimated parameters, thus meeting real application demands (Daducci et al., 2015).

Fiber Orientation Estimated using Continuous Axially Symmetric Tensors   We resorted to DIPY also for computation of measures derived from Fiber Orientation Estimated using Continuous Axially Symmetric Tensors (FORECAST) model (https://dipy.org/ documentation/1.1.1./examples_built/reconst_forecast/). We used 6 as spherical harmonics order (*sh_order*) for the fODF and CSD as spherical deconvolution algorithm for the FORECAST basis fitting (*dec_alg*) to extract crossing invariant tensor indices.

Multi-Shell Multi-Tissue Constrained Spherical Deconvolution   Application of MSMT CSD has been performed in MRtrix3. For response function estimation, used as the kernel by the deconvolution algorithm, we resorted to *dhollander* approach, suitable for computing MSMT response functions in case of multi-tissue variants of SD and more reliable in case of neonates (Dhollander et al., 2019, 2016). In principle, the number of tissue types that can be resolved by MSMT CSD is limited by the number of *b* values in the data, including

$b = 0$ shell. As a result, our acquisition, made up of 3 unique b values, would be able to resolve the three primary tissue types in the brain (WM, GM & CSF). However, given the poor WM/GM contrast inherent to neonatal scans (Dhollander et al., 2018), we were limited to extracting tissue-specific ODF just for WM and CSF. Moreover, since interested in performing population studies, we used the same response function for all our cohort. To this end, we calculated the average tissue response function for all our subjects, using `responsemean`, just for WM and CSF responses.

Structural Connectomes

To deepen the characterization of our cohort of patients and in view of future developments of the current work, we also carried out computation of structural connectomes from our HARDI dataset. As usual, default Mrtrix3 procedure for connectome contruction (https://mrtrix. readthedocs.io/en/dev/quantitative_structural_connectivity/structural_connectome.html) is conceived for adult imaging and thus does not apply properly in case of infants. Specifically, having to do with neonatal scans, we favoured preventing spurious streamline terminations and thus opted for performing Anatomically-constrained tractography (ACT) (Smith et al., 2012) in order to improve our streamline tracking based on effective anatomical information and biological priors.

At this step, we encountered issues in generating a 5-Tissue-Type (5TT) segmented image appropriate for ACT, since Mrtrix3 default tissue segmentation algorithm `5ttgen` does not perform well in neonates (WM/GM tissue signal contribution is often mixed with preponderant GM). We thus resorted to a recently-developed pipeline (Blesa et al., 2021) (https://git.ecdf.ed.ac.uk/jbrl/neonatal-5TT/) and reformulated it to fit our case.

This method integrates different resources: (i) FSL (https://fsl.fmrib.ox.ac.uk/fsl/fslwiki); (ii) MRtrix (http://www.mrtrix.org/); (iii) ANTs (http://stnava.github.io/ANTs/) to create the 5TT file and the parcellation needed to generate the connectome using ACT in the neonatal brain.

Different approaches can be found in the literature (Batalle et al., 2017; Blesa et al., 2019; Lennartsson et al., 2018), but we readapted this work since fully automated, freely available and respecting as much as possible the underlying anatomy of the neonatal brain.

To do so, it relies on manually parcellated images in ten individuals that comprise the original Melbourne Children's Regional Infant Brain (M-CRIB) atlas (Alexander et al., 2017) (https://github.com/DevelopmentalImagingMCRI/M-CRIB_atlas), with Desikan-Killiany compatible cortical regions. As a first step, to obtain the parcellation, we performed intensity histogram matching (`mrhistmatch` command in Mrtrix3) between the T1 preprocessed M-

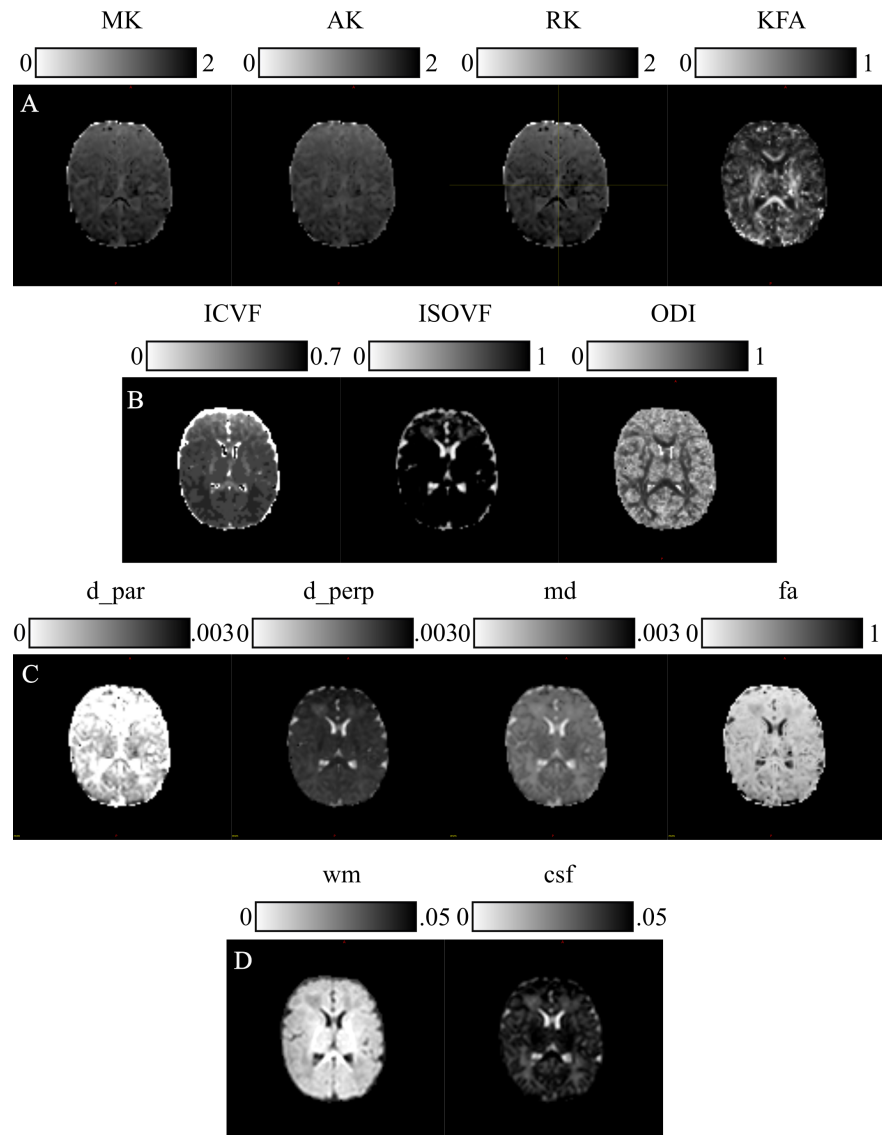Figure 8.2 **Microstructural Models:** parametric scalar maps derived from all the HARDI models employed for this study: **(A)** Diffusion Kurtosis Imaging (DKI), **(B)** Neurite Orientation Dispersion and Density imaging (NODDI), **(C)** Fiber Orientation Estimated using Continuous Axially Symmetric Tensors (FORECAST), **(D)** Multi-Shell Multi-Tissue Constrained Spherical Deconvolution (MSMT CSD).

CRIB templates registered to T2 and our subjects' T1 resulting from MASS skull-stripping, based on their respective binary mask images (`fslmaths` command in FSL).

Then, we customized segmentations from M-CRIB atlas labels to each subject's T1 using `antsJointLabelFusion`image fusion algorithm (Wang et al., 2012), adding as an output the probability labels. Finally, to obtain the 5TT, we simply combined (`fslmaths` command in FSL) the obtained probability labels for each subjects separating cortical and subcortical GM, CSF, and WM, respectively. In addition, we normalized these tissue probability maps between 0 and 1. The latter have been merged together (`fslmerge` in FSL) to result in the final 5TT segmented image, displayed in Figure B.7. From this step, standard commands for structural connectome construction in Mtrix3 were applied.

Specifically, for each subject, we registered the T1, the resulting 5TT file and the M-CRIB labels to to the mean $b = 0$ diffusion image, though keeping its higher resolution through `trasformconvert` command. We then reordered the labels using `labelconvert`, for extracting the relevant (84) GM parcellations from the default neonatal FreeSurfer segmentation (M-CRIB). After applying MSMT CSD from previous paragraph, we normalised the tissue components corrected for the effects of residual intensity inhomogeneities (`mtnormalize`). Furthermore, in order to reduce memory consumption and allow faster tracking, we reduced the spatial resolution of the FOD image (using `mrgrid`). These corrected and downsampled FODs, together with the registered 5TT file for each subject were the input of `tckgen` command for tractogram generation, with streamiline seeding on the GM-WM interface and a reduced FOD amplitude cutoff threshold (0.05). Indeed, this allows streamlines to reach the GM-WM interface more reliably, and does not result in significant false positives since the MSMT algorithm does not produce many erroneous small FOD lobes. Subsequently, we applied the Spherical-deconvolution Informed Filtering of Tractograms (SIFT) algorithm, a method which reduces the overall streamline count, but provides more biologically meaningful estimates of structural connection density. Finally, as last step, we mapped streamlines to the parcellated image to produce connectomes using `tck2connectome`.

Resulting connectivity matrices for two representative subjects can be visualized in Figure B.8.

8.2.4   Post processing

Tract-Based Spatial Statistics

FA skeleton generation   Once applied all the microstructural models and extracted the related metrics, we first used TBSS, themost popular voxel-wise statistical inference for WM

anatomy (Bach et al., 2014), to inspect potential per-voxel differences across microstructural derived markers typical of preterm birth compared to term born controls. However, once again neonatal imaging caused standard TBSS pipeline developed in FSL (https://fsl.fmrib.ox. ac.uk/fsl/fslwiki/TBSS/UserGuide) to present technical challenges in case of neonates, due to smaller anatomical dimension and lower image contrast and resolution. We thus integrated it with DTI-TK (http://dti-tk.sourceforge.net/pmwiki/pmwiki.php?n=Documentation.TBSS), as suggested also in the literature (Bach et al., 2014; Tokariev et al., 2020).

The latter is a spatial normalization and atlas construction toolkit optimized for examining WM morphometry resorting to tensor-based registration able to leverage rich discriminating features afforded by DTI.

As a first step, we computed DTI tensor for each subject using FSL command `dtifit`, given DTI-TK interoperability with FSL - it is conceived as an FSL plugin. Specifically, we opted for computing the DT limiting to the b=700 s/mm^2 shell instead of using the whole multi-shell diffusion volume. Indeed, this was the alternative producing the best outcome in later analysis steps (e.g., TBSS FA skeleton generation). As usual, we limited tensor estimation within a binary mask generated from non diffusion-weighted averaged volumes. We then converted FSL-generated DTI eigensystem volumes into fully DTI-TK compatible DTI volumes, (i.e., both in the correct format, physical unit of diffusivity and correctly preprocessed) using `fsl_to_dtitk` script. To further make sure of the correctness of the conversion, we visually inspected each subject's DT using tensor glyph tool (`TVglyphview` in DTI-TK). Indeed, effective visualization of DTI volumes in 3D is imperative for processing and analyzing this type of data. We then moved to the registration and spatial normalization of DTI volumes, which is the core functionality of DTI-TK.

We opted for bootstrapping a population-specific DTI template from our specific cohort of study without relying on an existing template, given the age range under analysis (`TVMean` command in DTI-TK). To this end, rather than few subjects, we employed all datasets to build our ad-hoc template because, although computationally more intense, this allows to better capture within-population features. Once the common DTI template was created (Figure B.9), we performed tensor-based registration of each subject to the template space, through consecutive steps aimed at iteratively refining the template and improving the registration outcome (rigid, affine and deformable alignment of DTI volumes achieved through `dti_rigid_population`, `dti_affine_population` and `dti_diffeomorphic_population` DTI-TK commands, respectively).

The last custom implementation of TBSS has the aim to: (i) generate the spatially normalized high-resolution DTI data, i.e., with a spatial resolution of isotropic 1 mm^3

(`dti_warp_to_template_group` command), (ii) generate the population-specific DTI template with the isotropic 1 mm³ spacing; and (iii) generate the FA map of the high-resolution population-specific DTI template (`TVTool`). Therefore, resorting to FSL default command `tbss_skeleton` the WM skeleton from the high-resolution FA map of the DTI template is created for running the subsequent TBSS analysis. Finally, after producing each FA map of the spatially normalized high-resolution DTI data (`TVTool`), they are all merged (`fslmerge` in FSL) to form a 4D FA map and its corresponding binary mask.

Previous procedures in DTI-TK replaced the first three steps of standard TBSS pipeline (`tbss_1_preproc`, `tbss_2_reg`, and `tbss_3_postreg`, respectively). From this point on we thus moved to default procedure in FSL with the last two steps, that is `tbss_4_prestats` and stats (`randomise`). The first one aims first of all at thresholding the mean FA skeleton image at a suitable threshold. The latter is chosen by visual inspection, setting a value able to retain common major WM tracts avoiding those subject to excessive cross-subject variability and where the nonlinear registration has not been able to attain good alignments - 0.1 in our case, consistent with other works on neonates (Ball et al., 2010). Later, it projects all subjects' FA data onto the resulting mean FA skeleton. This 4D image file containing the projected skeletonised FA data is thus fed into voxelwise statistics. In order to find voxels which significantly differ between our two cohorts in comparison, cluster-size thresholding was applied to the data, in which the size of the cluster was determined by 500 permutations by using Randomise FSL's tool (http://fsl.fmrib.ox.ac.uk/fsl/fslwiki/Randomise). A threshold of $p < 0.05$ (95th percentile of the distribution) was set for the clusters, corrected for multiple comparisons across space. This is somewhat similar to cluster-based thresholding, but generally more robust and avoids the need for the arbitrary initial cluster-forming threshold. We thus generated both a design matrix file (*design.mat*) and contrasts file (*design.con*), through the script *design_ttest2* as our case consisted of a simple two-group comparison.

Non FA metrics   In order to extend TBSS analysis to diffusion-derived measures other than FA, we repeated DTI-TK/TBSS steps with some variations, similar to what done in (Timmers et al., 2016). Indeed, `tbss_non_FA` script included in FSL implementation was not directly applicable due to previous integration with DTI-TK. We first needed to adjust the header for all HARDI measures (except for NODDI markers) in order to assure the same orientation in DIPY or Mrtrix3 and DTI-TK format. We thus resorted to `fslcpgeom` command in FSL to integrate the q-form into headers generated by external programs, which neglect it unlike DTI-TK. We thus moved to convert each microstructural scalar map to the DTI-TK coordinates (`SVAdjustVoxelspace` in DTI-TK). Then, we reapplied to each measure the

original nonlinear registration obtained to transfer each FA map to the population-specific template (`deformationScalarVolume` in DTI-TK).

We then merged (`fslmerge` in FSL) all subjects' warped data into a 4D file and created the relative mean map (`SVMean` in DTI-TK) together with its binary mask. Analogous to FA, we then projected this onto the original mean FA skeleton (using the original FA data to find the projection vectors), resulting in the 4D projected data. We were thus able to run voxel-wise stats on the projected 4D data in the same manner as described above.

This procedure was repeated for each of the microstructural measure analysed in the current work.
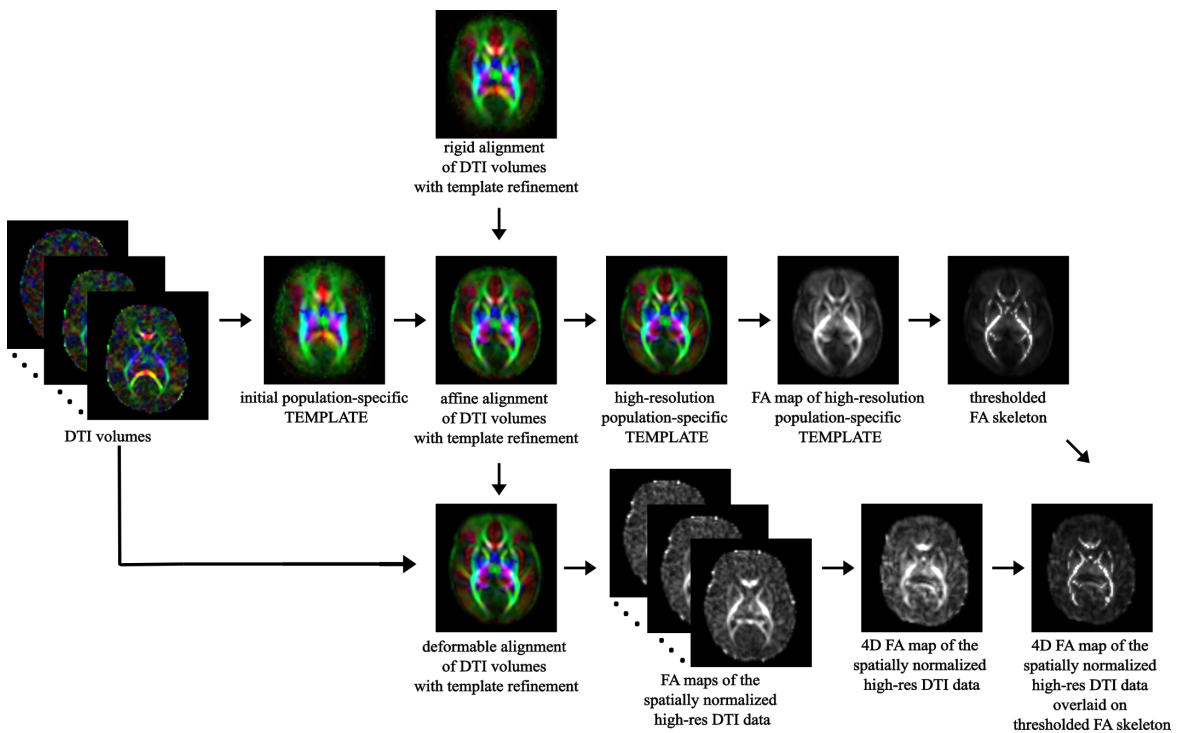
Figure 8.3 **TBSS pipeline:** overview of the main steps of TBSS framework, from spatial normalization of DTI volumes, to bootstrapping the within-population template, to skeletonisation of the template's FA map and projection of each subject's FA onto the skeleton.

Predictive model

Machine Learning methods for classification   Moving to ML analysis, we performed preterm/term-born subject classification based on a predictive model. A crucial remark is that we only have access to a small amount of data to train our model. This might cause overfitting, a very well-known issue in ML, which occurs when the classifier learns noise and

random fluctuations in the training data and does not generalize to the test data (i.e., unseen data). The main causes of overfitting are indeed a small number N of samples in training or the high complexity of the model (e.g. large number P of input variables).

We thus resorted to a SVM framework to categorize preterm-born and term-born individuals based on whole-brain WM skeleton estimated using TBSS from DTI scans. Indeed, among the variety of ML techniques applied so far in neuroimaging settings, SVM has emerged as one of the most popular ML methods (Chin et al., 2018; Chu et al., 2015), able to effectively cope with high-dimensional data and provide good classification results, thus avoiding overfitting of the data (Vapnik, 1999). The fundamental aim of SVM is to classify data points by maximizing the margin between classes in a high dimensional space (Sain, 1996). In brief, an optimal classifier is constructed through a "training phase", whereby key brain features are identified in order to distinguish between two groups, which is then applied to categorize new, unseen data in the "testing phase".

Along with adopting SVM classifier to handle the issue of overfitting, we also carried out a further analysis to investigate how the performance changes by varying the input dimension P of our data through feature selection (see Experimental design section for details) and, then, we trained a classification model based on related findings. For implementation of ML method, we resorted to scikit-learn free software ML library for the Python programming language (https://scikit-learn.org/stable/).

Experimental design   The experiments we carried out can be subdivided into two phases (Figure 8.4).

In the first phase (Figure 8.4A), we adopted SVM to perform binary classification starting with the FA map warped to common TBSS space and masked by thresholded WM skeleton for all 69 infants involved. This corresponded to a 69×2286 input matrix, equal to the number of subjects by the number of voxels in the thresholded WM skeleton. We then split the dataset into learning and testing by stratified 5-fold cross-validation ($outer - CV$) in order to increase the numerosity of our dataset while preserving the same class ratio throughout the K folds as the ratio in the original dataset.

For each fold, we thus applied data standardization (by scaling each feature to (0,1) range) on the learning set and repeated the same procedure for the test set. We then further split the learning set into training and validation sets, named $inner - CV$, for exhaustively tuning the model hyperparameters with GridSearchCV instance. We thus looked for the best hyperparameter grid by choosing the one that produced the lowest prediction error. This set included: (i) the best penalty term C (among 0.001, 0.01, 0.1, 1, 10, 100, 105); (ii) the

best kernel (among linear, radial basis function and polynomial with default degree=3) and (iii) the optimal number of features (selecting 20%, 40%, 60%, 80% and 100% of the input dataset with `SelectKBest` method).

For each combination of hyperparameters, we fitted a model on the training set, we thus evaluated the model performance computing the f1-score on the validation set, and we calculated the averaged f1-score across folds. We thus chose the set of parameters whose average f1-score was the best, we trained an SVM model on the learning set and, subsequently, we evaluated the model performance in terms of accuracy, precision, recall, f1-score, and Receiver Operating Characteristic (ROC) on the unseen test set.

The accuracy score indicates the percentage of labels predicted correctly. The precision score is defined as the ability of a classifier to not mislabel a sample (TP/TP+FP where TP and FP are true and false positive, respectively). The recall, or sensitivity, score is the ability of a classifier to find all the positive samples (TP/TP+FN where FN is the false negative). The f1-score is a weighted harmonic mean of precision and recall. The ROC score is produced by calculating the area under the curve plotting the true positive rate against the false positive rate at a variety of thresholds.

Finally, we computed the mean and the standard deviation of these scores across folds.

In the second phase (Figure 8.4A), once selected the model classifier offering the best performance on FA data, we carried out further analysis for evaluating the classification performance when giving as inputs the parametric measures from other microstructural models than DTI. For each input variable, we again performed the $outer-CV$ to provide a more robust evaluation of the model. We thus trained the model on the learning set and then, we evaluated the model on the test set computing the accuracy, precision, recall, f1-score and ROC. We finally calculated the averaged performance and the standard deviation across folds. Please note that in this phase, we did not perform any $inner-CV$ as we do not introduce a hyperparameters search.
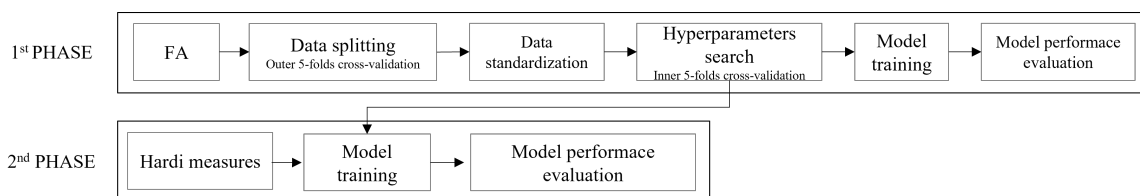
Figure 8.4 **Experimental design for SVM classification:** in a first phase a SVM classification estimator is chosen to best perform on FA skeletonised data; in a second phase the selected model is extended to other non-FA measures.

Weight maps extraction and comparison with TBSS

Finally, in order to relate the results from TBSS with those resulting from ML, we extracted weight maps from the selected SVM classifier within $outer - CV$, averaged them across the 5 folds, normalized between 0 and 1 and reshaped as the input TBSS skeleton (3D image) for mere visual comparison. The weights are SVM coefficients determining the discriminant hyperplane, which depicts the relevance of each voxel for the classification between positive and negative conditions.

We thus computed standard Pearson's correlation between normalized SVM weight maps and TBSS normalized significance maps (p-maps) for each of the microstructural measure analyzed. In order to further inspect the overlap between ML and TBSS WM discriminating regions, we related Pearson's correlation with Wasserstein Distance (WD) metric, to quantify the distance between the two distributions.

8.3   Results

8.3.1   Voxel-wise statistics on the WM skeletonised data

Cross-subject voxel-wise statistics did not unravel any significant difference between the healthy and unhealthy groups, likely due to the heterogeneity and low numerosity of each pathological cathegory. Precisely for this reason, from now on we focused on characterizing discrepancies between preterm and term-born subjects, regardless of the diagnosis. Indeed, cross-subject voxel-wise statistics exhibited significantly different voxels between preterm and term-born groups exclusively on a subset of the microstructural maps under consideration. Specifically, compared with the term cohort, the preterm group showed a significant decrease in FA, MK, AK, ICVF and fa. The WM regions with significant between-group differences in diffusion metrics are shown in Figure 8.5. Conversely, no significant differences have been captured by TBSS analysis in RK, KFA, ISOVF, OD, md, d_par, d_perp either in MSMT-derived measures.

More in detail, compared with the term group, the preterm cohort had significantly decreased FA values in widespread WM areas predominately in the genu, body and splenium of the corpus callosum, right internal capsule, corona radiata, and posterior thalamic radiation. The distribution of areas with decreased MK was similar but extending bilaterally with respect to the areas with decreased FA and including also right external capsule. AK exhibited a pattern analogous to MK whilst comprising bilateral external capsule. The same applies for ICVF metric except for excluding genu of the corpus callosum. The amount of

WM areas showing significant decrease in prematurity increased for fa parameter derived from FORECAST model, which extended to the whole corpus callosum, bilateral internal capsule, external capsule and anterior corona radiata and, finally, posterior thalamic radiation (including the optic radiation).

8.3.2   SVM classification on the skeletonised data

Since the performance of a model significantly depends on the value of its hyperparameters, first of all we carried out hyperparameter tuning in order to determine the optimal values for our classification estimator.

In this respect, Figure 8.6A shows the result of cross-validated grid-search over the parameter grid across each of the 5 folds.

Furthermore, based on the selected hyperparameters, we fitted our model on the training set and evaluated its performance on the test set in terms of f1-score, accuracy, precision, recall and ROC across each of the 5 fold (Figure 8.6B). In order to establish the best estimator possible based on the input data, we counted into how many folds a variable was selected and could thus conclude that penalty term C and *linear* kernel were the most frequently selected hyperparameters. Conversely, the search turned out to be less stable in terms of the optimal number of features, which varied at every fold (Figure 8.6C). Therefore, in order to set the last missing parameter for our estimator, we set C and kernel according their most chosen values while varying the number of features as a percentage of the total amount.

Figure 8.6C confirms that in our case feature selection is not beneficial for improving the classification performance. Indeed, both average value and standard deviation across folds of each score remain constant with variable subset of features.

We thus opted for avoiding feature reduction and kept the whole of features to define the final version of our SVM estimator. As regards this definitive version of the classifier, a detailed plot of the ROC curve profile for every fold is displayed in Figure 8.6D.

We subsequently trained a classification model without hyperparameters' search (*inner-CV*) using as input variables the features derived from other microstructural HARDI models. Once again we evaluated the performance in terms of f1-score, accuracy,precision, recall and ROC. Results for the whole set of microstructural parameters, including FA, are reported in Figure 8.7.
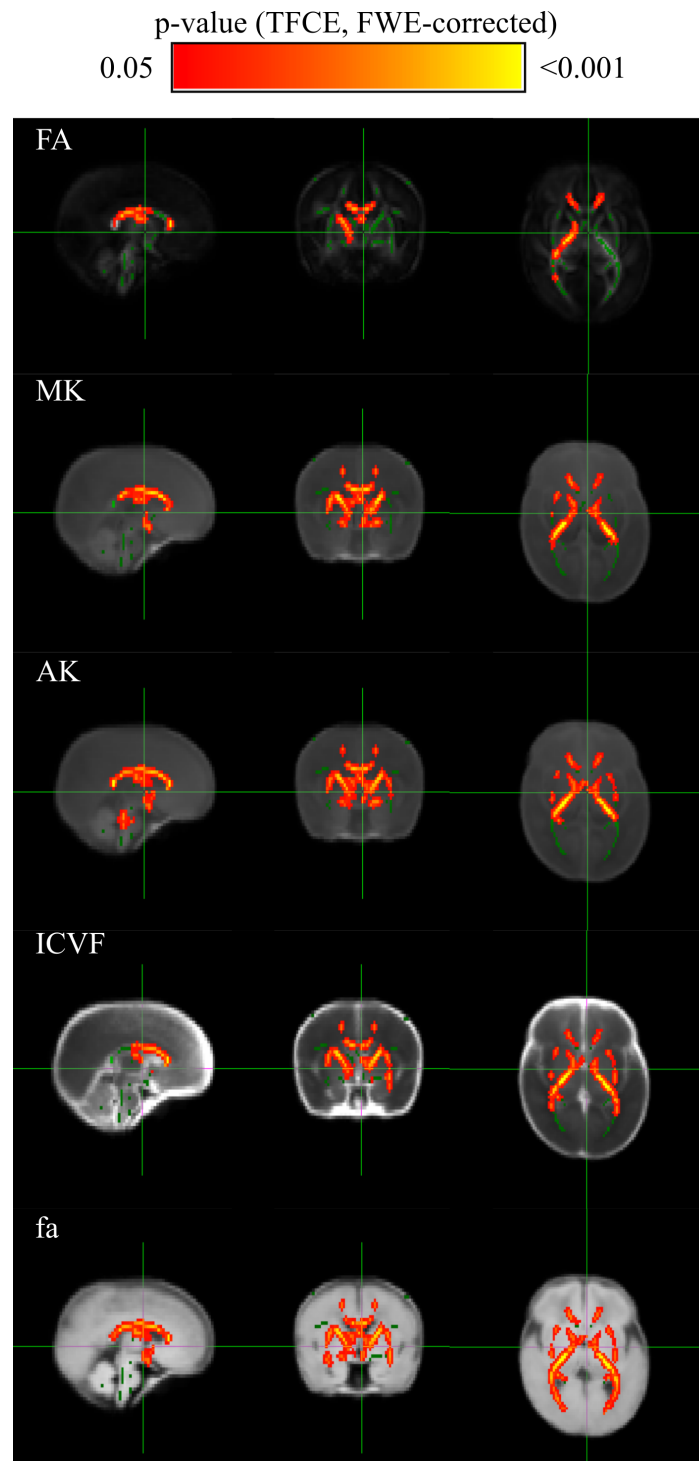
Figure 8.5 **TBSS results:** Group-level voxel-wise statistical difference maps for Fractional Anisotropy (FA), Mean Kurtosis (MK), Axial Kurtosis (AK), Intra-Cellular Volume Fraction (ICVF) and fractional anisotropy (fa) between preterm and term-born cohort. Green indicates the FA skeleton with a threshold of 0.1, which highlights the tracts used in the comparison. Red-Yellow indicates the regions with decreased metrics' values in the preterm group.
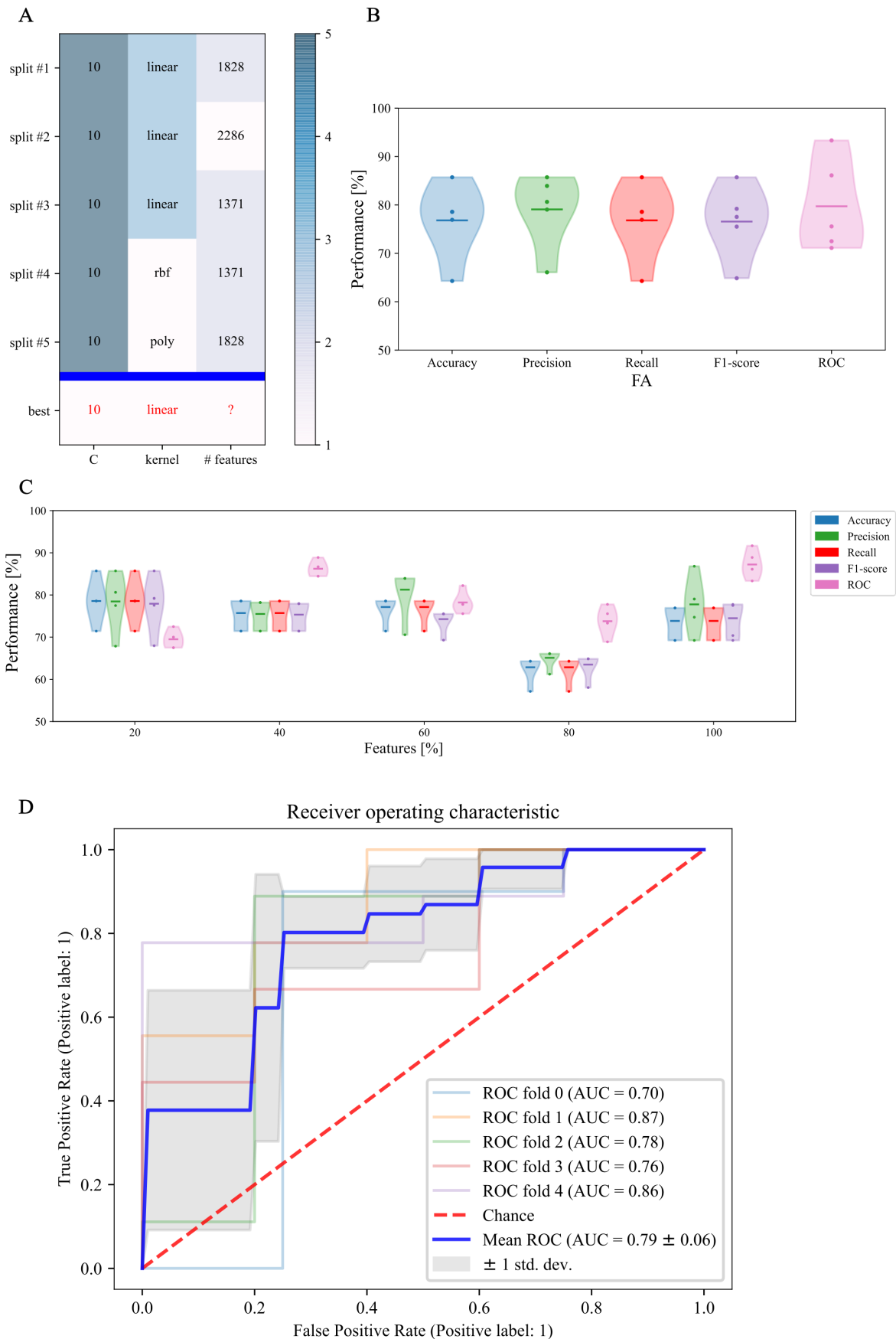
Figure 8.6 **First phase: SVM training on FA skeletonised data: A** cross-validated search of the best set of hyperparameters for our SVM estimator on stratified 5-fold data; **(B)** relative performance for every score across folds; **(C)** Different sets of selected features along with relative performance for every score across folds; and **(D)** area under the curve score
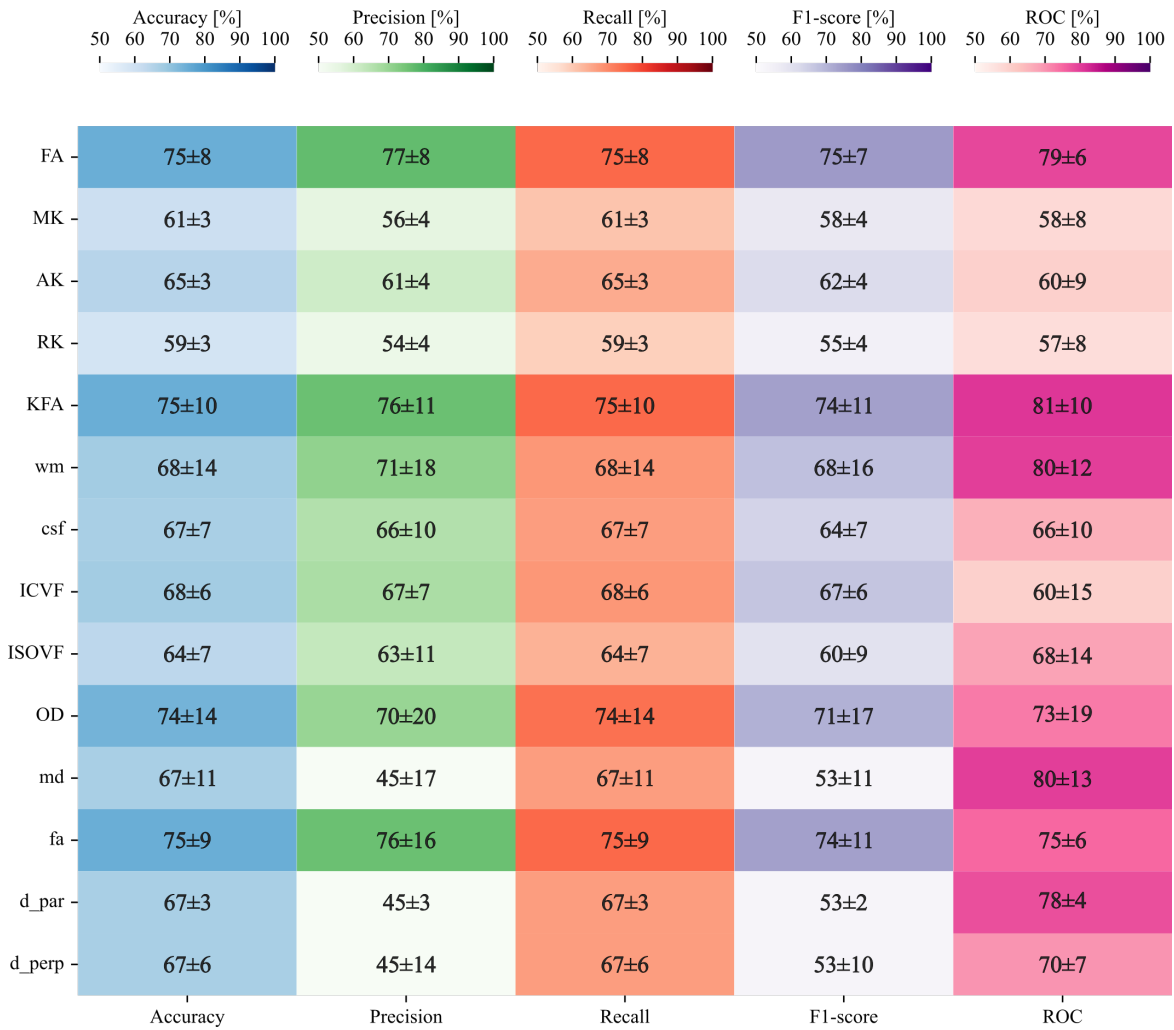
Figure 8.7 **Second phase: SVM testing on non-FA skeletonised data:** heatmap containing average and relative standard deviation, in percentage, of each score and for each of the HARDI measures under analysis.

Table 8.3 Comparison between TBSS voxelwise statistics and SVM classification

	Pearson's r	p-value	Wasserstein distance
FA	-0.45	<0.0001	0.32
MK	-0.34	<0.0001	0.43
AK	-0.33	<0.0001	0.41
RK	-0.46	<0.0001	0.36
KFA	-0.48	<0.0001	0.35
d_par	-0.61	<0.0001	0.20
d_perp	-0.14	<0.0001	0.48
md	-0.33	<0.0001	0.36
fa	-0.28	<0.0001	0.40
wm	-0.14	<0.0001	0.42
csf	-0.11	<0.0001	0.55
ICVF	-0.35	<0.0001	0.36
ODI	-0.51	<0.0001	0.41
ISOVF	-0.05	0.013	0.46

8.3.3 Comparison between SVM and TBSS approach

Relating TBSS significance map with weights extracted from linear SVM showed statstically significant Pearson's correlation for all microstructural measures considered ($p < 10^{-2}$) (see Table 8.3). This relationship was further confirmed by inspecting the association between Pearson's correlation coefficient and WD, reported in Figure 8.8, showing a trend of direct proportionality. Indeed, those measures exhibiting a higher absolute correlation also presented a lower WD, thus confirming similarity between the two methods. Correlation was high (r=0.61) for d_par parameter, intermediate ($r \in 0.45 - 0.51$) for RK, KFA, FA and OD, moderate ($r \in 0.28 - 0.35$) for MK, AK, md, fa and ISOVF and low ($r \in 0.05 - 0.14$) for the last set of measures - d_perp, CSD-related measures and ISOVF. These results suggest an overall good, though measure-dependent rate of agreement between p-maps derived by TBSS approach and weights probing disciminative power of SVM.
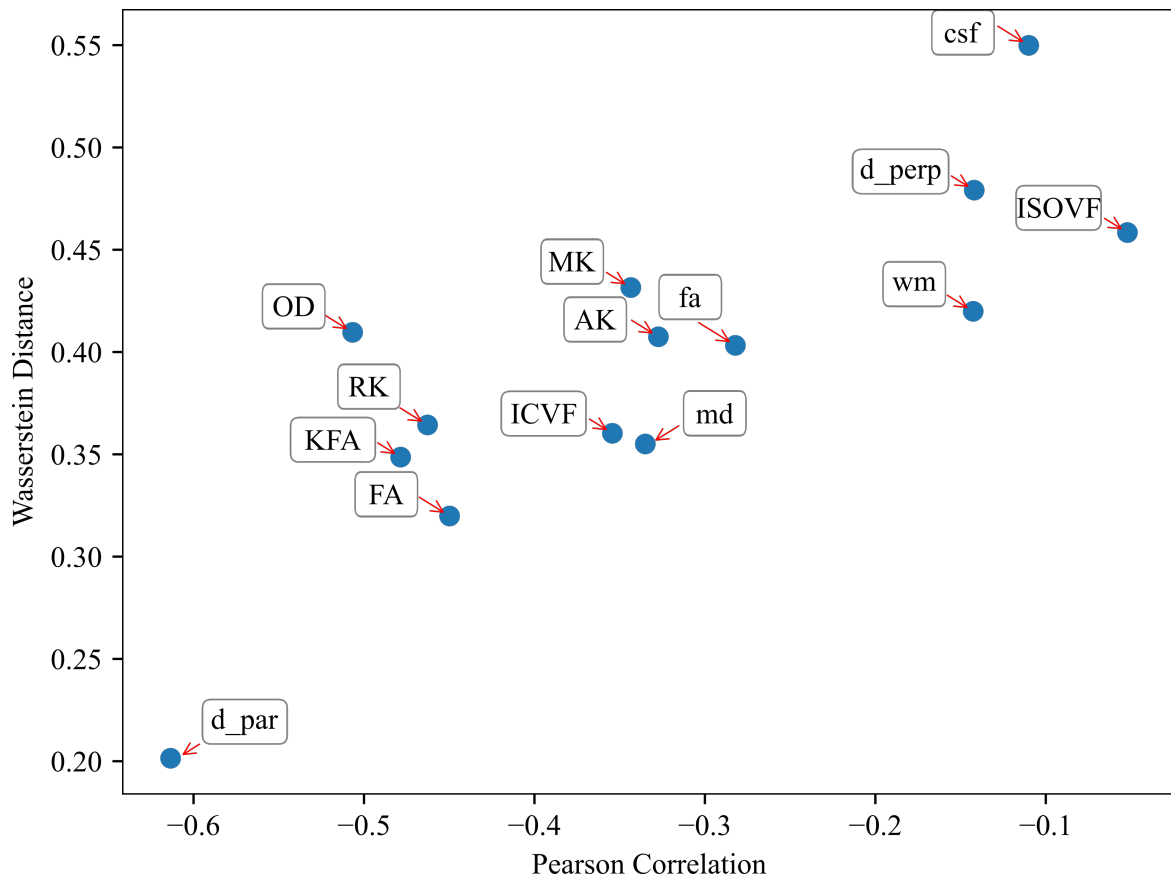
Figure 8.8 **Relationship between Pearson's correlation and Wasserstein Distance for HARDI microstructural models:** the two measures show a good trend of association throughout all HARDI measures considered.

Part IV

Discussion

Chapter 9

Conclusions

9.1 Main Results

The main results of this PhD thesis can be summed up as: (i) the exploration of the influence of magnetic field strength on DKI-derived mesures, starting from a modeling of noise reflecting the true properties of the image and thus more accurate and truthful than the traditional methods used in literature; (ii) the application of this optimal denoising approach as very first preprocessing step within the the first semi-automated pipeline for handling clinical DKI data of neonatal SC, from acquisition setting to estimation of diffusion measures, through accurate adjustment of processing algorithms customized for adults, with a preliminary validation in a pilot clinical case study involving preterm patients ; (iii) the investigation of such a current issue as preterm birth extended to the neonatal brain, explored with the latest HARDI models able to offer new insights into the characterization of tissue microstructure.

9.2 Part II: Denoising as a crucial step in Diffusion MRI

9.2.1 Influence of adaptive denoising on Diffusion Kurtosis Imaging at 3T and 7T

The first approach to validate preprocessing of dMRI scans is almost always done on healthy adult subjects, to obtain a baseline description of the brain's workings.
In the work presented in Chapter 6, we used healthy adult data from HCP in order to inspect the dependence of DKI-derived measures on magnetic field intensity, analyzing denoising approach as the first key factor.

Among the multiplicity of developed denoising techniques specifically tailored for dMRI, we focused on two methods both definable as "adaptive", thus placing the emphasis on the need to abandon too binding noise models. This is the most important prerequisite in case of complex MRI systems, such as acquisition of DKI images making use of parallel-imaging and MB techniques.

In the first part of this work, we thus focused on comparing these two denoising approaches, with particular regard to their application for DKI model.

An important growing prerequisite in medical imaging is development of fast image pre-processing and processing frameworks allowing real-time analysis. Therefore, computational efficiency is one first crucial aspect contributing to overall performance of a denoising algorithm. In this respect, considering current implementation of the two methods under analysis, they proved to exhibit an inversed trend in their computational speed. Indeed, Patch2Self drastically reduces the time required to process dMRI scans from 3T to 7T, unlike NLSAM, whose duration slightly increases. As a result, Patch2Self seems to allow much faster processing of dMRI images, and this gain in time becomes even more relevant with increasing field strength.

Of course, computational performance must be supported by an efficient action of the denoising method in effectively improving image quality. Qualitative evaluation of our already preprocessed HCP scans shows how at 3T contribution of denoising is not substantial, especially for NLSAM. Conversely, UHF scans seem more sensitive to denoising than conventional 3T: at 7T performance of the two methods turns to be not only comparable but also more relevant, as shown from more intense residual plots as well as from improvement in the appearance of DKI images themselves. However, enhancement of DKI maps performed by NLSAM may tend to introduce minimal smoothing/blurring artifacts when denoising, thus not completely preserving raw data.

This qualitative investigation is further corroborated by inspecting impact of denoising on microstructure model fitting, a critical step often leading to degenerate parameter estimates due to the low SNR of dMRI acquisitions. The overall higher quality of fitting at both field strengths confirmed the primacy of Patch2Self via quantitative improvements in microstructure modeling. In addition, the presence of an outlier for NLSAM-denoised data at 7T – corresponding to subject 20, at whom un-denoised data appear to have a higher goodness-of-fit than denoised scan – further supports the hypothesis that Patch2Self is better at preserving raw image features.

Another important factor to consider when fitting higher-order models such as DKI to our data is their susceptibility to estimation degeneracies in derived parametric maps, often

due to noise and signal fluctuations, which may hamper accuracy in subsequent analyses. As precisely regards the number of degeneracies inherent to DKI maps, both qualitative and quantitative analyses agree that performance increases from noisy to Patch2Self- to NLSAM- denoised scans for all DKI measures regardless of the magnetic field strength. This is particularly evident at 7T and in case of highly directional WM areas such as CC, and less relevant in areas of crossing fibers such as ACR. Indeed, number of black voxels is limited at 3T and concentrated in periventricular regions already in noisy images. As a result, denoising just slightly improves the outcome. Conversely, number of degeneracies increases at UHF, with arousal of artefactual signal dropouts likely related to magnetic field inhomogeneities. Denoising contribution here is crucial in decreasing these implausible voxels, and NLSAM outperforms Patch2Self at this task, also thanks to its blurring action. This higher spread and amount of degeneracies at 7T may partly find an explanation in the lower number of directions and b values at disposal to fit DKI model with respect to 3T, due to differences in the acquisition protocol.

In the second part of current study, we moved to inspect variability of MK and KFA measures from 3T to 7T accounting for the denoising method. Regions where denoising does have an impact in determining variation of MK with respect to field intensity are those more sensitive to susceptibility-induced background gradients, that is highly myelinated WM areas such as CC, as well as GM regions rich in iron content as PUT, TH and PAL. In fact, susceptibility gradients contributing to DKI metrics' variation increase with increasing field strength because of the iron- and myelin- related contribution to relaxation (R_2) and magnetic susceptibility of brain tissue (Gelman et al., 1999; Hametner et al., 2018; Möller et al., 2019). This finding is in contrast with (Shaw et al., 2017), where MK had not a substantial field dependence at conventional clinical field strengths (1.5 vs 3T). Indeed, mean difference of this metric for the two field strengths was found to be just a few percent of the average value, and the slopes of the best fit lines for the linear regression analysis close to unit. On the contrary, this agrees with (Palombo et al., 2015), who revealed a significantly positive correlation between MK and $R_2^* = \frac{1}{T_2^*}$ at 3T. Concerning comparison of the two denoising methods, once again it is stressed that their difference in performance is negligible at 3T while getting relevant at 7T.

Regarding KFA, its variations from 3T to 7T seems independent from the denoising step. Indeed, this metric inherently exhibits significant differences in its values with varying field strength, insensitive to the application of denoising. KFA is by far the most variable metrics also in term of denoising approach at both field strengths. This largest relative discrepancy than other DKI metrics agrees with (Shaw et al., 2017), although exhibiting an inverse trend.

Indeed, they found a modest field-dependent bias for this parameter, with a higher KFA at 1.5T than at 3T.

These partial conflicting findings with respect to the only previous work on quantitative comparison of DKI metrics between 1.5T and 3T are mainly due to differences in acquisition protocol, which is known to crucially determine downstream quantitative diffusion measures. In brief, in our work acquisition sequences have been calibrated specifically to obtain the best data quality possible from both field strengths, while in (Shaw et al., 2017) care was taken to minimize protocol differences on 1.5 and 3T scanners.

Along with magnetic susceptibility, another possible cause for DKI parameters' wider variability than DTI ones may be due to higher-order diffusion signal model underlying kurtosis tensor computation: it has largely been shown that effects of noise are greater in estimation of the diffusional kurtosis compared to the diffusivity in both phantom and human data (Jensen and Helpern, 2010). As a result, its definition as the second-order Taylor expansion of the natural algorithm of the true magnitude of the diffusion weighted signal might in part explain DKI susceptibility to other possible differences in scanners (gradient stability, gradient cooling systems, bias field, SNR) and therefore to the wider observed variations.

Take-Home Message

Denoising represents a crucial phase in the pre-processing pipeline of dMRI images, with substantial impact on subsequent analysis steps. As a result, selecting the most suitable denoising method for the kind of data in question is of utmost importance to ensure robustness, accuracy and reproducibility of DKI estimates.

From the current work, the importance of adopting an accurate estimation of the noise profile among all existing denoising methods comes to notice. Comparison of the two chosen techniques acts as a case-study to show differentiated behaviour of different denoising approach and their influence on later steps, such as extraction of model-derived parameters.

Most relevant factors to account for when choosing denoising method for dMRI are microstructural model under analysis, computational efficiency, preservation of anatomical details, consistency of microstructure model fitting, alleviation of degeneracies in model estimation among the many. Specifically, Patch2Self method overall proves to be more suitable for DKI model, starting from faster processing time of utmost importance in clinic.

In general, qualitative and quantitative assessment of DKI measures shows that denoising performance improves with an increase in magnetic field strength. This may partly explain why DKI metrics prove to vary more from 3T to 7T than from 1.5T to 3T. Moreover, DKI

ability to provide additional information on the brain tissue microstructure compared to DTI may be partially due to its sensitivity to susceptibility gradients as another possible source of image contrast. This suggests that potential confounding effects due to adopted denoising approach, T_2 differences, susceptibility gradients and underlying diffusion model play a relevant role at UHF.

9.3 Part III: Feasibility of advanced Diffusion Imaging in neonatal clinical data

9.3.1 Diffusion Kurtosis Imaging of Neonatal Spinal Cord in clinical routine

Once selected the optimal noise model on gold-standard adult data, we moved to its application in pediatric clinical settings. Chapter 7 is focused on the first application of DKI to neonatal SC through a pipeline able to perform complete processing within a clinically acceptable time. As regards acquisition setting, we were able to perform a time-consuming technique like DKI using a short diffusion sequence which minimizes patient's physiological motion, and which likely reflects a standard clinical scenario devoid of latest technologies in terms of acquisition sequence optimization.

Among existing denoising strategies via magnitude data, thanks to its weak assumption about noise properties to be suppressed, Patch2Self showed optimal performance in effectively minimizing the detrimental bias introduced by Rician noise at higher b values. In turn, this minimization reduces error estimates in tensors computation and subsequent derived metrics. With regard to image processing, we opted for creating this pipeline using SCT since it represents the only existing comprehensive, free, and open-source software dedicated to the processing and analysis of SC multi-parametric MRI data. Adaptation of each image processing tools already in use for adult subjects through appropriate tuning of parameters allowed to successfully overcome all the issues mentioned in the Introduction section inherent to imaging of SC and exacerbated in case of neonatal scans. We were thus able to quantify diffusion measures within specific ROIs using an atlas-based approach, automatic and thus highly reproducible, unbiased by the user experience and knowledge of the anatomy, and much faster than long and tedious manual delineation of ROIs.

Present pipeline has been designed to fulfill specific requirements such as short acquisition time and minimal modifications to routine protocol in use at the hosting center. As a result,

any improvement in acquisition setup of our pipeline will bring to even stronger and more comprehensive results. Major limitation of this procedure consists in basing on an adult atlas, although being the only option available. Indeed, the exact location of tracts may not perfectly correspond to neonatal images despite the good adjustment of registration parameters. Moreover, due to short acquisition time dictated by clinical needs and to the lack of specific spatially selective MR sequences, acquired scans are prone to noise and artifacts. Partially borrowed from reference adult study (Panara et al., 2019), our acquisition protocol has certainly room for improvement. For instance, rather than prioritizing voxel size, reducing TE in favour of higher SNR and better contrast could be an option.

We acknowledge the protocol in use to be on the edge for HARDI schemes required by DKI. However, this represents a first attempt to customize advanced dMRI acquisition setting within a clinical routine protocol, already long in itself since made up of multiple MRI sequences in order to increase diagnostic possibilities. Nevertheless, we appropriately addressed this issue at DKI tensor and measures computation phase to ensure reliability and accuracy in their estimates.

After its design, we tested the pipeline in a group of neonates with PWMI, a form of mild WM injury frequently diagnosed in preterm infants. Of note, several studies have showed that greater lesion load of PWMI and the involvement of frontal WM are associated with higher risk of adverse neurodevelopmental outcome, affecting both motor and cognitive functions (Parodi et al., 2019). Moreover, periventricular WM lesions in preterm neonates correlate with region-specific changes in MD, FA, RD, and AD in several cerebral WM tracts that might explain the abnormal development of long-term neurological functions (Cheong et al., 2009). Specifically, the involvement of pyramidal tract fibers in the periventricular WM has been demonstrated to be a relevant factor for motor dysfunction in children with PWMI (Staudt et al., 2003).

In our study, we found that microstructural changes can be detected by using an advanced DKI analysis also in the GM and WM of cSC of preterm neonates with PWMI studied at TEA, thus suggesting that DKI parameters could be used as markers to unravel underlying subtle microstructural lesions. Moreover, our preliminary findings confirm the hypothesis that in preterm neonates with PWMI WM microstructure alterations extend beyond the immediate area of periventricular injury, widening distally also in the cSC (Bassi et al., 2011; Tusor et al., 2017). Hence, these initial results agree with the corresponding adult survey which served as a starting point for the research question addressed in this work. Indeed, since FA is known to be an index of structural integrity (Hansen, 2019) and MSK a marker of tissue microstructure complexity (Jensen et al., 2005), our findings suggest that, in case of

overlying WM brain lesion, a loss of integrity and complexity is registered also in SC WM tracts below with a more isotropic diffusion pattern due to disruption of WM tracts. Also MD, AD and RD (Figure B.6) followed the same trend, with an increase in case of lesioned subjects, as in (Panara et al., 2019). Hence the hypothesis that microstructural impairment of SC could be related to distant lesions of cerebral WM, already verified for adults with stroke lesions, would also subsist in infants with smaller prematurity-related WM lesions.

This study serves as a further evidence that added value of DKI is also found in pediatrics. Results about feasibility of DTI and MSDKI analysis in neonatal SC with subjects collected so far are preliminary but promising and demonstrate the clinical utility of combining DTI and DKI in the characterization of spinal cord pathologies.

FA reduction parallel to MD increase in patients is an expected finding consistent with existing literature and attributable to degeneration of diffusion barrier and loss of diffusion directionality.

Our results suggest that, although yet underused in clinical studies, MSK metrics might have an increased sensitivity in capturing alterations related to pathology, also far from the lesion site. Such findings once again stress the importance of combining DTI and DKI metrics as complementary sensitive biomarkers in order to fully exploit the potential of dMRI compared to conventional MRI. Our results further hint that the presence of a WM lesion in the brain might cause subsequent alterations not only in cSC WM but also in GM, as evidence of the strong association between brain and spine. In this respect, resorting to DKI measures becomes of utmost importance given kurtosis sensitivity to structural changes in isotropic tissues such as GM. Indeed, range of variability of MSK metric from controls to PWMI was overall higher in GM than that of corresponding DTI measures, and a considerable decrease in case of PWMI was registered also in GM unlike for DTI-related parameters.

If FA and, more importantly, MSK measures appeared to be more sensitive to microstructural changes related to pathology both in WM and GM, the same did not apply for WM/GM tissue differentiation. Indeed, MD, AD and RD showed a lower value in GM with respect to WM (including CSTs) for both control and patient group. Conversely, FA and MSK kept comparable values for the two tissues. Since no other studies yet exist about dMRI on this anatomical district in such age range, we had no ground-truth to compare our findings with. However, we hypothesized that, in this cohort of early preterm subjects, WM and GM already differ in terms of amount of diffusivity but yet still not of microstructural organization or of complexity.

Indeed, higher density of cell nuclei in GM than in WM translates in a decreased amount in diffusivity along all directions (mean, axial, radial). In GM, the presence of cell body

contributes to create voluminosity in the environment, which turns into a more restricted diffusion pattern. On the contrary, a parameter like FA, tightly dependent to GA and strongly modulated by myelin growth, may not be yet particularly sensitive to differential microstructure between WM and GM portions. The same happens for MSK, index of microstructural complexity, related to brain maturation and supposedly not so different in SC areas at this early stage.

Further analyses on a wider cohort of neonates are necessary to confirm these preliminary results, possibly investigating also lower SC tracts, and extending to different clinical cases, preferably focused on a determined pathology. For example, it would be interesting to explore long-term correlations between DKI measures and specific clinical scores as done in (Panara et al., 2019), where diffusion measures have been related to motor performance indexes. A further step may be adapting this analysis pipeline to other promising higher-order diffusion models requiring multi-shell acquisition such as NODDI.

Take-Home Message

In this work, we have showed how accurate adjustment and parameters' tuning of processing algorithms customized for adult SC opens up new horizons in exploiting increased ability of advanced dMRI models, also in neonatal domain, where they had never been utilized before. Indeed, even starting from low quality data acquired for diagnostic purposes and thus suboptimal, we were able to extract from DKI information relevant for diagnosis. The case study proposed in this work is just an example of the potential relapses of this semi-automated pipeline, which paves the wave for applying advanced dMRI models to neonatal setting in a wide range of potential clinical applications. In particular, the possibility of successfully exploiting increased sensitivity and specificity inherent to DKI methodology also into neonatal setting would indeed be extremely useful for throwing light on complex diseases related to this critical phase of development and to deepen the knowledge about the relationship between brain and SC at birth.

9.3.2 Data-driven characterization of Preterm Birth through intramodal Diffusion MRI

After investigating preterm subjects in SC region, we opted for addressing such a hot topic in neuroimaging as preterm birth from the brain's perspective, with the additional novelty of resorting to other models besides DKI. In the work from Chapter 8, based on observations that integrating data from different MRI sequences enhances anatomic characterization (Ball et al.,

2017; Kulikova et al., 2015; Thompson et al., 2019), we aimed at combining most popular HARDI-based microstructural models to supplement the understanding of WM differentiation in the preterm cohort for an early clinical diagnosis. Indeed, HARDI acquisitions potentially allow to investigate neurodevelopment with a higher degree of sensistivity and earliness, yet at the price of pitfalls in scanning vulnerable preterm infants. Of note, obtaining good quality images is particularly challenging in this patient group primarily as motion-sensitive and artifact-prone (Jones and Cercignani, 2010).

The first achievement of present work is thus the successful implementation of the overall image processing pipeline able to fully investigate our cohort. This was possible thanks to the setting of a suitable acquisition protocol, fine-tuned to the specific characteristic of infant brain, supported by patient's sedation, monitoring and fixation and resulting in high quality images suitable for HARDI modelling. Another crucial role is played by preprocessing: a dedicated workflow, whose denoising confirmed as an essential step, is here key for subsequent analysis. However, compared to imaging of SC, the design of such a pipeline was widely supported by the existence of software packages and imaging tools already specifically conceived for the pediatric field. Through extensive assessment of data quality, essential to guarantee reliability of images through combination of visual inspection of raw diffusion data and software-based quality checks, this pipeline thus ensured successful application of microstructural models as well as extraction of structural connectomes from the population under analysis.

Moving to actual post-processing, the first tool we considered to investigate the fingerprint of preterm subjects was TBSS. In fact, the analytic method of TBSS offers a number of advantages over hypothesis-directed ROI analyses, in that it describes changes in WM microstructure in a 3D image space. Furthermore, resorting to a population- and thus age-specific template ensured good alignment of DT images and thus success of subsequent analyses, given the vast variability of brain morphology at these early stages of development. By using TBSS analysis of DT images, we demonstrated that both FA and non-FA values can be useful measures to distinguish relevant WM tracts in preterm-born neonates at term age from term-born controls. It was notable that there was a correspondence between the distribution of areas with decreased FA and non-FA measures with an expansion of WM discriminating areas over the main tracts especially in case of beyond-DTI measures.

This agrees with existing findings in literature claiming that: (i) WM maturation is associated with increasing axonal organisation, pre-myelination and myelination, which progressively restricts water diffusion perpendicular to the direction of the axonal fiber; (ii) since premature birth may lead to relatively slow brain development in premature infants,

there are some brain regions that are less developed than the full-term infants. This includes CC, ALIC, PLIC, and, more generally, all tracts subject to early myelination and thus whose metabolism is vigorous and the oxygen demand is high, which makes these metabolically active areas are the first to be damaged in case of risk factors for preterm birth (Ling et al., 2013).

As regard DTI measures, lower FA has been found across the WM in preterm infants compared with term-born infants (Anjari et al., 2007; Hüppi et al., 1998b; Pecheva et al., 2018; Thompson et al., 2011), which correlated with increased prematurity (Ball et al., 2010; Ouyang et al., 2019a; Partridge et al., 2004). Furthermore, WM diffusion measures in preterm infants at TEA have been related to subsequent neurodevelopmental performance. Decreased FA - together with increased MD and RD - in the WM at TEA are associated with worsened motor, cognitive, and language performance in early childhood (Barnett et al., 2018; Counsell et al., 2008) as well as visual function (Bassi et al., 2008; Groppo et al., 2014).

In (Zhao et al., 2021), kurtosis-related parameters, especially MK, showed to sensitively reflect the brain maturity of premature infants. Decreased MK values were registered in the preterm cohort due to the decreased density of cells and axon membranes associated with impaired brain development.

Similarly, NODDI model has been applied to investigate WM and GM maturation in the preterm brain (Batalle et al., 2017, 2019; Eaton-Rosen et al., 2015; Kimpton et al., 2021), finding that ICVF increases in the WM with increasing maturation, mainly attributed to increasing axonal growth/density/packing/diameter or pre-myelination/myelination changes, rather than changes in axon coherence or geometry. Moreover, greater ICVF in childhood has been associated with better neurodevelopmental outcomes, IQ (Kelly et al., 2016; Young et al., 2019), visual motor integration (Young et al., 2019), motor/behavioural/emotional scores (Kelly et al., 2016), language (Mürner-Lavanchy et al., 2018) and maths (Collins et al., 2019).

Finally, although not previously investigated in case of preterm subjects, fa parameter derived from FORECAST model falls among those measures exhibiting significant differences from preterm to term-born infants, presumably because it is the equivalent of the DTI FA yet far more sensitive to the underlying fiber microanatomy.

The second perspective from which we examined our cohort was an SVM-based approach aimed at a more individualized classification method to overcome shortcomings of group-wise investigations. The success of the SVM in assigning a preterm-born or control individual to the correct group, based on a single MR image, indicates that the distinct brain development of preterm-born individuals can be successfully identified by ML methods. Indeed, considering

the law sample size at disposal, much inferior than the number of features (i.e., image voxels), SVM classifier managed to handle the issue of overfitting and proved a good performance both on FA skeletonised image, on which its model was designed, and on the vast majority of non-FA measures. Specifically, together with FA from DTI, other scalar parameters derived from DKI, NODDI and FORECAST exhibited good scores in terms both of accuracy and, most importantly, of ROC - a more meaningful measure of classifier performance than accuracy because it does not bias on size of test or evaluation data. Along with good performance scores, the selected classifier also showed strong robustness (i.e. limited variability across folds), another important indicator for model evaluation, assessing its stability.

We then explored the relationship occurring between TBSS- and SVM- based methods, with a view to assessing the degree of overlap between the two survey methods. The observed negative Pearson's correlation finds its explanation in considering that we compared a significance map from voxel-wise statistics made up of thresholded p-values below 0.05 and the map of SVM weight vectors serving as ranking metric for measuring feature importance (Gaonkar and Davatzikos, 2013). As a result, those voxels exhibiting a lower p-value correspondingly have a high ranking in the SVM model, which brings to the observed inverse trend. Agreement between voxel features for the two methods is just partial, to reflect the fact that a discrepancy actually exists between the two kinds of approach in voting WM connections with discriminative ability. Indeed, as already explained in the Introduction to this work, ML approaches have been entered neuroimaging field precisely to try to improve data-driven extraction of knowledge about underlying biological correlates.

We are aware that both voxel-wise statistical methods and, in particular, ML approaches benefit from large quantities of data. Consequently, one further step could be extending the current dataset in order to further improve our findings and, possibly, introducing a stratification based on patient's diagnosis. Indeed, we hypothesise that greater potential of ML classification may be useful to distinguish specific patterns of WM tracts also between healthy and pathological subjects, not detectable with standard group-level methods. This is a possible interesting development of current investigation, which could further highlight benefit of ML-based approaches for neuroimaging. Another possible continuation of the current survey could include structural connectome of our population to study the brain functional maturation in preterm infants. Features extracted from connectomes could be used as input both for the ML and for mathematical models to identify differences at the level of functional connectivity between term/preterm or healthy/pathological subjects and to investigate whether certain features of functional connectivity in preterm infants have

predictive abilities on possible disorders in the long term. Moreover, given the multiplicity of microstructural measures considered, it would be informative also to apply a Canonical Correlation Approach (CCA) (Bilenko and Gallant, 2016), which focuses on finding linear combinations that account for the most correlation in multiple datasets. This would help to identify the inter-measure similarities among features typical of preterm birth.

Take-Home Message

Results gathered so far from this study revealed that an intramodal dMRI approach can be a valuable tool to distinguish preterm and term-born infants regardless of the specific diagnosis based on radiological findings. This differentiation is attained both through a classical group-level survey tool such as TBSS and through a state-of-the-art approach based on SVM classification achieving a high recognition rate. Furthermore, comparison of the two methods shows a discrete agreement in selecting most discriminating WM regions, mainly depending on the microstructural measure under consideration. Taken together, these findings suggest that exploiting undisputed advantage of combining a ML-based procedure with an intramodal HARDI approach can unparallelly supplement the understanding of biological mechanisms underlying preterm birth providing precious biomarkers of long-term developmental outcome. Further work should focus on investigating how well these results generalize to data across centers and on what kind of improvements are needed, if any, to reach the end goal of predicting, on an individual basis, the specific outcome of persons born preterm.

9.4   Final Take-Home Message

Current work compensed in this dissertation serves as a proof-of-concept to demonstrate that advanced dMRI microstructural models are feasible in a neonatal clinical setting, subject to an accurate and dedicated preprocessing framework, requiring careful adaptation of algorithms in use for adults and centered first of all on an efficient denoising, crucial to improve quality of diagnostic images. By solving the problems posed by the sub-optimality of data from the paediatric clinical environment, this work poses the basis for a wide adoption of advanced diffusion imaging methods in the clinical activity, not only regarding the infant brain but also regarding the SC district, where they had never been utilized before. Investigation of preterm birth faced in our surveys is only an example of how combination of high-field scanners,

beyond-DTI HARDI techniques, as well as ML-based analysis tools can give a relevant boost in further elucidating the plethora of perinatal SNC abnormalities.

References

Aja-Fernández, S., Vegas-Sánchez-Ferrero, G., and Tristán-Vega, A. (2014). Noise estimation in parallel mri: Grappa and sense. *Magnetic resonance imaging*, 32(3):281–290.

Alexander, A. L., Lee, J. E., Wu, Y.-C., and Field, A. S. (2006). Comparison of diffusion tensor imaging measurements at 3.0 t versus 1.5 t with and without parallel imaging. *Neuroimaging Clinics*, 16(2):299–309.

Alexander, B., Murray, A. L., Loh, W. Y., Matthews, L. G., Adamson, C., Beare, R., Chen, J., Kelly, C. E., Rees, S., Warfield, S. K., et al. (2017). A new neonatal cortical and subcortical brain atlas: the melbourne children's regional infant brain (m-crib) atlas. *NeuroImage*, 147:841–851.

Alexandrou, G., Mårtensson, G., Skiöld, B., Blennow, M., Ådén, U., and Vollmer, B. (2014). White matter microstructure is influenced by extremely preterm birth and neonatal respiratory factors. *Acta paediatrica*, 103(1):48–56.

Alizadeh, M., Fisher, J., Saksena, S., Sultan, Y., Conklin, C. J., Middleton, D. M., Finsterbusch, J., Krisa, L., Flanders, A. E., Faro, S. H., et al. (2018). Reduced field of view diffusion tensor imaging and fiber tractography of the pediatric cervical and thoracic spinal cord injury. *Journal of neurotrauma*, 35(3):452–460.

Anderson, A. W. (2005). Measurement of fiber orientation distributions using high angular resolution diffusion imaging. *Magnetic Resonance in Medicine: An Official Journal of the International Society for Magnetic Resonance in Medicine*, 54(5):1194–1206.

Andre, J. B. and Bammer, R. (2010). Advanced diffusion-weighted magnetic resonance imaging techniques of the human spinal cord. *Topics in magnetic resonance imaging: TMRI*, 21(6):367.

Anjari, M., Srinivasan, L., Allsop, J. M., Hajnal, J. V., Rutherford, M. A., Edwards, A. D., and Counsell, S. J. (2007). Diffusion tensor imaging with tract-based spatial statistics reveals local white matter abnormalities in preterm infants. *Neuroimage*, 35(3):1021–1027.

Antherieu, P., Levy, R., De Saint Denis, T., Lohkamp, L., Paternoster, G., Di Rocco, F., Boddaert, N., and Zerah, M. (2019). Diffusion tensor imaging (dti) and tractography of the spinal cord in pediatric population with spinal lipomas: preliminary study. *Child's Nervous System*, 35(1):129–137.

Arab, A., Wojna-Pelczar, A., Khairnar, A., Szabó, N., and Ruda-Kucerova, J. (2018). Principles of diffusion kurtosis imaging and its role in early diagnosis of neurodegenerative disorders. *Brain research bulletin*, 139:91–98.

Arthurs, O. J., Edwards, A., Austin, T., Graves, M. J., and Lomas, D. J. (2012). The challenges of neonatal magnetic resonance imaging. *Pediatric radiology*, 42(10):1183–1194.

Assaf, Y. and Basser, P. J. (2005). Composite hindered and restricted model of diffusion (charmed) mr imaging of the human brain. *Neuroimage*, 27(1):48–58.

Atkinson, J. and Braddick, O. (2007). Visual and visuocognitive development in children born very prematurely. *Progress in brain research*, 164:123–149.

Bach, M., Laun, F. B., Leemans, A., Tax, C. M., Biessels, G. J., Stieltjes, B., and Maier-Hein, K. H. (2014). Methodological considerations on tract-based spatial statistics (tbss). *Neuroimage*, 100:358–369.

Baliyan, V., Das, C. J., Sharma, R., and Gupta, A. K. (2016). Diffusion weighted imaging: technique and applications. *World journal of radiology*, 8(9):785.

Ball, G., Aljabar, P., Nongena, P., Kennea, N., Gonzalez-Cinca, N., Falconer, S., Chew, A. T., Harper, N., Wurie, J., Rutherford, M. A., et al. (2017). Multimodal image analysis of clinical influences on preterm brain development. *Annals of neurology*, 82(2):233–246.

Ball, G., Counsell, S. J., Anjari, M., Merchant, N., Arichi, T., Doria, V., Rutherford, M. A., Edwards, A. D., Rueckert, D., and Boardman, J. P. (2010). An optimised tract-based spatial statistics protocol for neonates: applications to prematurity and chronic lung disease. *Neuroimage*, 53(1):94–102.

Ball, G., Srinivasan, L., Aljabar, P., Counsell, S. J., Durighel, G., Hajnal, J. V., Rutherford, M. A., and Edwards, A. D. (2013). Development of cortical microstructure in the preterm human brain. *Proceedings of the National Academy of Sciences*, 110(23):9541–9546.

Barkovich, M. J., Li, Y., Desikan, R. S., Barkovich, A. J., and Xu, D. (2019). Challenges in pediatric neuroimaging. *Neuroimage*, 185:793–801.

Barnett, M. L., Tusor, N., Ball, G., Chew, A., Falconer, S., Aljabar, P., Kimpton, J. A., Kennea, N., Rutherford, M., Edwards, A. D., et al. (2018). Exploring the multiple-hit hypothesis of preterm white matter damage using diffusion mri. *NeuroImage: Clinical*, 17:596–606.

Barth, M., Breuer, F., Koopmans, P. J., Norris, D. G., and Poser, B. A. (2016). Simultaneous multislice (sms) imaging techniques. *Magnetic resonance in medicine*, 75(1):63–81.

Basser, P. J., Mattiello, J., and LeBihan, D. (1994). Mr diffusion tensor spectroscopy and imaging. *Biophysical journal*, 66(1):259–267.

Bassi, L., Chew, A., Merchant, N., Ball, G., Ramenghi, L., Boardman, J., Allsop, J. M., Doria, V., Arichi, T., Mosca, F., et al. (2011). Diffusion tensor imaging in preterm infants with punctate white matter lesions. *Pediatric research*, 69(6):561–566.

Bassi, L., Ricci, D., Volzone, A., Allsop, J. M., Srinivasan, L., Pai, A., Ribes, C., Ramenghi, L. A., Mercuri, E., Mosca, F., et al. (2008). Probabilistic diffusion tractography of the optic radiations and visual function in preterm infants at term equivalent age. *Brain*, 131(2):573–582.

Batalle, D., Hughes, E. J., Zhang, H., Tournier, J.-D., Tusor, N., Aljabar, P., Wali, L., Alexander, D. C., Hajnal, J. V., Nosarti, C., et al. (2017). Early development of structural networks and the impact of prematurity on brain connectivity. *Neuroimage*, 149:379–392.

Batalle, D., O'Muircheartaigh, J., Makropoulos, A., Kelly, C. J., Dimitrova, R., Hughes, E. J., Hajnal, J. V., Zhang, H., Alexander, D. C., Edwards, A. D., et al. (2019). Different patterns of cortical maturation before and after 38 weeks gestational age demonstrated by diffusion mri in vivo. *NeuroImage*, 185:764–775.

Beck, S., Wojdyla, D., Say, L., Betran, A. P., Merialdi, M., Requejo, J. H., Rubens, C., Menon, R., and Van Look, P. F. (2010). The worldwide incidence of preterm birth: a systematic review of maternal mortality and morbidity. *Bulletin of the World Health Organization*, 88:31–38.

Beebe, D. S., Tran, P., Bragg, M., Stillman, A., Truwitt, C., and Belani, K. G. (2000). Trained nurses can provide safe and effective sedation for mri in pediatric patients. *Canadian journal of anaesthesia*, 47(3):205–210.

Bester, M., Sigmund, E., Tabesh, A., Jaggi, H., Inglese, M., and Mitnick, R. (2010). Diffusional kurtosis imaging of the cervical spinal cord in multiple sclerosis patients. In *Proceedings of the 2010 Annual Meeting of ISMRM. Stockholm, Sweden*.

Bhutta, A. T., Cleves, M. A., Casey, P. H., Cradock, M. M., and Anand, K. J. (2002). Cognitive and behavioral outcomes of school-aged children who were born preterm: a meta-analysis. *Jama*, 288(6):728–737.

Bilenko, N. Y. and Gallant, J. L. (2016). Pyrcca: regularized kernel canonical correlation analysis in python and its applications to neuroimaging. *Frontiers in neuroinformatics*, 10:49.

Blencowe, H., Cousens, S., Chou, D., Oestergaard, M., Say, L., Moller, A.-B., Kinney, M., and Lawn, J. (2013). Born too soon: the global epidemiology of 15 million preterm births. *Reproductive health*, 10(1):1–14.

Blesa, M., Galdi, P., Cox, S. R., Sullivan, G., Stoye, D. Q., Lamb, G. J., Quigley, A. J., Thrippleton, M. J., Escudero, J., Bastin, M. E., et al. (2021). Hierarchical complexity of the macro-scale neonatal brain. *Cerebral Cortex*, 31(4):2071–2084.

Blesa, M., Sullivan, G., Anblagan, D., Telford, E. J., Quigley, A. J., Sparrow, S. A., Serag, A., Semple, S. I., Bastin, M. E., and Boardman, J. P. (2019). Early breast milk exposure modifies brain connectivity in preterm infants. *Neuroimage*, 184:431–439.

Braga, R. M., Roze, E., Ball, G., Merchant, N., Tusor, N., Arichi, T., Edwards, D., Rueckert, D., and Counsell, S. J. (2015). Development of the corticospinal and callosal tracts from extremely premature birth up to 2 years of age. *PLoS One*, 10(5):e0125681.

By, S., Xu, J., Box, B. A., Bagnato, F. R., and Smith, S. A. (2017). Application and evaluation of noddi in the cervical spinal cord of multiple sclerosis patients. *NeuroImage: Clinical*, 15:333–342.

Chen, G., Wu, Y., Shen, D., and Yap, P.-T. (2019). Noise reduction in diffusion mri using non-local self-similar information in joint x- q space. *Medical image analysis*, 53:79–94.

Cheong, J., Thompson, D., Wang, H., Hunt, R., Anderson, P., Inder, T. E., and Doyle, L. (2009). Abnormal white matter signal on mr imaging is related to abnormal tissue microstructure. *American Journal of Neuroradiology*, 30(3):623–628.

Chin, R., You, A. X., Meng, F., Zhou, J., and Sim, K. (2018). Recognition of schizophrenia with regularized support vector machine and sequential region of interest selection using structural magnetic resonance imaging. *Scientific Reports*, 8(1):1–10.

Choi, S., Cunningham, D. T., Aguila, F., Corrigan, J. D., Bogner, J., Mysiw, W. J., Knopp, M. V., and Schmalbrock, P. (2011). Dti at 7 and 3 t: systematic comparison of snr and its influence on quantitative metrics. *Magnetic resonance imaging*, 29(6):739–751.

Chu, C., Lagercrantz, H., Forssberg, H., and Nagy, Z. (2015). Investigating the use of support vector machine classification on structural brain images of preterm–born teenagers as a biological marker. *Plos one*, 10(4):e0123108.

Chung, A. W., Seunarine, K. K., and Clark, C. A. (2016). Noddi reproducibility and variability with magnetic field strength: a comparison between 1.5 t and 3 t. *Human brain mapping*, 37(12):4550–4565.

Clark, C., Barker, G., and Tofts, P. (1999). An in vivo evaluation of the effects of local magnetic susceptibility-induced gradients on water diffusion measurements in human brain. *Journal of Magnetic Resonance*, 141(1):52–61.

Cohen, Y., Anaby, D., and Morozov, D. (2017). Diffusion mri of the spinal cord: from structural studies to pathology. *NMR in Biomedicine*, 30(3):e3592.

Collins, S. E., Spencer-Smith, M., Mürner-Lavanchy, I., Kelly, C. E., Pyman, P., Pascoe, L., Cheong, J., Doyle, L. W., Thompson, D. K., and Anderson, P. J. (2019). White matter microstructure correlates with mathematics but not word reading performance in 13-year-old children born very preterm and full-term. *NeuroImage: Clinical*, 24:101944.

Conklin, C. J., Middleton, D. M., Alizadeh, M., Finsterbusch, J., Raunig, D. L., Faro, S. H., Shah, P., Krisa, L., Sinko, R., Delalic, J. Z., et al. (2016). Spatially selective 2d rf inner field of view (ifov) diffusion kurtosis imaging (dki) of the pediatric spinal cord. *NeuroImage: Clinical*, 11:61–67.

Conklin, J., Winter, J. D., Thompson, R. T., and Gelman, N. (2008). High-contrast 3d neonatal brain imaging with combined t1-and t2-weighted mp-rage. *Magnetic Resonance in Medicine: An Official Journal of the International Society for Magnetic Resonance in Medicine*, 59(5):1190–1196.

Counsell, S. J., Allsop, J. M., Harrison, M. C., Larkman, D. J., Kennea, N. L., Kapellou, O., Cowan, F. M., Hajnal, J. V., Edwards, A. D., and Rutherford, M. A. (2003). Diffusion-weighted imaging of the brain in preterm infants with focal and diffuse white matter abnormality. *Pediatrics*, 112(1):1–7.

Counsell, S. J., Edwards, A. D., Chew, A. T., Anjari, M., Dyet, L. E., Srinivasan, L., Boardman, J. P., Allsop, J. M., Hajnal, J. V., Rutherford, M. A., et al. (2008). Specific relations between neurodevelopmental abilities and white matter microstructure in children born preterm. *Brain*, 131(12):3201–3208.

Counsell, S. J., Maalouf, E. F., Fletcher, A. M., Duggan, P., Battin, M., Lewis, H. J., Herlihy, A. H., Edwards, A. D., Bydder, G. M., and Rutherford, M. A. (2002). Mr imaging assessment of myelination in the very preterm brain. *American journal of neuroradiology*, 23(5):872–881.

Daducci, A., Canales-Rodrı, E. J., Descoteaux, M., Garyfallidis, E., Gur, Y., Lin, Y.-C., Mani, M., Merlet, S., Paquette, M., Ramirez-Manzanares, A., et al. (2013). Quantitative comparison of reconstruction methods for intra-voxel fiber recovery from diffusion mri. *IEEE transactions on medical imaging*, 33(2):384–399.

Daducci, A., Canales-Rodríguez, E. J., Zhang, H., Dyrby, T. B., Alexander, D. C., and Thiran, J.-P. (2015). Accelerated microstructure imaging via convex optimization (amico) from diffusion mri data. *Neuroimage*, 105:32–44.

Dagia, C. and Ditchfield, M. (2008). 3 t mri in paediatrics: challenges and clinical applications. *European journal of radiology*, 68(2):309–319.

Dalal, P. G., Murray, D., Cox, T., McAllister, J., and Snider, R. (2006). Sedation and anesthesia protocols used for magnetic resonance imaging studies in infants: provider and pharmacologic considerations. *Anesthesia & Analgesia*, 103(4):863–868.

Davatzikos, C. (2019). Machine learning in neuroimaging: Progress and challenges. *Neuroimage*, 197:652.

de Bruïne, F. T., van Wezel-Meijler, G., Leijser, L. M., van den Berg-Huysmans, A. A., van Steenis, A., van Buchem, M. A., and van der Grond, J. (2011). Tractography of developing white matter of the internal capsule and corpus callosum in very preterm infants. *European radiology*, 21(3):538–547.

De Leener, B., Fonov, V. S., Collins, D. L., Callot, V., Stikov, N., and Cohen-Adad, J. (2018). Pam50: Unbiased multimodal template of the brainstem and spinal cord aligned with the icbm152 space. *Neuroimage*, 165:170–179.

De Leener, B., Kadoury, S., and Cohen-Adad, J. (2014). Robust, accurate and fast automatic segmentation of the spinal cord. *Neuroimage*, 98:528–536.

De Leener, B., Lévy, S., Dupont, S. M., Fonov, V. S., Stikov, N., Collins, D. L., Callot, V., and Cohen-Adad, J. (2017a). Sct: Spinal cord toolbox, an open-source software for processing spinal cord mri data. *Neuroimage*, 145:24–43.

De Leener, B., Mangeat, G., Dupont, S., Martin, A. R., Callot, V., Stikov, N., Fehlings, M. G., and Cohen-Adad, J. (2017b). Topologically preserving straightening of spinal cord mri. *Journal of Magnetic Resonance Imaging*, 46(4):1209–1219.

Dean, D., Planalp, E., Wooten, W., Adluru, N., Kecskemeti, S., Frye, C., Schmidt, C., Schmidt, N., Styner, M., Goldsmith, H., et al. (2017). Mapping white matter microstructure in the one month human brain. *Scientific reports*, 7(1):1–14.

Descoteaux, M. (1999). High angular resolution diffusion imaging (hardi). *Wiley encyclopedia of electrical and electronics engineering*, pages 1–25.

Desikan, R. S., Ségonne, F., Fischl, B., Quinn, B. T., Dickerson, B. C., Blacker, D., Buckner, R. L., Dale, A. M., Maguire, R. P., Hyman, B. T., et al. (2006). An automated labeling system for subdividing the human cerebral cortex on mri scans into gyral based regions of interest. *Neuroimage*, 31(3):968–980.

Dhollander, T., Mito, R., Raffelt, D., and Connelly, A. (2019). Improved white matter response function estimation for 3-tissue constrained spherical deconvolution. In *Proc. Intl. Soc. Mag. Reson. Med*, volume 555.

Dhollander, T., Raffelt, D., and Connelly, A. (2016). Unsupervised 3-tissue response function estimation from single-shell or multi-shell diffusion mr data without a co-registered t1 image. In *ISMRM Workshop on Breaking the Barriers of Diffusion MRI*, volume 5. ISMRM.

Dhollander, T., Zanin, J., Nayagam, B. A., Rance, G., and Connelly, A. (2018). Feasibility and benefits of 3-tissue constrained spherical deconvolution for studying the brains of babies. In *Proceedings of the 26th annual meeting of the International Society of Magnetic Resonance in Medicine*, page 3077.

Dietrich, O., Raya, J. G., Reeder, S. B., Reiser, M. F., and Schoenberg, S. O. (2007). Measurement of signal-to-noise ratios in mr images: influence of multichannel coils, parallel imaging, and reconstruction filters. *Journal of Magnetic Resonance Imaging: An Official Journal of the International Society for Magnetic Resonance in Medicine*, 26(2):375–385.

Doshi, J., Erus, G., Ou, Y., Gaonkar, B., and Davatzikos, C. (2013). Multi-atlas skull-stripping. *Academic radiology*, 20(12):1566–1576.

Dubois, J., Adibpour, P., Poupon, C., Hertz-Pannier, L., and Dehaene-Lambertz, G. (2016). Mri and m/eeg studies of the white matter development in human fetuses and infants: review and opinion. *Brain Plasticity*, 2(1):49–69.

Dubois, J., Alison, M., Counsell, S. J., Hertz-Pannier, L., Hüppi, P. S., and Benders, M. J. (2021). Mri of the neonatal brain: a review of methodological challenges and neuroscientific advances. *Journal of Magnetic Resonance Imaging*, 53(5):1318–1343.

Dubois, J., Dehaene-Lambertz, G., Kulikova, S., Poupon, C., Hüppi, P. S., and Hertz-Pannier, L. (2014). The early development of brain white matter: a review of imaging studies in fetuses, newborns and infants. *Neuroscience*, 276:48–71.

Dubois, J., Dehaene-Lambertz, G., Perrin, M., Mangin, J.-F., Cointepas, Y., Duchesnay, E., Le Bihan, D., and Hertz-Pannier, L. (2008). Asynchrony of the early maturation of white matter bundles in healthy infants: quantitative landmarks revealed noninvasively by diffusion tensor imaging. *Human brain mapping*, 29(1):14–27.

Duerden, E., Foong, J., Chau, V., Branson, H., Poskitt, K., Grunau, R., Synnes, A., Zwicker, J., and Miller, S. (2015). Tract-based spatial statistics in preterm-born neonates predicts cognitive and motor outcomes at 18 months. *American Journal of Neuroradiology*, 36(8):1565–1571.

Dyet, L. E., Kennea, N., Counsell, S. J., Maalouf, E. F., Ajayi-Obe, M., Duggan, P. J., Harrison, M., Allsop, J. M., Hajnal, J., Herlihy, A. H., et al. (2006). Natural history of brain lesions in extremely preterm infants studied with serial magnetic resonance imaging from birth and neurodevelopmental assessment. *Pediatrics*, 118(2):536–548.

Eaton-Rosen, Z., Melbourne, A., Orasanu, E., Cardoso, M. J., Modat, M., Bainbridge, A., Kendall, G. S., Robertson, N. J., Marlow, N., and Ourselin, S. (2015). Longitudinal measurement of the developing grey matter in preterm subjects using multi-modal mri. *NeuroImage*, 111:580–589.

Edwards, A. D. and Arthurs, O. J. (2011). Paediatric mri under sedation: is it necessary? what is the evidence for the alternatives? *Pediatric radiology*, 41(11):1353–1364.

Fadnavis, S., Batson, J., and Garyfallidis, E. (2020). Patch2self: Denoising diffusion mri with self-supervised learning. *Advances in Neural Information Processing Systems*, 33:16293–16303.

Farquharson, S., Tournier, J.-D., Calamante, F., Fabinyi, G., Schneider-Kolsky, M., Jackson, G. D., and Connelly, A. (2013). White matter fiber tractography: why we need to move beyond dti. *Journal of neurosurgery*, 118(6):1367–1377.

Feng, L., Li, H., Oishi, K., Mishra, V., Song, L., Peng, Q., Ouyang, M., Wang, J., Slinger, M., Jeon, T., et al. (2019). Age-specific gray and white matter dti atlas for human brain at 33, 36 and 39 postmenstrual weeks. *Neuroimage*, 185:685–698.

Fieremans, E., Benitez, A., Jensen, J., Falangola, M., Tabesh, A., Deardorff, R., Spampinato, M., Babb, J., Novikov, D., Ferris, S., et al. (2013). Novel white matter tract integrity metrics sensitive to alzheimer disease progression. *American Journal of Neuroradiology*, 34(11):2105–2112.

Fieremans, E., Jensen, J. H., and Helpern, J. A. (2011). White matter characterization with diffusional kurtosis imaging. *Neuroimage*, 58(1):177–188.

Finsterbusch, J. (2009). High-resolution diffusion tensor imaging with inner field-of-view epi. *Journal of Magnetic Resonance Imaging: An Official Journal of the International Society for Magnetic Resonance in Medicine*, 29(4):987–993.

Fischl, B. (2012). Freesurfer. *Neuroimage*, 62(2):774–781.

Fruehwald-Pallamar, J., Szomolanyi, P., Fakhrai, N., Lunzer, A., Weber, M., Thurnher, M., Pallamar, M., Trattnig, S., Prayer, D., and Noebauer-Huhmann, I. (2012). Parallel imaging of the cervical spine at 3t: optimized trade-off between speed and image quality. *American Journal of Neuroradiology*, 33(10):1867–1874.

Fujiwara, S., Uhrig, L., Amadon, A., Jarraya, B., and Le Bihan, D. (2014). Quantification of iron in the non-human primate brain with diffusion-weighted magnetic resonance imaging. *Neuroimage*, 102:789–797.

Fushimi, Y., Miki, Y., Okada, T., Yamamoto, A., Mori, N., Hanakawa, T., Urayama, S.-i., Aso, T., Fukuyama, H., Kikuta, K.-i., et al. (2007). Fractional anisotropy and mean diffusivity: Comparison between 3.0-t and 1.5-t diffusion tensor imaging with parallel imaging using

histogram and region of interest analysis. *NMR in Biomedicine: An International Journal Devoted to the Development and Application of Magnetic Resonance In vivo*, 20(8):743–748.

Galdi, P., Blesa, M., Stoye, D. Q., Sullivan, G., Lamb, G. J., Quigley, A. J., Thrippleton, M. J., Bastin, M. E., and Boardman, J. P. (2020). Neonatal morphometric similarity mapping for predicting brain age and characterizing neuroanatomic variation associated with preterm birth. *NeuroImage: Clinical*, 25:102195.

Gaonkar, B. and Davatzikos, C. (2013). Analytic estimation of statistical significance maps for support vector machine based multi-variate image analysis and classification. *Neuroimage*, 78:270–283.

Garyfallidis, E., Brett, M., Amirbekian, B., Rokem, A., Van Der Walt, S., Descoteaux, M., and Nimmo-Smith, I. (2014). Dipy, a library for the analysis of diffusion mri data. *Frontiers in neuroinformatics*, 8:8.

Gelman, N., Gorell, J. M., Barker, P. B., Savage, R. M., Spickler, E. M., Windham, J. P., and Knight, R. A. (1999). Mr imaging of human brain at 3.0 t: preliminary report on transverse relaxation rates and relation to estimated iron content. *Radiology*, 210(3):759–767.

Glenn, G. R., Helpern, J. A., Tabesh, A., and Jensen, J. H. (2015a). Optimization of white matter fiber tractography with diffusional kurtosis imaging. *NMR in Biomedicine*, 28(10):1245–1256.

Glenn, G. R., Helpern, J. A., Tabesh, A., and Jensen, J. H. (2015b). Quantitative assessment of diffusional kurtosis anisotropy. *NMR in Biomedicine*, 28(4):448–459.

Glenn, G. R., Kuo, L.-W., Chao, Y.-P., Lee, C.-Y., Helpern, J. A., and Jensen, J. H. (2016). Mapping the orientation of white matter fiber bundles: a comparative study of diffusion tensor imaging, diffusional kurtosis imaging, and diffusion spectrum imaging. *American Journal of Neuroradiology*, 37(7):1216–1222.

Glenn, G. R., Tabesh, A., and Jensen, J. H. (2015c). A simple noise correction scheme for diffusional kurtosis imaging. *Magnetic resonance imaging*, 33(1):124–133.

Gnanalingham, M., Irving, V., and Shaw, N. (2005). Consensus on neonatal infusion pumps and pressure monitoring. *Archives of Disease in Childhood-Fetal and Neonatal Edition*, 90(1):F93–F93.

Golland, P., Fischl, B., Spiridon, M., Kanwisher, N., Buckner, R. L., Shenton, M. E., Kikinis, R., Dale, A., and Grimson, W. E. L. (2002). Discriminative analysis for image-based studies. In *International Conference on Medical Image Computing and Computer-Assisted Intervention*, pages 508–515. Springer.

Griswold, M. A., Jakob, P. M., Heidemann, R. M., Nittka, M., Jellus, V., Wang, J., Kiefer, B., and Haase, A. (2002). Generalized autocalibrating partially parallel acquisitions (grappa). *Magnetic Resonance in Medicine: An Official Journal of the International Society for Magnetic Resonance in Medicine*, 47(6):1202–1210.

Groppo, M., Ricci, D., Bassi, L., Merchant, N., Doria, V., Arichi, T., Allsop, J. M., Ramenghi, L., Fox, M. J., Cowan, F. M., et al. (2014). Development of the optic radiations and visual function after premature birth. *Cortex*, 56:30–37.

Gros, C., De Leener, B., Badji, A., Maranzano, J., Eden, D., Dupont, S. M., Talbott, J., Zhuoquiong, R., Liu, Y., Granberg, T., et al. (2019). Automatic segmentation of the spinal cord and intramedullary multiple sclerosis lesions with convolutional neural networks. *Neuroimage*, 184:901–915.

Grossman, E. J., Ge, Y., Jensen, J. H., Babb, J. S., Miles, L., Reaume, J., Silver, J. M., Grossman, R. I., and Inglese, M. (2012). Thalamus and cognitive impairment in mild traumatic brain injury: a diffusional kurtosis imaging study. *Journal of neurotrauma*, 29(13):2318–2327.

Grussu, F., Schneider, T., Tur, C., Yates, R. L., Tachrount, M., Ianuş, A., Yiannakas, M. C., Newcombe, J., Zhang, H., Alexander, D. C., et al. (2017). Neurite dispersion: a new marker of multiple sclerosis spinal cord pathology? *Annals of clinical and translational neurology*, 4(9):663–679.

Hametner, S., Endmayr, V., Deistung, A., Palmrich, P., Prihoda, M., Haimburger, E., Menard, C., Feng, X., Haider, T., Leisser, M., et al. (2018). The influence of brain iron and myelin on magnetic susceptibility and effective transverse relaxation-a biochemical and histological validation study. *Neuroimage*, 179:117–133.

Hansen, B. (2019). An introduction to kurtosis fractional anisotropy. *American Journal of Neuroradiology*.

Hansen, B. and Jespersen, S. N. (2016). Kurtosis fractional anisotropy, its contrast and estimation by proxy. *Scientific reports*, 6(1):1–13.

Hansen, B. and Jespersen, S. N. (2017). Recent developments in fast kurtosis imaging. *Frontiers in Physics*, 5:40.

Hansen, B., Lund, T. E., Sangill, R., and Jespersen, S. N. (2013). Experimentally and computationally fast method for estimation of a mean kurtosis. *Magnetic resonance in medicine*, 69(6):1754–1760.

Hansen, B., Shemesh, N., and Jespersen, S. N. (2016). Fast imaging of mean, axial and radial diffusion kurtosis. *Neuroimage*, 142:381–393.

Heidemann, R. M., Porter, D. A., Anwander, A., Feiweier, T., Heberlein, K., Knösche, T. R., and Turner, R. (2010). Diffusion imaging in humans at 7t using readout-segmented epi and grappa. *Magnetic Resonance in Medicine*, 64(1):9–14.

Helle, M., Jerosch-Herold, M., Voges, I., Hart, C., Kramer, H.-H., and Rickers, C. (2011). Improved mri of the neonatal heart: feasibility study using a knee coil. *Pediatric radiology*, 41(11):1429–1432.

Henriques, R. N. (2012). *Diffusion kurtosis imaging of the healthy human brain*. PhD thesis.

Henriques, R. N., Correia, M. M., Marrale, M., Huber, E., Kruper, J., Koudoro, S., Yeatman, J. D., Garyfallidis, E., and Rokem, A. (2021a). Diffusional kurtosis imaging in the diffusion imaging in python project. *Frontiers in Human Neuroscience*, page 390.

Henriques, R. N., Correia, M. M., Nunes, R. G., and Ferreira, H. A. (2015). Exploring the 3d geometry of the diffusion kurtosis tensor—impact on the development of robust tractography procedures and novel biomarkers. *Neuroimage*, 111:85–99.

Henriques, R. N., Jespersen, S. N., Jones, D. K., and Veraart, J. (2021b). Toward more robust and reproducible diffusion kurtosis imaging. *Magnetic Resonance in Medicine*, 86(3):1600–1613.

Henriques, R. N., Jespersen, S. N., and Shemesh, N. (2019). Microscopic anisotropy misestimation in spherical-mean single diffusion encoding mri. *Magnetic resonance in medicine*, 81(5):3245–3261.

Hori, M., Fukunaga, I., Masutani, Y., Nakanishi, A., Shimoji, K., Kamagata, K., Asahi, K., Hamasaki, N., Suzuki, Y., and Aoki, S. (2012). New diffusion metrics for spondylotic myelopathy at an early clinical stage. *European radiology*, 22(8):1797–1802.

Hosseini, F., Ebrahimpourkomleh, H., and KhodamHazrati, M. (2015). Quantitative evaluation of skull stripping techniques on magnetic resonance images. In *World Congress on Electrical Engineering and Computer Systems and Science (EECSS 2015)*.

Hu, H. H. and McAllister, A. S. (2019). The potential and promise of diffusion tensor mri in predicting neurodevelopment in children.

Huber, E., Henriques, R. N., Owen, J. P., Rokem, A., and Yeatman, J. D. (2019). Applying microstructural models to understand the role of white matter in cognitive development. *Developmental Cognitive Neuroscience*, 36:100624.

Hughes, E., Cordero-Grande, L., Murgasova, M., Hutter, J., Price, A., Gomes, A. D. S., Allsop, J., Steinweg, J., Tusor, N., Wurie, J., et al. (2017a). The developing human connectome: announcing the first release of open access neonatal brain imaging. *Organization for Human Brain Mapp*, pages 25–29.

Hughes, E. J., Winchman, T., Padormo, F., Teixeira, R., Wurie, J., Sharma, M., Fox, M., Hutter, J., Cordero-Grande, L., Price, A. N., et al. (2017b). A dedicated neonatal brain imaging system. *Magnetic resonance in medicine*, 78(2):794–804.

Hui, E. S., Fieremans, E., Jensen, J. H., Tabesh, A., Feng, W., Bonilha, L., Spampinato, M. V., Adams, R., and Helpern, J. A. (2012). Stroke assessment with diffusional kurtosis imaging. *Stroke*, 43(11):2968–2973.

Hunsche, S., Moseley, M. E., Stoeter, P., and Hedehus, M. (2001). Diffusion-tensor mr imaging at 1.5 and 3.0 t: initial observations. *Radiology*, 221(2):550–556.

Hüppi, P. S., Maier, S. E., Peled, S., Zientara, G. P., Barnes, P. D., Jolesz, F. A., and Volpe, J. J. (1998a). Microstructural development of human newborn cerebral white matter assessed in vivo by diffusion tensor magnetic resonance imaging. *Pediatric research*, 44(4):584–590.

Hüppi, P. S., Warfield, S., Kikinis, R., Barnes, P. D., Zientara, G. P., Jolesz, F. A., Tsuji, M. K., and Volpe, J. J. (1998b). Quantitative magnetic resonance imaging of brain development in premature and mature newborns. *Annals of Neurology: Official Journal of the American Neurological Association and the Child Neurology Society*, 43(2):224–235.

Hutter, J., Tournier, J. D., Price, A. N., Cordero-Grande, L., Hughes, E. J., Malik, S., Steinweg, J., Bastiani, M., Sotiropoulos, S. N., Jbabdi, S., et al. (2018). Time-efficient and flexible design of optimized multishell hardi diffusion. *Magnetic resonance in medicine*, 79(3):1276–1292.

Iglesias, J. E., Liu, C.-Y., Thompson, P. M., and Tu, Z. (2011). Robust brain extraction across datasets and comparison with publicly available methods. *IEEE transactions on medical imaging*, 30(9):1617–1634.

Jelescu, I. O., Veraart, J., Adisetiyo, V., Milla, S. S., Novikov, D. S., and Fieremans, E. (2015). One diffusion acquisition and different white matter models: how does microstructure change in human early development based on wmti and noddi? *Neuroimage*, 107:242–256.

Jensen, J. H. and Helpern, J. A. (2010). Mri quantification of non-gaussian water diffusion by kurtosis analysis. *NMR in Biomedicine*, 23(7):698–710.

Jensen, J. H., Helpern, J. A., Ramani, A., Lu, H., and Kaczynski, K. (2005). Diffusional kurtosis imaging: the quantification of non-gaussian water diffusion by means of magnetic resonance imaging. *Magnetic Resonance in Medicine: An Official Journal of the International Society for Magnetic Resonance in Medicine*, 53(6):1432–1440.

Jensen, J. H., Helpern, J. A., and Tabesh, A. (2014). Leading non-gaussian corrections for diffusion orientation distribution function. *NMR in Biomedicine*, 27(2):202–211.

Jespersen, S. N., Kroenke, C. D., Østergaard, L., Ackerman, J. J., and Yablonskiy, D. A. (2007). Modeling dendrite density from magnetic resonance diffusion measurements. *Neuroimage*, 34(4):1473–1486.

Jeurissen, B., Leemans, A., Tournier, J.-D., Jones, D. K., and Sijbers, J. (2013). Investigating the prevalence of complex fiber configurations in white matter tissue with diffusion magnetic resonance imaging. *Human brain mapping*, 34(11):2747–2766.

Jeurissen, B., Tournier, J.-D., Dhollander, T., Connelly, A., and Sijbers, J. (2014). Multi-tissue constrained spherical deconvolution for improved analysis of multi-shell diffusion mri data. *NeuroImage*, 103:411–426.

Jones, D. K. and Cercignani, M. (2010). Twenty-five pitfalls in the analysis of diffusion mri data. *NMR in Biomedicine*, 23(7):803–820.

Jones, D. K., Horsfield, M. A., and Simmons, A. (1999). Optimal strategies for measuring diffusion in anisotropic systems by magnetic resonance imaging. *Magnetic Resonance in Medicine: An Official Journal of the International Society for Magnetic Resonance in Medicine*, 42(3):515–525.

Kaden, E., Kruggel, F., and Alexander, D. C. (2016). Quantitative mapping of the per-axon diffusion coefficients in brain white matter. *Magnetic resonance in medicine*, 75(4):1752–1763.

Karmacharya, S., Gagoski, B., Ning, L., Vyas, R., Cheng, H., Soul, J., Newberger, J., Shenton, M., Rathi, Y., and Grant, P. (2018). Advanced diffusion imaging for assessing normal white matter development in neonates and characterizing aberrant development in congenital heart disease. *NeuroImage: Clinical*, 19:360–373.

Kelly, C. E., Thompson, D. K., Chen, J., Leemans, A., Adamson, C. L., Inder, T. E., Cheong, J. L., Doyle, L. W., and Anderson, P. J. (2016). Axon density and axon orientation dispersion in children born preterm. *Human brain mapping*, 37(9):3080–3102.

Kersbergen, K. J., Leemans, A., Groenendaal, F., van der Aa, N. E., Viergever, M. A., de Vries, L. S., and Benders, M. J. (2014). Microstructural brain development between 30 and 40 weeks corrected age in a longitudinal cohort of extremely preterm infants. *Neuroimage*, 103:214–224.

Kimpton, J., Batalle, D., Barnett, M., Hughes, E., Chew, A., Falconer, S., Tournier, J., Alexander, D., Zhang, H., Edwards, A., et al. (2021). Diffusion magnetic resonance imaging assessment of regional white matter maturation in preterm neonates. *Neuroradiology*, 63(4):573–583.

Koay, C. G., Özarslan, E., and Pierpaoli, C. (2009). Probabilistic identification and estimation of noise (piesno): a self-consistent approach and its applications in mri. *Journal of magnetic resonance*, 199(1):94–103.

Kulikova, S., Hertz-Pannier, L., Dehaene-Lambertz, G., Buzmakov, A., Poupon, C., and Dubois, J. (2015). Multi-parametric evaluation of the white matter maturation. *Brain Structure and Function*, 220(6):3657–3672.

Kunz, N., Zhang, H., Vasung, L., O'Brien, K. R., Assaf, Y., Lazeyras, F., Alexander, D. C., and Hüppi, P. S. (2014). Assessing white matter microstructure of the newborn with multi-shell diffusion mri and biophysical compartment models. *Neuroimage*, 96:288–299.

Lampinen, B., Szczepankiewicz, F., Mårtensson, J., van Westen, D., Sundgren, P. C., and Nilsson, M. (2017). Neurite density imaging versus imaging of microscopic anisotropy in diffusion mri: a model comparison using spherical tensor encoding. *Neuroimage*, 147:517–531.

Lao, Z., Shen, D., Xue, Z., Karacali, B., Resnick, S. M., and Davatzikos, C. (2004). Morphological classification of brains via high-dimensional shape transformations and machine learning methods. *Neuroimage*, 21(1):46–57.

Lazar, M., Jensen, J. H., Xuan, L., and Helpern, J. A. (2008). Estimation of the orientation distribution function from diffusional kurtosis imaging. *Magnetic Resonance in Medicine: An Official Journal of the International Society for Magnetic Resonance in Medicine*, 60(4):774–781.

Le Bihan, D. and Breton, E. (1985). Imagerie de diffusion in-vivo par résonance magnétique nucléaire. *Comptes-Rendus de l'Académie des Sciences*, 93(5):27–34.

Le Bihan, D., Mangin, J.-F., Poupon, C., Clark, C. A., Pappata, S., Molko, N., and Chabriat, H. (2001). Diffusion tensor imaging: concepts and applications. *Journal of Magnetic Resonance Imaging: An Official Journal of the International Society for Magnetic Resonance in Medicine*, 13(4):534–546.

Lennartsson, F., Darekar, A., Maharatna, K., Konn, D., Allen, D., Tournier, J., Broulidakis, J., Vollmer, B., et al. (2018). Developing a framework for studying brain networks in neonatal hypoxic-ischemic encephalopathy. In *Annual Conference on Medical Image Understanding and Analysis*, pages 203–216. Springer.

Lévy, S., Benhamou, M., Naaman, C., Rainville, P., Callot, V., and Cohen-Adad, J. (2015). White matter atlas of the human spinal cord with estimation of partial volume effect. *Neuroimage*, 119:262–271.

Li, D. and Wang, X. (2017). Application value of diffusional kurtosis imaging (dki) in evaluating microstructural changes in the spinal cord of patients with early cervical spondylotic myelopathy. *Clinical Neurology and Neurosurgery*, 156:71–76.

Li, D. C., Malcolm, J. G., Rindler, R. S., Baum, G. R., Rao, A., Khurpad, S. N., Ahmad, F. U., et al. (2017a). The role of diffusion tensor imaging in spinal pathology: A review. *Neurology India*, 65(5):982.

Li, H.-x., Feng, X., Wang, Q., Dong, X., Yu, M., and Tu, W.-j. (2017b). Diffusion tensor imaging assesses white matter injury in neonates with hypoxic-ischemic encephalopathy. *Neural regeneration research*, 12(4):603.

Lin, L., Bhawana, R., Xue, Y., Duan, Q., Jiang, R., Chen, H., Chen, X., Sun, B., and Lin, H. (2018). Comparative analysis of diffusional kurtosis imaging, diffusion tensor imaging, and diffusion-weighted imaging in grading and assessing cellular proliferation of meningiomas. *American Journal of Neuroradiology*, 39(6):1032–1038.

Ling, X., Tang, W., Liu, G., Huang, L., Li, B., Li, X., Liu, S., and Xu, J. (2013). Assessment of brain maturation in the preterm infants using diffusion tensor imaging (dti) and enhanced t2 star weighted angiography (eswan). *European Journal of Radiology*, 82(9):e476–e483.

Liu, L., Oza, S., Hogan, D., Chu, Y., Perin, J., Zhu, J., Lawn, J. E., Cousens, S., Mathers, C., and Black, R. E. (2016). Global, regional, and national causes of under-5 mortality in 2000–15: an updated systematic analysis with implications for the sustainable development goals. *The Lancet*, 388(10063):3027–3035.

Ljungberg, E., Damestani, N. L., Wood, T. C., Lythgoe, D. J., Zelaya, F., Williams, S. C., Solana, A. B., Barker, G. J., and Wiesinger, F. (2021). Silent zero te mr neuroimaging: Current state-of-the-art and future directions. *Progress in Nuclear Magnetic Resonance Spectroscopy*, 123:73–93.

Lopez Rios, N., Foias, A., Lodygensky, G., Dehaes, M., and Cohen-Adad, J. (2018). Size-adaptable 13-channel receive array for brain mri in human neonates at 3 t. *NMR in Biomedicine*, 31(8):e3944.

Lu, H., Jensen, J. H., Ramani, A., and Helpern, J. A. (2006). Three-dimensional characterization of non-gaussian water diffusion in humans using diffusion kurtosis imaging. *NMR in Biomedicine: An International Journal Devoted to the Development and Application of Magnetic Resonance In vivo*, 19(2):236–247.

Ly, M. T., Nanavati, T. U., Frum, C. A., and Pergami, P. (2015). Comparing tract-based spatial statistics and manual region-of-interest labeling as diffusion analysis methods to detect white matter abnormalities in infants with hypoxic-ischemic encephalopathy. *Journal of Magnetic Resonance Imaging*, 42(6):1689–1697.

Malavolti, A. M., Chau, V., Brown-Lum, M., Poskitt, K. J., Brant, R., Synnes, A., Grunau, R. E., and Miller, S. P. (2017). Association between corpus callosum development on magnetic resonance imaging and diffusion tensor imaging, and neurodevelopmental outcome in neonates born very preterm. *Developmental Medicine & Child Neurology*, 59(4):433–440.

Malviya, S., Voepel-Lewis, T., Prochaska, G., and Tait, A. R. (2000). Prolonged recovery and delayed side effects of sedation for diagnostic imaging studies in children. *Pediatrics*, 105(3):e42–e42.

Marrale, M., Collura, G., Brai, M., Toschi, N., Midiri, F., La Tona, G., Lo Casto, A., and Gagliardo, C. (2016). Physics, techniques and review of neuroradiological applications of diffusion kurtosis imaging (dki). *Clinical neuroradiology*, 26(4):391–403.

McJury PhD, M. and Shellock PhD, F. G. (2000). Auditory noise associated with mr procedures: a review. *Journal of Magnetic Resonance Imaging*, 12(1):37–45.

Medicines and Agency, H. P. R. (2015). Safety guidelines for magnetic resonance imaging equipment in clinical use.

Mohamed, F. B., Hunter, L., Barakat, N., Liu, C.-S., Sair, H., Samdani, A., Betz, R., Faro, S., Gaughan, J., and Mulcahey, M. (2011). Diffusion tensor imaging of the pediatric spinal cord at 1.5 t: preliminary results. *American Journal of Neuroradiology*, 32(2):339–345.

Möller, H. E., Bossoni, L., Connor, J. R., Crichton, R. R., Does, M. D., Ward, R. J., Zecca, L., Zucca, F. A., and Ronen, I. (2019). Iron, myelin, and the brain: neuroimaging meets neurobiology. *Trends in neurosciences*, 42(6):384–401.

Mori, S., Oishi, K., Jiang, H., Jiang, L., Li, X., Akhter, K., Hua, K., Faria, A. V., Mahmood, A., Woods, R., et al. (2008). Stereotaxic white matter atlas based on diffusion tensor imaging in an icbm template. *Neuroimage*, 40(2):570–582.

Moser, M., Breger, R., Khatri, B., and Liu, Y. (2009). Comparison of 1.5 and 3.0 tesla mri diffusion tensor imaging (dti) in patients with multiple sclerosis. In *Proc Intl Soc Mag Reson Med*, volume 17, page 1155.

Mulcahey, M., Samdani, A., Gaughan, J., Barakat, N., Faro, S., Shah, P., Betz, R., and Mohamed, F. (2013). Diagnostic accuracy of diffusion tensor imaging for pediatric cervical spinal cord injury. *Spinal Cord*, 51(7):532–537.

Mürner-Lavanchy, I. M., Kelly, C. E., Reidy, N., Doyle, L. W., Lee, K. J., Inder, T., Thompson, D. K., Morgan, A. T., and Anderson, P. J. (2018). White matter microstructure is associated with language in children born very preterm. *NeuroImage: Clinical*, 20:808–822.

Næss-Schmidt, E. T., Blicher, J. U., Eskildsen, S. F., Tietze, A., Hansen, B., Stubbs, P. W., Jespersen, S., Østergaard, L., and Nielsen, J. F. (2017). Microstructural changes in the thalamus after mild traumatic brain injury: a longitudinal diffusion and mean kurtosis tensor mri study. *Brain injury*, 31(2):230–236.

Neto Henriques, R. (2018). *Advanced Methods for Diffusion MRI Data Analysis and their Application to the Healthy Ageing Brain*. PhD thesis, University of Cambridge.

Nilsson, M., Lätt, J., Ståhlberg, F., van Westen, D., and Hagslätt, H. (2012). The importance of axonal undulation in diffusion mr measurements: a monte carlo simulation study. *NMR in Biomedicine*, 25(5):795–805.

Nossin-Manor, R., Card, D., Morris, D., Noormohamed, S., Shroff, M. M., Whyte, H. E., Taylor, M. J., and Sled, J. G. (2013). Quantitative mri in the very preterm brain: assessing tissue organization and myelination using magnetization transfer, diffusion tensor and t1 imaging. *Neuroimage*, 64:505–516.

Nossin-Manor, R., Card, D., Raybaud, C., Taylor, M. J., and Sled, J. G. (2015). Cerebral maturation in the early preterm period—a magnetization transfer and diffusion tensor imaging study using voxel-based analysis. *Neuroimage*, 112:30–42.

Novikov, D. S., Kiselev, V. G., and Jespersen, S. N. (2018). On modeling. *Magnetic resonance in medicine*, 79(6):3172–3193.

Nunes, R., Hajnal, J., Golay, X., and Larkman, D. (2006). Simultaneous slice excitation and reconstruction for single shot epi. In *Proc Intl Soc Mag Reson Med*, volume 14, page 293.

Oishi, K., Faria, A. V., and Mori, S. (2012). Advanced neonatal neuromri. *Magnetic Resonance Imaging Clinics*, 20(1):81–91.

Oishi, K., Mori, S., Donohue, P. K., Ernst, T., Anderson, L., Buchthal, S., Faria, A., Jiang, H., Li, X., Miller, M. I., et al. (2011). Multi-contrast human neonatal brain atlas: application to normal neonate development analysis. *Neuroimage*, 56(1):8–20.

Ouyang, M., Dubois, J., Yu, Q., Mukherjee, P., and Huang, H. (2019a). Delineation of early brain development from fetuses to infants with diffusion mri and beyond. *Neuroimage*, 185:836–850.

Ouyang, M., Jeon, T., Sotiras, A., Peng, Q., Mishra, V., Halovanic, C., Chen, M., Chalak, L., Rollins, N., Roberts, T. P., et al. (2019b). Differential cortical microstructural maturation in the preterm human brain with diffusion kurtosis and tensor imaging. *Proceedings of the National Academy of Sciences*, 116(10):4681–4688.

Palombo, M., Gentili, S., Bozzali, M., Macaluso, E., and Capuani, S. (2015). New insight into the contrast in diffusional kurtosis images: Does it depend on magnetic susceptibility? *Magnetic resonance in medicine*, 73(5):2015–2024.

Panara, V., Navarra, R., Mattei, P., Piccirilli, E., Bartoletti, V., Uncini, A., and Caulo, M. (2019). Correlations between cervical spinal cord magnetic resonance diffusion tensor and diffusion kurtosis imaging metrics and motor performance in patients with chronic ischemic brain lesions of the corticospinal tract. *Neuroradiology*, 61(2):175–182.

Panara, V., Navarra, R., Mattei, P., Piccirilli, E., Cotroneo, A., Papinutto, N., Henry, R., Uncini, A., and Caulo, M. (2017). Spinal cord microstructure integrating phase-sensitive inversion recovery and diffusional kurtosis imaging. *Neuroradiology*, 59(8):819–827.

Pannek, K., Fripp, J., George, J. M., Fiori, S., Colditz, P. B., Boyd, R. N., and Rose, S. E. (2018). Fixel-based analysis reveals alterations is brain microstructure and macrostructure of preterm-born infants at term equivalent age. *NeuroImage: Clinical*, 18:51–59.

Papadakis, N. G., Xing, D., Huang, C. L.-H., Hall, L. D., and Carpenter, T. A. (1999). A comparative study of acquisition schemes for diffusion tensor imaging using mri. *Journal of Magnetic Resonance*, 137(1):67–82.

Paquette, M., Merlet, S., Gilbert, G., Deriche, R., and Descoteaux, M. (2015). Comparison of sampling strategies and sparsifying transforms to improve compressed sensing diffusion spectrum imaging. *Magnetic resonance in medicine*, 73(1):401–416.

Parodi, A., Malova, M., Cardiello, V., Raffa, S., Re, M., Calevo, M. G., Severino, M., Tortora, D., Morana, G., Rossi, A., et al. (2019). Punctate white matter lesions of preterm infants: Risk factor analysis. *European Journal of Paediatric Neurology*, 23(5):733–739.

Partridge, S. C., Mukherjee, P., Henry, R. G., Miller, S. P., Berman, J. I., Jin, H., Lu, Y., Glenn, O. A., Ferriero, D. M., Barkovich, A. J., et al. (2004). Diffusion tensor imaging: serial quantitation of white matter tract maturity in premature newborns. *Neuroimage*, 22(3):1302–1314.

Pecheva, D., Kelly, C., Kimpton, J., Bonthrone, A., Batalle, D., Zhang, H., and Counsell, S. (2018). Recent advances in diffusion neuroimaging: applications in the developing preterm brain. f1000res. *F1000FacultyRev-1326*.

Pietsch, M., Christiaens, D., Hutter, J., Cordero-Grande, L., Price, A. N., Hughes, E., Edwards, A. D., Hajnal, J. V., Counsell, S. J., and Tournier, J.-D. (2019). A framework for multi-component analysis of diffusion mri data over the neonatal period. *NeuroImage*, 186:321–337.

Pietsch, M. R. (2018). *Advanced diffusion MRI analysis methods for neonatal imaging*. PhD thesis, King's College London.

Polders, D. L., Leemans, A., Hendrikse, J., Donahue, M. J., Luijten, P. R., and Hoogduin, J. M. (2011). Signal to noise ratio and uncertainty in diffusion tensor imaging at 1.5, 3.0, and 7.0 tesla. *Journal of Magnetic Resonance Imaging*, 33(6):1456–1463.

Pruessmann, K. P., Weiger, M., Scheidegger, M. B., and Boesiger, P. (1999). Sense: sensitivity encoding for fast mri. *Magnetic Resonance in Medicine: An Official Journal of the International Society for Magnetic Resonance in Medicine*, 42(5):952–962.

Raz, E., Bester, M., Sigmund, E., Tabesh, A., Babb, J., Jaggi, H., Helpern, J., Mitnick, R., and Inglese, M. (2013). A better characterization of spinal cord damage in multiple sclerosis: a diffusional kurtosis imaging study. *American Journal of Neuroradiology*, 34(9):1846–1852.

Rodrigues, K. and Grant, P. E. (2011). Diffusion-weighted imaging in neonates. *Neuroimaging Clinics*, 21(1):127–151.

Rokem, A., Yeatman, J. D., Pestilli, F., Kay, K. N., Mezer, A., Van Der Walt, S., and Wandell, B. A. (2015). Evaluating the accuracy of diffusion mri models in white matter. *PloS one*, 10(4):e0123272.

Rudrapatna, S. U., Wieloch, T., Beirup, K., Ruscher, K., Mol, W., Yanev, P., Leemans, A., van der Toorn, A., and Dijkhuizen, R. M. (2014). Can diffusion kurtosis imaging improve the sensitivity and specificity of detecting microstructural alterations in brain tissue chronically after experimental stroke? comparisons with diffusion tensor imaging and histology. *Neuroimage*, 97:363–373.

Rufener, S., Ibrahim, M., and Parmar, H. A. (2011). Imaging of congenital spine and spinal cord malformations. *Neuroimaging Clinics*, 21(3):659–676.

Saha, S., Pagnozzi, A., Bourgeat, P., George, J. M., Bradford, D., Colditz, P. B., Boyd, R. N., Rose, S. E., Fripp, J., and Pannek, K. (2020). Predicting motor outcome in preterm infants from very early brain diffusion mri using a deep learning convolutional neural network (cnn) model. *Neuroimage*, 215:116807.

Sain, S. R. (1996). The nature of statistical learning theory.

Saksena, S., Alizadeh, M., Middleton, D. M., Conklin, C. J., Krisa, L., Flanders, A., Mulcahey, M., Mohamed, F. B., and Faro, S. H. (2018). Characterization of spinal cord diffusion tensor imaging metrics in clinically asymptomatic pediatric subjects with incidental congenital lesions. *Spinal Cord Series and Cases*, 4(1):1–7.

Saksena, S., Middleton, D., Krisa, L., Shah, P., Faro, S., Sinko, R., Gaughan, J., Finsterbusch, J., Mulcahey, M., and Mohamed, F. (2016). Diffusion tensor imaging of the normal cervical and thoracic pediatric spinal cord. *American Journal of Neuroradiology*, 37(11):2150–2157.

Schenck, J. F. (1996). The role of magnetic susceptibility in magnetic resonance imaging: Mri magnetic compatibility of the first and second kinds. *Medical physics*, 23(6):815–850.

Schilling, K. G., Fadnavis, S., Visagie, M., Garyfallidis, E., Landman, B. A., Smith, S. A., and O'Grady, K. P. (2021). Patch2self denoising of diffusion mri in the cervical spinal cord improves repeatability and feature conspicuity. In *International Society for Magnetic Resonance in Medicine Annual Meeting*.

Schneider, J., Fischer Fumeaux, C. J., Duerden, E. G., Guo, T., Foong, J., Graz, M. B., Hagmann, P., Chakravarty, M. M., Hüppi, P. S., Beauport, L., et al. (2018). Nutrient intake in the first two weeks of life and brain growth in preterm neonates. *Pediatrics*, 141(3).

Schölkopf, B., Smola, A. J., Bach, F., et al. (2002). *Learning with kernels: support vector machines, regularization, optimization, and beyond*. MIT press.

Shattuck, D. W. and Leahy, R. M. (2000). Brainsuite: An automated cortical surface identification tool. In *International Conference on Medical Image Computing and Computer-Assisted Intervention*, pages 50–61. Springer.

Shaw, C. B., Jensen, J. H., Deardorff, R. L., Spampinato, M. V., and Helpern, J. A. (2017). Comparison of diffusion metrics obtained at 1.5 t and 3t in human brain with diffusional kurtosis imaging. *Journal of Magnetic Resonance Imaging*, 45(3):673–680.

Shi, J., Chang, L., Wang, J., Zhang, S., Yao, Y., Zhang, S., Jiang, R., Guo, L., Guan, H., and Zhu, W. (2016). Initial application of diffusional kurtosis imaging in evaluating brain development of healthy preterm infants. *PLoS One*, 11(4):e0154146.

Singh, G., True, A. J., Lui, C. C., Prasanna, P., Orleans, G., Partyka, L., and Phatak, T. D. (2021). Normal anterior-posterior diameters of the spinal cord and spinal canal in healthy term newborns on sonography. *Pediatric Radiology*, 51(4):622–627.

Singhi, S., Tekes, A., Thurnher, M., Gilson, W. D., Izbudak, I., Thompson, C. B., and Huisman, T. A. (2012). Diffusion tensor imaging of the maturing paediatric cervical spinal cord: from the neonate to the young adult. *Journal of Neuroradiology*, 39(3):142–148.

Smith, R. E., Tournier, J.-D., Calamante, F., and Connelly, A. (2012). Anatomically-constrained tractography: improved diffusion mri streamlines tractography through effective use of anatomical information. *Neuroimage*, 62(3):1924–1938.

Smith, S. M. (2000). Bet: Brain extraction tool. *FMRIB TR00SMS2b, Oxford Centre for Functional Magnetic Resonance Imaging of the Brain), Department of Clinical Neurology, Oxford University, John Radcliffe Hospital, Headington, UK.*

Smith, S. M., Jenkinson, M., Johansen-Berg, H., Rueckert, D., Nichols, T. E., Mackay, C. E., Watkins, K. E., Ciccarelli, O., Cader, M. Z., Matthews, P. M., et al. (2006). Tract-based spatial statistics: voxelwise analysis of multi-subject diffusion data. *Neuroimage*, 31(4):1487–1505.

Soares, J., Marques, P., Alves, V., and Sousa, N. (2013). A hitchhiker's guide to diffusion tensor imaging. *Frontiers in neuroscience*, 7:31.

Sorantin, E., Robl, T., Lindbichler, F., and Riccabona, M. (2008). Mri of the neonatal and paediatric spine and spinal canal. *European journal of radiology*, 68(2):227–234.

Sotiropoulos, S. N., Jbabdi, S., Xu, J., Andersson, J. L., Moeller, S., Auerbach, E. J., Glasser, M. F., Hernandez, M., Sapiro, G., Jenkinson, M., et al. (2013). Advances in diffusion mri acquisition and processing in the human connectome project. *Neuroimage*, 80:125–143.

Spittle, A. J., Cheong, J., Doyle, L. W., Roberts, G., Lee, K. J., Lim, J., Hunt, R. W., Inder, T. E., and Anderson, P. J. (2011). Neonatal white matter abnormality predicts childhood motor impairment in very preterm children. *Developmental Medicine & Child Neurology*, 53(11):1000–1006.

St-Jean, S., Coupé, P., and Descoteaux, M. (2016). Non local spatial and angular matching: Enabling higher spatial resolution diffusion mri datasets through adaptive denoising. *Medical image analysis*, 32:115–130.

St-Jean, S., De Luca, A., Tax, C. M., Viergever, M. A., and Leemans, A. (2020). Automated characterization of noise distributions in diffusion mri data. *Medical Image Analysis*, 65:101758.

Staudt, M., Pavlova, M., Böhm, S., Grodd, W., and Krägeloh-Mann, I. (2003). Pyramidal tract damage correlates with motor dysfunction in bilateral periventricular leukomalacia (pvl). *Neuropediatrics*, 34(04):182–188.

Stejskal, E. O. and Tanner, J. E. (1965). Spin diffusion measurements: spin echoes in the presence of a time-dependent field gradient. *The journal of chemical physics*, 42(1):288–292.

Steven, A. J., Zhuo, J., and Melhem, E. R. (2014). Diffusion kurtosis imaging: an emerging technique for evaluating the microstructural environment of the brain. *American journal of roentgenology*, 202(1):W26–W33.

Stokowski, L. A. (2005). Ensuring safety for infants undergoing magnetic resonance imaging. *Advances in Neonatal Care*, 5(1):14–27.

Storey, P., Frigo, F. J., Hinks, R. S., Mock, B. J., Collick, B. D., Baker, N., Marmurek, J., and Graham, S. J. (2007). Partial k-space reconstruction in single-shot diffusion-weighted echo-planar imaging. *Magnetic Resonance in Medicine: An Official Journal of the International Society for Magnetic Resonance in Medicine*, 57(3):614–619.

Tabelow, K., Voss, H. U., and Polzehl, J. (2015). Local estimation of the noise level in mri using structural adaptation. *Medical image analysis*, 20(1):76–86.

Taber, K. H., Herrick, R. C., Weathers, S. W., Kumar, A. J., Schomer, D. F., and Hayman, L. A. (1998). Pitfalls and artifacts encountered in clinical mr imaging of the spine. *Radiographics*, 18(6):1499–1521.

Tabesh, A., Jensen, J. H., Ardekani, B. A., and Helpern, J. A. (2011). Estimation of tensors and tensor-derived measures in diffusional kurtosis imaging. *Magnetic resonance in medicine*, 65(3):823–836.

Tax, C. M., Otte, W. M., Viergever, M. A., Dijkhuizen, R. M., and Leemans, A. (2015). Rekindle: robust extraction of kurtosis indices with linear estimation. *Magnetic resonance in medicine*, 73(2):794–808.

Thaler, C., Kyselyova, A. A., Faizy, T. D., Nawka, M. T., Jespersen, S., Hansen, B., Stellmann, J.-P., Heesen, C., Stürner, K. H., Stark, M., et al. (2021). Heterogeneity of multiple sclerosis lesions in fast diffusional kurtosis imaging. *PloS one*, 16(2):e0245844.

Thompson, D. K., Inder, T. E., Faggian, N., Johnston, L., Warfield, S. K., Anderson, P. J., Doyle, L. W., and Egan, G. F. (2011). Characterization of the corpus callosum in very preterm and full-term infants utilizing mri. *Neuroimage*, 55(2):479–490.

Thompson, D. K., Kelly, C. E., Chen, J., Beare, R., Alexander, B., Seal, M. L., Lee, K., Matthews, L. G., Anderson, P. J., Doyle, L. W., et al. (2019). Early life predictors of brain development at term-equivalent age in infants born across the gestational age spectrum. *Neuroimage*, 185:813–824.

Tietze, A., Hansen, M., Østergaard, L., Jespersen, S., Sangill, R., Lund, T., Geneser, M., Hjelm, M., and Hansen, B. (2015). Mean diffusional kurtosis in patients with glioma: initial results with a fast imaging method in a clinical setting. *American journal of neuroradiology*, 36(8):1472–1478.

Timmers, I., Roebroeck, A., Bastiani, M., Jansma, B., Rubio-Gozalbo, E., and Zhang, H. (2016). Assessing microstructural substrates of white matter abnormalities: a comparative study using dti and noddi. *PloS one*, 11(12):e0167884.

Tokariev, M., Vuontela, V., Perkola, J., Lönnberg, P., Lano, A., Andersson, S., Metsäranta, M., and Carlson, S. (2020). A protocol for the analysis of dti data collected from young children. *MethodsX*, 7:100878.

Tournier, J., Calamante, F., and Connelly, A. (2009). How many diffusion gradient directions are required for hardi. In *Proc. ISMRM*, volume 358.

Tournier, J.-D., Calamante, F., and Connelly, A. (2007). Robust determination of the fibre orientation distribution in diffusion mri: non-negativity constrained super-resolved spherical deconvolution. *Neuroimage*, 35(4):1459–1472.

Tournier, J.-D., Calamante, F., Gadian, D. G., and Connelly, A. (2004). Direct estimation of the fiber orientation density function from diffusion-weighted mri data using spherical deconvolution. *Neuroimage*, 23(3):1176–1185.

Tournier, J.-D., Mori, S., and Leemans, A. (2011). Diffusion tensor imaging and beyond. *Magnetic resonance in medicine*, 65(6):1532.

Tournier, J.-D., Smith, R., Raffelt, D., Tabbara, R., Dhollander, T., Pietsch, M., Christiaens, D., Jeurissen, B., Yeh, C.-H., and Connelly, A. (2019). Mrtrix3: A fast, flexible and open software framework for medical image processing and visualisation. *Neuroimage*, 202:116137.

Tusor, N., Benders, M. J., Counsell, S. J., Nongena, P., Ederies, M. A., Falconer, S., Chew, A., Gonzalez-Cinca, N., Hajnal, J. V., Gangadharan, S., et al. (2017). Punctate white matter lesions associated with altered brain development and adverse motor outcome in preterm infants. *Scientific reports*, 7(1):1–9.

Tustison, N. J., Avants, B. B., Cook, P. A., Zheng, Y., Egan, A., Yushkevich, P. A., and Gee, J. C. (2010). N4itk: improved n3 bias correction. *IEEE transactions on medical imaging*, 29(6):1310–1320.

Tustison, N. J. et al. (2013). Explicit b-spline regularization in diffeomorphic image registration. *Frontiers in neuroinformatics*, 7:39.

Tymofiyeva, O., Hess, C. P., Ziv, E., Tian, N., Bonifacio, S. L., McQuillen, P. S., Ferriero, D. M., Barkovich, A. J., and Xu, D. (2012). Towards the "baby connectome": mapping the structural connectivity of the newborn brain. *PloS one*, 7(2):e31029.

Ullmann, E., Pelletier Paquette, J. F., Thong, W. E., and Cohen-Adad, J. (2014). Automatic labeling of vertebral levels using a robust template-based approach. *International journal of biomedical imaging*, 2014.

Van Braeckel, K. N. and Taylor, H. G. (2013). Visuospatial and visuomotor deficits in preterm children: the involvement of cerebellar dysfunctioning. *Developmental Medicine & Child Neurology*, 55:19–22.

Van Essen, D. C. and Ugurbil, K. (2012). The future of the human connectome. *Neuroimage*, 62(2):1299–1310.

van Pul, C., van Kooij, B. J., de Vries, L. S., Benders, M. J., Vilanova, A., and Groenendaal, F. (2012). Quantitative fiber tracking in the corpus callosum and internal capsule reveals microstructural abnormalities in preterm infants at term-equivalent age. *American journal of neuroradiology*, 33(4):678–684.

Vapnik, V. N. (1999). An overview of statistical learning theory. *IEEE transactions on neural networks*, 10(5):988–999.

Vargas, M., Boto, J., and Meling, T. (2021). Imaging of the spine and spinal cord: an overview of magnetic resonance imaging (mri) techniques. *Revue neurologique*, 177(5):451–458.

Vargas, M., Delattre, B., Boto, J., Gariani, J., Dhouib, A., Fitsiori, A., and Dietemann, J. (2018). Advanced magnetic resonance imaging (mri) techniques of the spine and spinal cord in children and adults. *Insights into imaging*, 9(4):549–557.

Vedantam, A., Jirjis, M. B., Schmit, B. D., Wang, M. C., Ulmer, J. L., and Kurpad, S. N. (2014). Diffusion tensor imaging of the spinal cord: insights from animal and human studies. *Neurosurgery*, 74(1):1–8.

Veraart, J., Novikov, D. S., Christiaens, D., Ades-Aron, B., Sijbers, J., and Fieremans, E. (2016). Denoising of diffusion mri using random matrix theory. *Neuroimage*, 142:394–406.

Volpe, J. J. (2003). Cerebral white matter injury of the premature infant—more common than you think. *Pediatrics*, 112(1):176–180.

Volpe, J. J. (2009). Brain injury in premature infants: a complex amalgam of destructive and developmental disturbances. *The Lancet Neurology*, 8(1):110–124.

Volpe, J. J., Inder, T. E., Darras, B. T., de Vries, L. S., du Plessis, A. J., Neil, J., and Perlman, J. M. (2017). *Volpe's neurology of the newborn e-book*. Elsevier Health Sciences.

Waldron, S. and MacKinnon, R. (2007). Neonatal thermoregulation. *Infant*, 3(3):101–104.

Walker, L., Gozzi, M., Lenroot, R., Thurm, A., Behseta, B., Swedo, S., and Pierpaoli, C. (2012). Diffusion tensor imaging in young children with autism: biological effects and potential confounds. *Biological psychiatry*, 72(12):1043–1051.

Wang, H., Suh, J. W., Das, S. R., Pluta, J. B., Craige, C., and Yushkevich, P. A. (2012). Multi-atlas segmentation with joint label fusion. *IEEE transactions on pattern analysis and machine intelligence*, 35(3):611–623.

Wang, K., Wang, W.-T., Wang, J., Chen, Z., Song, Q.-X., Chen, S.-Y., Hao, Q., He, D.-W., and Shen, H.-X. (2016). Compared study of routine magnetic resonance imaging and diffusion tensor tractography on the predictive value of diagnosis and prognosis in acute cervical spinal cord injury. *Journal of Acute Disease*, 5(4):328–332.

Wang, Z., Lin, J. C., Mao, W., Liu, W., Smith, M. B., and Collins, C. M. (2007). Sar and temperature: simulations and comparison to regulatory limits for mri. *Journal of Magnetic Resonance Imaging: An Official Journal of the International Society for Magnetic Resonance in Medicine*, 26(2):437–441.

Warach, S., Chien, D., Li, W., Ronthal, M., and Edelman, R. (1992). Fast magnetic resonance diffusion-weighted imaging of acute human stroke. *Neurology*, 42(9):1717–1717.

Whitwell, J. L. (2009). Voxel-based morphometry: an automated technique for assessing structural changes in the brain. *Journal of Neuroscience*, 29(31):9661–9664.

Wilm, B. J., Svensson, J., Henning, A., Pruessmann, K. P., Boesiger, P., and Kollias, S. S. (2007). Reduced field-of-view mri using outer volume suppression for spinal cord diffusion imaging. *Magnetic Resonance in Medicine: An Official Journal of the International Society for Magnetic Resonance in Medicine*, 57(3):625–630.

Wu, E. X. and Cheung, M. M. (2010). Mr diffusion kurtosis imaging for neural tissue characterization. *NMR in Biomedicine*, 23(7):836–848.

WU-Minn, H. (2017). 1200 subjects data release reference manual. *URL https://www. humanconnectome. org*.

Xie, S., Zuo, N., Shang, L., Song, M., Fan, L., and Jiang, T. (2015). How does b-value affect hardi reconstruction using clinical diffusion mri data? *PloS one*, 10(3):e0120773.

Xu, J., Shimony, J. S., Klawiter, E. C., Snyder, A. Z., Trinkaus, K., Naismith, R. T., Benzinger, T. L., Cross, A. H., and Song, S.-K. (2013). Improved in vivo diffusion tensor imaging of human cervical spinal cord. *Neuroimage*, 67:64–76.

Yoshida, S., Oishi, K., Faria, A. V., and Mori, S. (2013). Diffusion tensor imaging of normal brain development. *Pediatric radiology*, 43(1):15–27.

Young, J. M., Vandewouw, M. M., Mossad, S. I., Morgan, B. R., Lee, W., Smith, M. L., Sled, J. G., and Taylor, M. J. (2019). White matter microstructural differences identified using multi-shell diffusion imaging in six-year-old children born very preterm. *NeuroImage: Clinical*, 23:101855.

Zanin, E., Ranjeva, J., Confort-Gouny, S., GUYE, M., DENIS, D., COZZONE, P., and GIRARD, N. (2010). White matter maturation of normal human fetal brain. an in vivo diffusion tensor imaging tractography study. In *Proc Intl Soc Mag Reson Med*, volume 18, page 2025.

Zhang, H., Schneider, T., Wheeler-Kingshott, C. A., and Alexander, D. C. (2012). Noddi: practical in vivo neurite orientation dispersion and density imaging of the human brain. *Neuroimage*, 61(4):1000–1016.

Zhao, X., Zhang, C., Zhang, B., Yan, J., Wang, K., Zhu, Z., and Zhang, X. (2021). The value of diffusion kurtosis imaging in detecting delayed brain development of premature infants.

Zhu, T., Peng, Q., Ouyang, A., and Huang, H. (2021). Neuroanatomical underpinning of diffusion kurtosis measurements in the cerebral cortex of healthy macaque brains. *Magnetic Resonance in Medicine*, 85(4):1895–1908.

Appendix A

Advanced Diffusion MRI microstructural models

A.1   Neurite Orientation Dispersion and Density imaging

NODDI (Zhang et al., 2012) is currently the most popular among biophysical models. It provides a sufficiently simple, yet complex enough model of diffusion MRI for estimating the key features of neurite morphology in vivo on clinical MRI scanners. This model facilitates mapping of neurite morphology and focuses on quantifying the altered architecture of these multifaceted structures.

The proposed technique enables such mapping by combining a three-compartment tissue model with a two-shell HARDI protocol optimized for clinical feasibility. Specifically, it separates the signal arising from intra-cellular compartment, extra-cellular compartment and CSF. Each of them affects water diffusion within the environment in a unique way and gives rise to a separate normalized MR signal.

Specifically, the intra-cellular compartment refers to the space bounded by the membrane of neurites. This space is modelled as a set of sticks, i.e., cylinders of zero radius, to capture the highly restricted nature of diffusion perpendicular to neurites and unhindered diffusion along the. The orientation distribution of sticks can range from highly parallel to highly dispersed. The extra-cellular compartment refers to the space around the neurites, which is occupied by various types of glial cells and, additionally in GM, cell bodies. In this space, the diffusion of water molecules is hindered by the presence of neurites but not restricted, hence is modeled with Gaussian anisotropic diffusion. The CSF compartment models the space occupied by cerebrospinal fluid and is modeled as isotropic Gaussian diffusion.

Furthermore, to characterize the microstructure within a voxel, NODDI uses three scalar

parameters: (i) Neurite Density Index (NDI), also called Intra Cellular Volume Fraction (ICVF), estimating the density of neurites; (ii) Orientation Dispersion Index (ODI), defined to characterize angular variation of neurites, reflecting the spatial configuration of the neurite structures; and (iii) free water fraction or Isotropic Volume Fraction (ISOVF), quantifying freely diffusing water from neural tissues with Gaussian diffusion.

The resulting indices of neurites have proven to relate more directly to and provide more specific markers of brain tissue microstructure than standard indices from DTI, such as FA. Specifically, NODDI provides sensible neurite density and orientation dispersion estimates, thereby disentangling two key contributing factors to FA and enabling the analysis of each factor individually.

The optimized protocol takes about 30 min to acquire, making it feasible for inclusion in a typical clinical setting. Nevertheless, sampling fewer orientations in each shell can reduce the acquisition time to just 10 min with minimal impact on the accuracy of the estimates. This demonstrates the feasibility of NODDI even for the most time-sensitive clinical applications, such as neonatal and dementia imaging.

By increasing specificity for certain clinically meaningful tissue properties, application of NODDI in clinical research has mostly reported promising results for improving patient stratification and prediction of neurological functions. In particular, given the key role neurite morphology covers in terms of brain development, NODDI has opened new opportunities for understanding neurodevelopment and disorders.

A.2   Multi-Shell Multi-Tissue Constrained Spherical Deconvolution

MSMT CSD (Jeurissen et al., 2014) is a specific extension of Spherical Deconvolution (SD) approach. SD is a particularly attractive HARDI method, which provides estimates of the full fODF in each brain voxel, regardless of the number of underlying fibre orientations (Tournier et al., 2004). It is based on the assumption that the dMRI signal originating from a single voxel (made up of different fibre populations) is given by the spherical convolution of the single response function (the dMRI signal profile for a typical fibre population) with the fODF (the apparent density of fibres as a function of orientation). The unknown represented by the fODF can thus be found by performing the deconvolution of the response function from the measured dMRI signal.

However, SD operation is inherently ill-posed and susceptible to noise. To sort this out,

CSD introduces a constraint to minimize the appearance of physically impossible negative values in the reconstructed fODF. With this constraint, it becomes possible to perform the SD operation with drastically reduced noise sensitivity, allowing reliable fODF estimates on clinically feasible dMRI data (Tournier et al., 2007).

Despite the improvements provided by CSD, significant challenges persist. First, CSD typically only supports data acquired with a single shell acquisition scheme -i.e., single constant diffusion weighting, despite multi-shell data becoming more and more prevalent in microstructural modelling. Furthermore, CSD can only provide high quality fODF estimates in voxels containing WM only. Conversely, in voxels including other tissue types such as GM and CSF, the WM response function may no longer be appropriate and SD produces unreliable, noisy fODF estimates.

To this end, MSMT CSD approach is conceived as an extension of CSD to support multi-shell dMRI data. Indeed, by exploiting the unique b value dependencies of the different tissue types, it can estimate a multi-tissue ODF. Moreover, as MSMT-CSD includes separate compartments for each tissue type, it can produce a map of the WM/GM/CSF volume fractions directly from the dMRI data, which can serve as new quantitative metrics. In addition, the more complete modelling of the dMRI signal results in more precise fibre orientation estimates at the tissue interfaces, resulting in more accurate fibre tracking in large parts of the brain compared to standard Single-Shell Single-Tissue CSD.

A.3 Fiber ORientation Estimated using Continuous Axially Symmetric Tensors

FORECAST (Anderson, 2005; Kaden et al., 2016) is a simple, axially symmetric model of diffusion in WM fibers used to relate diffusion measurements to fiber properties. This method represents a good trade-off between a conventional, single tensor model of diffusion and "model-free" high angular resolution methods.

This approach is based on the invariance property of diffusion signal: as long as the local structure is axially symmetric - which is typically the case in nerve tissue - for a fixed b value the spherical mean of the diffusion signal over the gradient directions does not depend on the axon orientation distribution. This allows to disentangle the intrinsic fiber diffusivity from the fiber orientation distribution and in turn to extract relevant markers of axon microgeometry unaffected by fiber dispersion and crossing, which are ubiquitous in brain WM. This translates in potentially improving the sensitivity and/or specificity to various neurological

conditions.

FORECAST models the single fiber response within each voxel with an axially symmetric tensor and exploits the mean of the signal to estimate the tensor parameters. Its associated scalar indices are the crossing invariant version of tensor indices: the parallel diffusivity (d_par), the perpendicular diffusivity (d_perp), the fractional anisotropy (fa) and the mean diffusivity (md) in each voxel.

These quantitative maps of the voxel-averaged diffusion coefficients can be estimated in a clinically feasible manner in vivo. Indeed, this method does not assume prior knowledge about fibers' orientation inside a voxel, neither normally requires complex gradient waveforms with multiple gradient pulses. It is instead able to recover microscopic diffusion anisotropy resorting to a widely available pulse sequence featuring moderate levels of diffusion weighting, which simplifies implementation and improves image quality compared to very high diffusion weighting methods.

Factoring out the effects due to fiber dispersion and crossing in human WM, this technique has proven to resolve crossing fibers better than other existing methods and also to address the problem of partial volume averaging in DTI, providing a basis for more reliable estimates of fiber orientation and fa. In contrast to DTI, it can discriminate changes in angular distribution ("coherence") from changes in fiber anisotropy, which potentially improves the sensitivity and/or specificity of image-derived parameters for diseases that directly or indirectly affect WM.
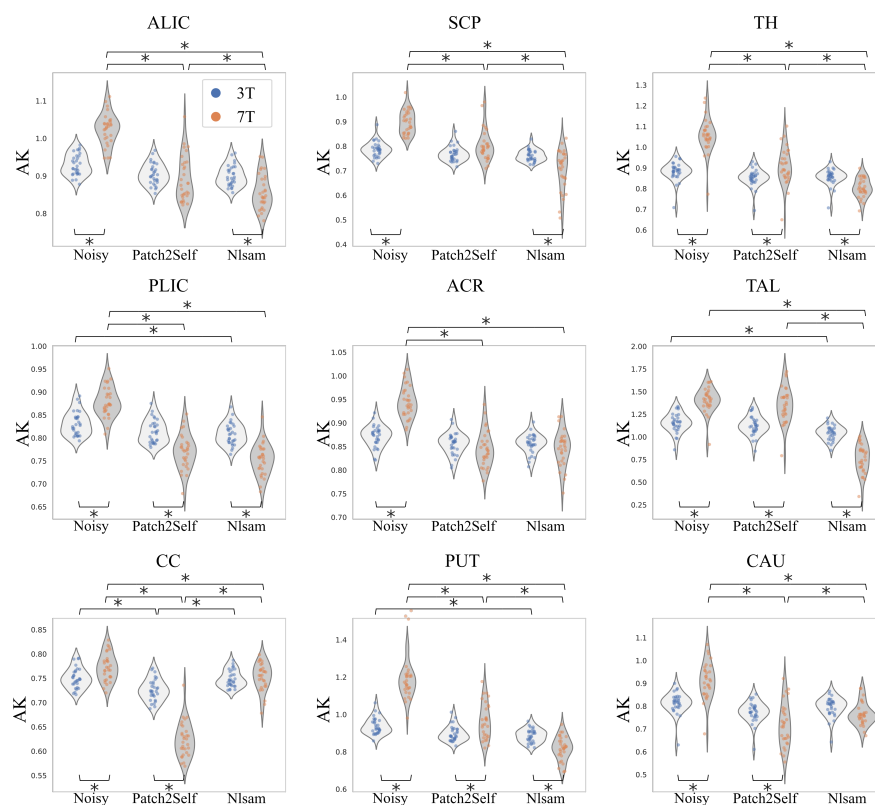
Appendix B

Supplementary Material

Figure B.1 **Violin plots of average AK over WM and GM ROIs at each field strength and denoising approach** with overlaid strip plots as a complement to show all observations along with representation of the underlying distribution. In two-way ANOVA with Bonferroni correction, upper $*$ indicates $p \leq 0.0056$, ($\frac{\alpha}{n}$, with $n = 9$) considering differences in the denoising approach at fixed magnetic field. Conversely, lower $*$ indicates $p \leq 0.0056$, ($\frac{\alpha}{n}$, with $n = 9$) considering differences in the magnetic field within the same denoising method.
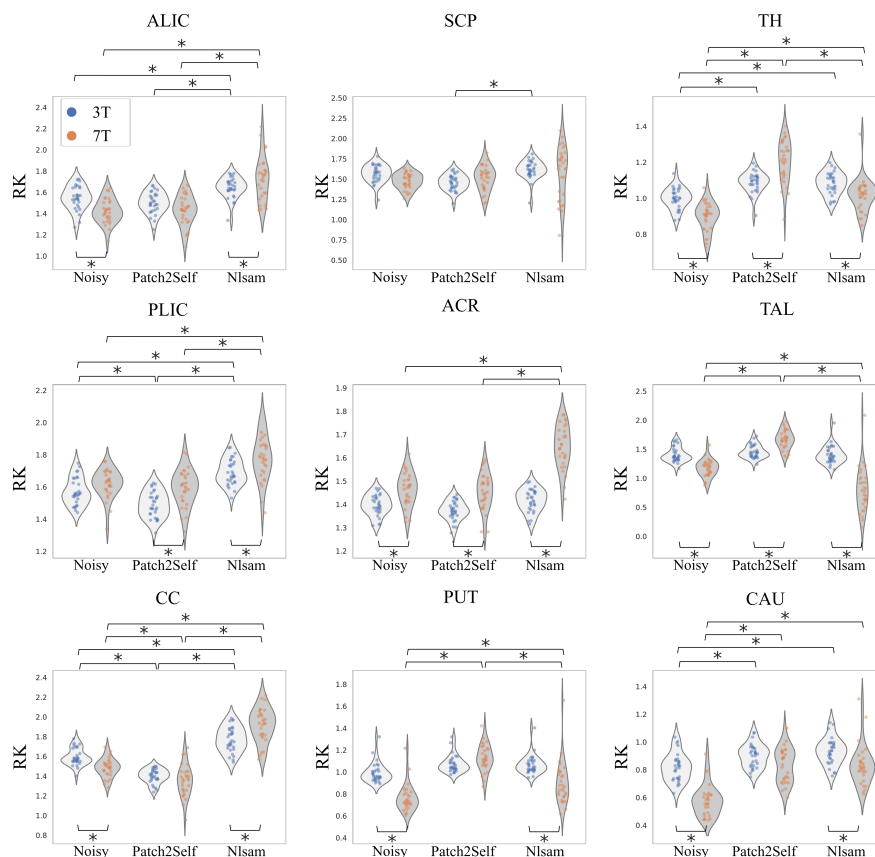
Figure B.2 **Violin plots of average RK over WM and GM ROIs at each field strength and denoising approach** with overlaid strip plots as a complement to show all observations along with representation of the underlying distribution. In two-way ANOVA with Bonferroni correction, upper $*$ indicates $p \leq 0.0056$, ($\frac{\alpha}{n}$, with $n = 9$) considering differences in the denoising approach at fixed magnetic field. Conversely, lower $*$ indicates $p \leq 0.0056$, ($\frac{\alpha}{n}$, with $n = 9$) considering differences in the magnetic field within the same denoising method.
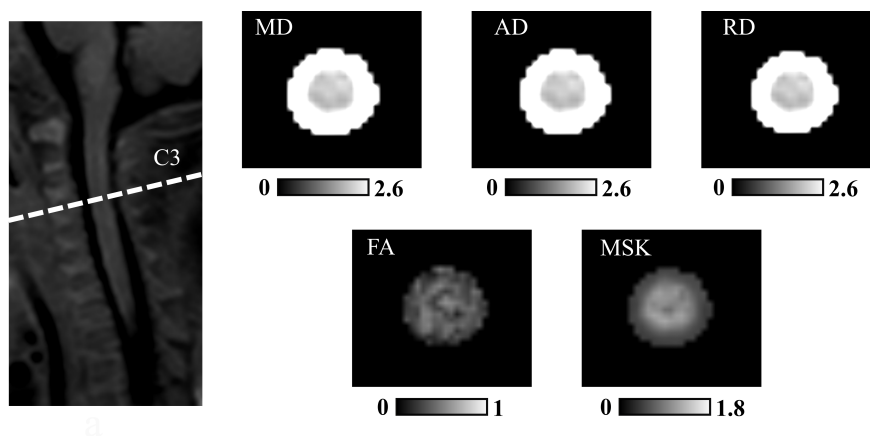

Figure B.3 **Diffusion and kurtosis maps at the mid-C3 level for one example subject**: Units for MD, AD and RD are $\mu m^2/s$, for MSK mm^2/s, while FA is dimensionless.
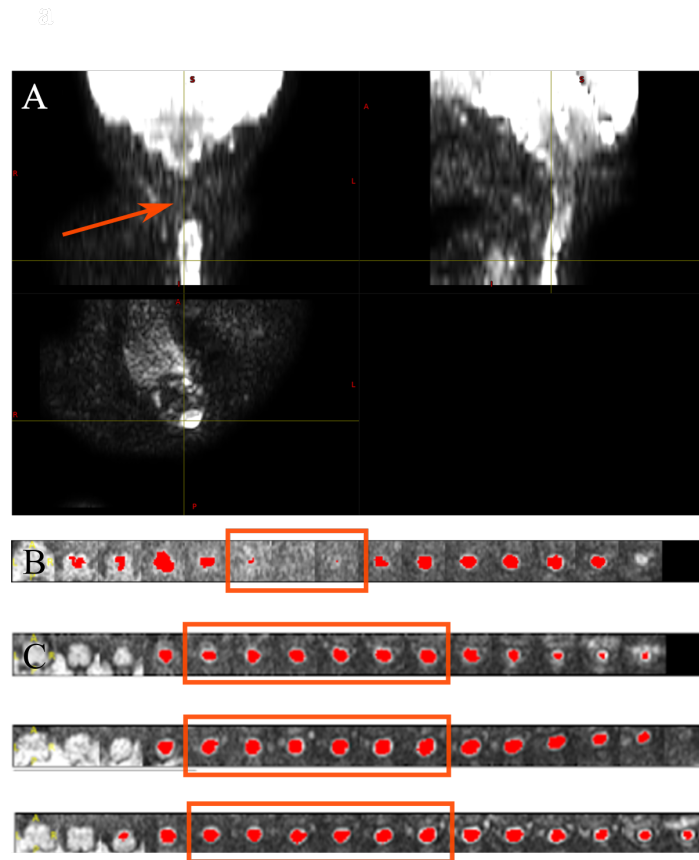
Figure B.4 **Quality control**: **(A)** Example of excluded DKI scan and **(B)** relative SC segmentation show signal loss across multiple slices as the coronal plane is not overlapping with the cord (ie: lordosis); **(C)** QC of C1-C4 levels: axial slices under analysis correspond to the same cervical levels for all subjects as shown in three example subjects.

Figure B.5 **Vertebral labeling**: Manual labeling of top of C1 vertebra and C3-C4 disc from graphical user interface integrated in SCT.
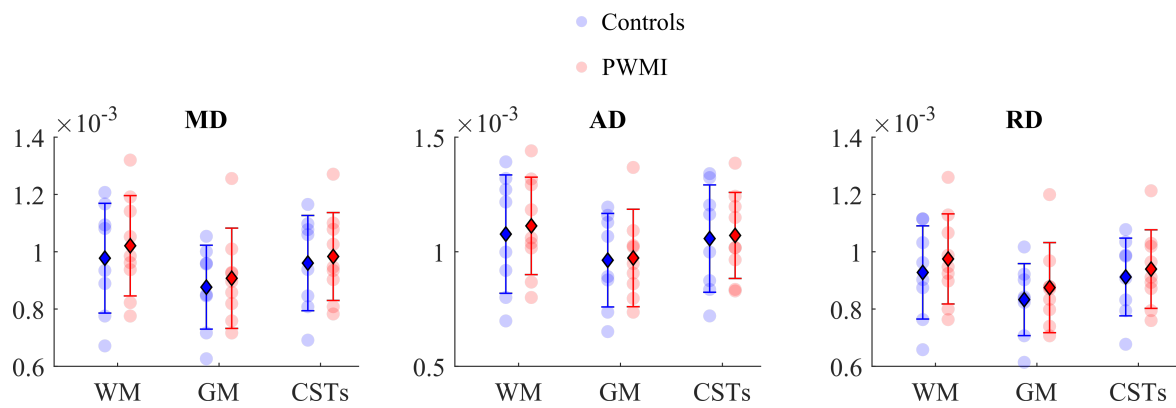
Figure B.6 **Extraction of diffusion measures within specific ROIs**: Scatter plots of DTI in group subjects across WM, GM and CSTs ROIs: coloured spots indicate single subject's value for each metric; as reported in the legend, controls' measures are in blue, whereas Periventricular White Matter Injury (PWMI) group's in red. Units for MD, AD, RD are in mm^2/s. Error bars displaying mean (diamond) and standard deviation (bars) are overlaid on scatter plots.

Table B.1 Two-way non-parametric Scheirer-Ray-Hare output to assess the presence of statistically significant differences in DTI- and MSDKI- derived metrics between patient and control groups

Test of Between-Subjects Effects

	Factor	SS	DF	H	p-value
MSK	diagnosis	1299.6	1	5.8812	**0.015303**
	ROI	402.71	2	1.8224	0.40203
	diagnosis*ROI	46.229	2	0.20921	0.90068
	residuals	9300	45	NaN	NaN
FA	diagnosis	0.019676	1	8.9043e-05	0.99247
	ROI	194.94	2	0.88221	0.64333
	diagnosis*ROI	56.327	2	0.25491	0.88033
	residuals	10797	45	NaN	NaN
MD	diagnosis	33.075	1	0.14968	0.69884
	ROI	874.94	2	3.9595	0.1381
	diagnosis*ROI	19.05	2	0.086209	0.95781
	residuals	10121	45	NaN	NaN
AD	diagnosis	12.297	1	0.055652	0.8135
	ROI	627.29	2	2.8388	0.24186
	diagnosis*ROI	12.197	2	0.055196	0.9728
	residuals	10397	45	NaN	NaN
RD	diagnosis	68.492	1	0.30996	0.5777
	ROI	1043.3	2	4.7214	0.094353
	diagnosis*ROI	16.863	2	0.076315	0.96256
	residuals	9919.9	45	NaN	NaN

*SS=Sum of Squares; DF=Degrees of Freedom; H= Test Statistics

Table B.2 Mann-Whitney U Test (Wilcoxon rank-sum test) as non-parametric version of the independent T-test for pairwise post-hoc comparisons between patient and control group within each ROI, limited to MSK and FA - the two variables of interest for this study

Multiple Comparisons of means

	ROI	U-val	RBC	CLES	p-value
MSK	WM	48.5	-0.347222	0.673611	0.247923
	GM	49.5	-0.375	0.6875	0.210682
	CSTs	55.5	-0.541667	**0.770833**	**0.06734**
FA	WM	35.5	0.013889	0.493056	1
	GM	39.5	-0.097222	0.548611	0.772694
	CSTs	34.5	0.041667	0.479167	0.923295

*ROI=Region of Interest; WM=White Matter; GM= Gray Matter;
U-val=U-value; RBC=Rank-Biserial Correlation; CLES= Common Language Effect Size
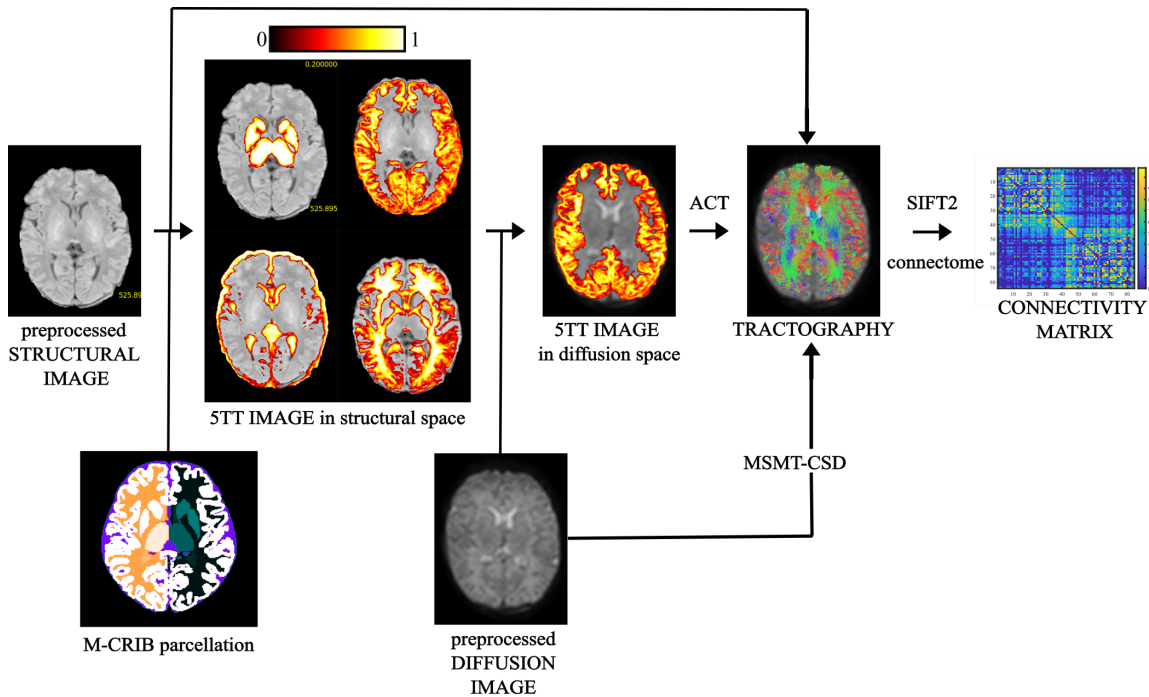
Figure B.7 **Structural Connectome pipeline:** overview of the main steps necessary for building structural connectomes: from generation of an infant-specific 5-Tissue-Type (5TT) segmented image, to Anatomically-Constrained Tractography (ACT), filtered with spherical-deconvolution informed filtering of tractograms (SIFT2) to further improve the estimation of streamlines, up to resulting structural connectome and relative connectivity matrix.
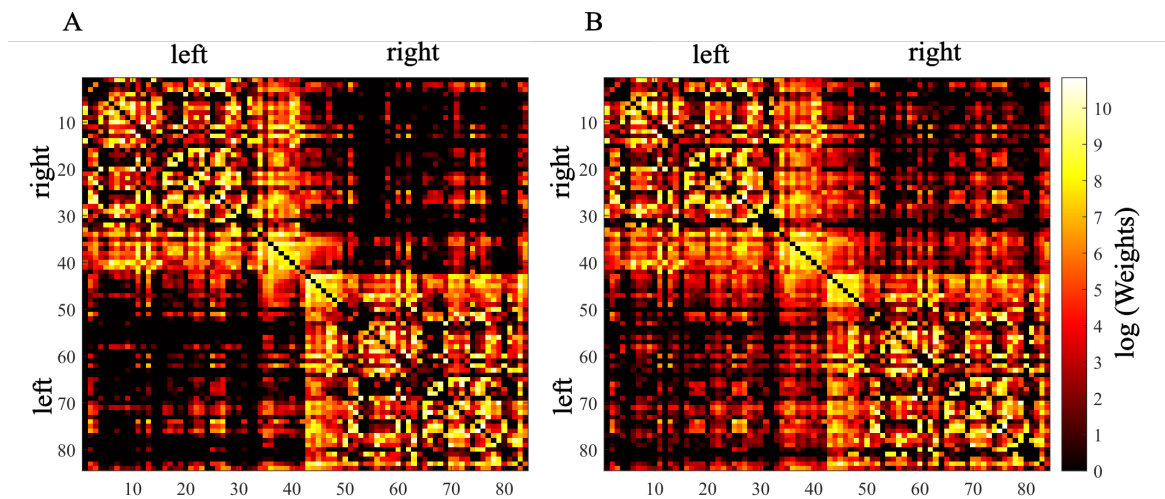

Figure B.8 **Exemplary connectivity matrices for two representative subjects**: **(A)** structural connectivity matrix for a 30 weeks PMA preterm subject and **(B)** for a 41 weeks PMA term-born control, both weighted by the number of streamlines connecting two parcels.

Figure B.9 **Population-specific DTI template:** lightbox displaying axial views of the age-specific template created ad-hoc for performing normalization of DTI volumes within DTITK and subsequent WM skeleton creation within TBSS.

Appendix C

List of Publications

International peer-reviewed papers:

1. **Trò R**, Roascio M, Gabriele A, Tortora D, Severino M, Rossi A, Napolitano A, Fato MM. *"Influence of adaptive denoising on Diffusion Kurtosis Imaging at 3T and 7T."* NeuroImage. 2022 May (submitted).

2. **Trò R**, Roascio M, Tortora D, Severino M, Rossi A, Cohen-Adad J, Fato MM, Arnulfo G. *"Diffusion Kurtosis Imaging of the neonatal Spinal Cord in clinical routine."* Frontiers in Radiology. 2022 Jan.

3. Roascio M, Canessa A, **Trò R**, Mattioli P, Famà F, Giorgetti L, Girtler N, Orso B, Morbelli S, Nobili F, Arnaldi D. *"Phase and amplitude electroencephalography correlations change with disease progression in people with idiopathic rapid eye-movement sleep behavior disorder."* Sleep. 2022 Jan;45(1):zsab232.

4. **Trò R**, Martini S, Stagnaro N, Sambuceti V, Torre M, Fato MM. *"A new tool for assessing Pectus Excavatum by a semi-automatic image processing pipeline calculating the classical severity indexes and a new marker: the Volumetric Correction Index."* BMC Medical Imaging. 2022 Dec;22(1):1-6.

5. Brusasco C, Santori G, Tavazzi G, Via G, Robba C, Gargani L, Mojoli F, Mongodi S, Bruzzo E, **Trò R**, Boccacci P. *"Second-order grey-scale texture analysis of pleural ultrasound images to differentiate acute respiratory distress syndrome and cardiogenic pulmonary edema."* Journal of Clinical Monitoring and Computing. 2020 Dec 12:1-0.

6. Brusasco C, Santori G, Bruzzo E, **Trò R**, Robba C, Tavazzi G, Guarracino F, Forfori F, Boccacci P, Corradi F. *"Quantitative lung ultrasonography: a putative new algorithm*

for automatic detection and quantification of B-lines." Critical Care. 2019 Dec;23(1):1-7.

Posters at conferences:

1. **Trò R**, Fadnavis S, Arnulfo G, Fato MM, Garyfallidis E. *"Impact of Patch2Self denoising on Diffusion Kurtosis Imaging at different field strengths."* 43rd Annual International Conference of the IEEE Engineering in Medicine and Biology Society (EMBC), virtual, 1-5 November 2021.

2. **Trò R**, Napolitano A, Toselli B, Arnulfo G, Tortora D, Severino M, Rossi A, Fato MM., *"Comparison of Diffusion Tensor and Diffusion Kurtosis Metrics acquired at 3T and 7T in Human Brain."* XI AIRMM Meeting (ISMRM Italian Chapter), virtual, 10-11 December 2020.